UNIVERSITY *of* NICOSIA

Integrating Micro-scale Modelling with Core Measurements to Improve Shale Gas Production

Ms. Natalia Kovalchuk

A thesis submitted to the University of Nicosia
in accordance with the requirements of the degree of
PhD (Doctor of Philosophy) in Oil, Gas and Energy Engineering

Department of Engineering

September, 2020

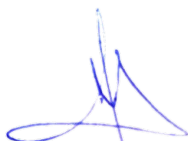# Integrating Micro-scale Modelling with Core Measurements to Improve Shale Gas Production

APPROVED BY
SUPERVISING COMMITTEE:
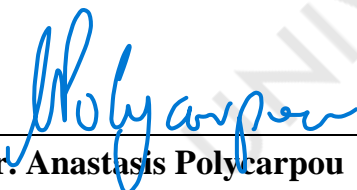
DATE OF APPROVAL:

15 Feb., 2021

Dr. Constantinos Hadjistassou
Associate Professor

17 Feb, 2021

Dr. Vasileios Gaganis
Assistant Professor

18/2/2021

Dr. Anastasis Polycarpou
Professor

Acknowledgements

Firstly, I would like to express my special appreciation and thanks to my advisor Associate Professor Constantinos Hadjistassou for his valuable guidance, encouraging my research and continuous support of my Ph.D. studies and related research, for his patience, motivation, and immense knowledge. His guidance helped me at all the times during my research and the writing phase of this thesis.

Furthermore, I would like to gratefully acknowledge financial support in the form of a scholarship from the University of Nicosia. My educational pursuits would not have been possible without the generous support from the scholarship.

My appreciation also goes to Professor Polycarpou and Assistant Professor Sarris for their useful questions and comments. The quest for answers helped me to better understand contentious matters and look at my research from a different perspective.

My special thanks to my parents. Words cannot express how grateful I am to my mother and father for all the sacrifices that you've made on my behalf. I would also like to thank all my friends who supported me in writing and motivated me to strive towards my goal. At the end, I would like to express my sincere appreciation to my beloved husband Evgenii who was always my support in the moments when there was no one to answer my queries.

Abstract

Traditionally, resources encountered in low-permeability ('tight') formations such as shales are deemed uneconomical for production. Advances in horizontal drilling and reservoir stimulation have shifted this perspective to render shale gas reservoirs one of the most promising hydrocarbon resources around the world. A profound understanding of the transport processes manifesting in shale gas reservoirs will contribute to more effective Enhanced Gas Recovery (EGR) schemes, lower production costs and, at the same time, improve the forecasting of gas production.

To gain more insights into the mechanics of gas production from shale formations, this thesis proposes a geometrically accurate model inspired from Scanning Electron Microscopy (SEM) imaging. Discretising the computational domain, the equations of flow were solved considering the mechanisms of Fickian and Knudsen diffusion, Klinkenberg's permeability, real gas compressibility and adsorption/desorption processes. The gas flowrate was determined and the pressure variations were deduced inside shale porous media at the micro-level. A non-dimensionalisation approach was developed that permits the comparison between micro-scale modelling results with actual core measurements several orders of magnitude apart in spatial and temporal scales. Non-dimensional micro-scale modelling results exhibit excellent agreement with actual core data shedding light on some of the important aspects which govern gas flow.

To ensure that the adsorption mechanism is thoroughly captured, the calculated isotherm profile should replicate experimental measurements within the whole pressure range. The adopted Klotz isotherm profile closely matches the core measurements, and this promotes a better understanding of the adsorption processes in the shale matrix. In parallel, a flowrate sensitivity analysis was conducted in the context of the matrix and the fluid properties. The sensitivity analysis revealed that, although permeability is the most prominent parameter governing gas flow rates, reservoir pressure requires even more attention, since it changes considerably during the lifetime of a gas field and it can be managed by a suitable production strategy. Ultimately, the effort to tie the prevailing theoretical understanding with experimental observations was deemed significant for boosting the productivity of gas from shale formations.

Table of Contents

Nomenclature

A_{outlet}	Outlet area	m^2
B	Gas formation volume factor	
b	Gas slippage factor	Pa
C	Magnitude of adsorbent and adsorbate interactions. The constant is related to the net heat of adsorption.	
C_F	Quadratic drag factor	
c_g	Gas compressibility	$(Pa)^{-1}$
C_m	Gas mole concentration	mol/m^3
c_m	Matrix compressibility	$(Pa)^{-1}$
c_p	Specific heat	$J/(kg \cdot K)$
c_t	Total compressibility	$(Pa)^{-1}$
D	Molecular diffusion coefficient	cm^2/s
d	Pore diameter	m, nm
d_{CH_4}	Molecular diameter of methane	m
D_k	Knudsen diffusivity	m^2/s
d_{outlet}	Outlet diameter	m
d_p	Effective pore diameter	m
F	Body force vector	
G	Field-strength gradient	G/cm
h_{model}	Model height	m
h_{net}	Net pay	m
K	Binding constant of already adsorbed molecules	
k	Permeability	mD, μD
k_∞	Permeability at infinite pressure (liquid permeability)	mD, μD
k_B	Boltzmann constant	J/K
k_g	Klinkenberg permeability	mD, μD
K_n	Knudsen number	
l	Length of the sample or the model size	m, μm
L_{Ke}	Constant associated with the kinetic energy of the Bouncing-back molecules	m
M	Molecular mass	kg/mol
M_g	Gas molar mass	kg/mol
MW	Gas molecular weight	g/mol
N	Number of measurements	
n	Maximum number of adsorption layers	
$NRMSE$	Normalised Root Mean Square Error	
P	Pressure	psi, Pa, MPa
P_0	Gas saturation pressure	Pa
P_c	Critical pressure	MPa
P_{cap}	Capilary pressure	psi
p_i	Initial pressure	Pa
P_L	Langmuir pressure	MPa
p_p	Pseudo-pressure	Pa/s
p_{pr}	Production pressure	Pa

P_r	Pseudo-reduced pressure	
Pr	Prandtl number	
P_{res}	Pressure in reservoir conditions	MPa
P_{sc}	Pressure in standard conditions	MPa
q	Volume flowrate	m^3/s
Q_n	Non-dimensional cumulative gas production	
q_n	Non-dimensional flowrate of the natural gas	
q_s	Tangential heat flux components to the wall	$J/(s{\cdot}m^2)$
Q_{sc}	Cumulative gas production under standard conditions	m^3
R	Gas constant	$J/(K{\cdot}mol)$
r	Pore radius	m, μm, nm
r_{th}	Pore-throat radius	m, μm, nm
r_{eff}	Radius of the pore with adsorbed gas molecules on its walls	m, μm, nm
r_K	Kelvin radius of the pore	m, μm, nm
r_{max}	Pore radius without any adsorbed gas molecules	m, μm, nm
r_p^m	Mean pore radius	m, μm, nm
S	Specific surface area	m^2/g
T	Temperature	°C, K, °R
t	Time	s, μs
T_2	Transverse relaxation time of the protons in a rock's pores	s
T_{2Bulk}	Transverse relaxation time	s
T_b	Boiling point of nitrogen	K
T_c	Critical temperature	K
TE	Inter-echo spacing used in the Carr-Purcell-Meiboom-Gill (CPMG) echo sequence	s
t_n	Non-dimensional time	
T_{nbp}	Temperature at normal boiling point	K
T_r	Pseudo-reduced temperature	
T_{res}	Temperature in reservoir conditions	K
T_{sc}	Temperature in standard conditions	K
t_{step}	Computational time step	s
t_{total}	Total time of gas flow	s
T_w	Reference wall temperature	K
U	Fluid flow velocity	m/s
U_w	Reference wall velocity	m/s
V_{ads}	Volume of the adsorbed gas	cm^3/g
V_{calc}	Adsorbed gas volume computed by employing chosen isotherm model	cm^3/g
V_{core}	Adsorbed gas volume from the core measurements	cm^3/g
V_L	Langmuir maximum sorption capacity	cm^3/g
V_m	Maximum adsorption gas volume when the entire absorbent surface is being covered with a complete monolayer	cm^3/g
V_{mol}	Molar volume of liquid nitrogen	m^3/mol
V_{res}	Gas volume in reservoir conditions	m^3
V_{sc}	Gas volume in standard conditions	m^3

W	Weight of the gas adsorbed at a specific relative pressure	g
W_m	Weight of monolayer nitrogen adsorbed to the sample	g
Z	Gas compressibility factor	
Z_{res}	Gas compressibility factor in reservoir conditions	
Z_{sc}	Gas compressibility factor in standard conditions	
α	Tangential momentum accommodation coefficient (TMAC) characterising the slip effect	
γ	Ratio of specific heats	
γ_b	Surface tension of nitrogen at its boiling point	N/m
γ_p	Constant of gyromagnetic ratio of a proton	MHz/T
θ	Contact angle	degrees
κ	Thermal conductivity	W/(m·K)
λ	Gas molecules mean free path	m
μ	Dynamic viscosity	Pa·s
ρ	Mass-density	g/cm^3
ρ_2	Surface relaxivity related to mineral-fluid interaction	Pm/s
ρ_r	Pseudo-reduced density	
σ	Interfacial tension	dynes/cm
τ	Shear stress tensor	N/m^2
τ_i	Tangential momentum of incoming molecules	kg·m/s
τ_r	Tangential momentum of reflected molecules	kg·m/s
τ_s	Viscous stress component corresponding to skin friction	N/m^2
τ_w	Tangential momentum of molecules reemitted from surface	kg·m/s
φ	Rock porosity	

List of Figures

List of Tables

List of publications

Kovalchuk Natalia and Hadjistassou Constantinos. 2018. New insights from shale gas production at the microscopic scale. *The European Physical Journal* E 41 (11): 134. https://doi.org/10.1140/epje/i2018-11741-5.

Kovalchuk Natalia and Hadjistassou Constantinos. 2019. Laws and principles governing fluid flow in porous media. *The European Physical Journal* E 42 (5): 56. https://doi.org/10.1140/epje/i2019-11819-6.

Kovalchuk Natalia and Hadjistassou Constantinos. 2020. Fathoming the Mechanics of Shale Gas Production at the Microscale. *Journal of Natural Gas Science and Engineering*: 103283. https://doi.org/10.1016/j.jngse.2020.103283.

Kovalchuk Natalia and Hadjistassou Constantinos. 2020. Integrating Microscale Modelling with Core Investigation Measurements to Improve Shale Gas Production. Submitted to *Journal of Petroleum Science and Engineering*.

Kovalchuk Natalia and Hadjistassou Constantinos. Microscale adsorption modelling. To be submitted to *Journal of Natural Gas Science and Engineering*.

1. Introduction

Shales are generally treated as non-porous formations and are often considered as a source rock and/or a cap rock (Chen *et al.* 2019). Over the past decades, after technical breakthroughs in the U.S.A., advanced techniques such as horizontal drilling, multi-stage hydraulic fracturing, micro-seismic monitoring and multi-well completions, have greatly promoted the exploitation of formations with low permeability like shale gas reservoirs or tight-gas sands (Chen *et al.* 2019; Li, Min*, et al.* 2016). Prominent examples of gas shale reservoirs are the Barnett and the Marcellus shales in North America, the Montney formation in Canada and others (Heller and Zoback 2014).

Nowadays, gas shale reservoirs have become an important source of natural gas production in North America and are attracting substantial interest as one of the most promising energy resources in South America, Europe and Asia (Alfi *et al.* 2015; Chen *et al.* 2015; Lan, Moghanloo and Davudov 2017) due to the projected rise in the global energy demand and the partial depletion of conventional reservoirs (Ali 2012). The Energy Information Administration (2013) reported that estimated gas reserves in shale reservoirs represent 32% of the recoverable natural gas in the world which amount to 7,299 trillion cubic feet (tcf) of shale gas (Bahadori 2016). However, with the exception of North America, shale production is still at embryonic stages elsewhere (Darabi *et al.* 2012; Tahmasebi, Javadpour and Sahimi 2015).

Although thousands of shale gas wells are actively producing petroleum around the world, factors controlling the permeability in shale gas formations are still poorly understood and lag behind the knowledge amassed from decades of gas production from conventional gas reservoirs (Huang *et al.* 2019; Jenkins *et al.* 2010; Ning *et al.* 2019). Due to the critical role that densely distributed and induced fractures play in gas production from shale reservoirs, much attention was dedicated in investigating gas flow from fractured media (Hattori *et al.* 2017; Nezhad *et al.* 2018). Generally, the matrix is treated as a natural gas storage space with very low permeability whereas flow processes in the shale matrix are disregarded theoretically. A fundamental understanding of the multiscale flow processes during extraction and accurate evaluation of the volume flows are crucial for efficient shale resources utilisation,

improving gas recovery and lowering production costs (Alfi *et al.* 2015; Kazmouz, Giusti and Mastorakos 2016).

Similar to conventional hydrocarbon systems, gas-prone shales are characterised by heterogeneity in composition and structure at all spatial scales (Heller and Zoback 2014). Nevertheless, shale gas reservoirs are dramatically different from conventional reservoirs in that their pore structures span from nanometres to micrometres, whereas most conventional gas reservoir pore systems are encountered at the micrometre or larger scales (Kalantari-Dahaghi and Mohaghegh 2011). The heterogeneous geological structure and extremely low permeability of shale reservoirs pose additional technical challenges, compared to conventional hydrocarbon resources (Alfi *et al.* 2015).

Migration of gas in nano- and micro-scale porous media is strongly correlated with factors such as the pore size, the pore pressure, the slippage effect, diffusivity, and the amount of adsorbed gas. While in general a porosity-permeability correlation can be obtained for most lithologies, shale systems present novel problems concerning the investigation of pore-scale flow and accordingly macroscopic permeability. Gas transport in extremely low-permeability shale formations, typically of less than 1 microdarcy, deviates considerably compared to conventional reservoirs by virtue of being a more complex process with many co-existing mechanisms, such as viscous flow, Knudsen diffusion, slip flow and gas adsorption-desorption (Guo, Wei and Liu 2015). These mechanisms are detailed in sections §2.4, §2.5, and §2.8. Therefore, Darcy's equation with volume averaged reservoir properties alone is no longer capable of capturing the complex gas transport in unconventional reservoirs (Guo, Wei and Liu 2015).

1.1. Problem definition

Due to the extremely low permeability of tight shale formations, the absence of densely distributed fractures renders natural gas production from shale reservoirs economically non-viable. Because the distribution of fractures fundamentally determines the productivity of shale reservoirs, the majority of studies concentrate on the characterisation of fractures. Remarkably, the flow in the matrix, which is usually treated as the storage medium of natural gas with very low permeability, is not explicitly

2

considered for production purposes. At the same time, owing to the ultra-low permeability of mudstones, it is difficult to experimentally probe the transport processes manifesting inside the shale rock and to accurately measure their physical properties.

Perhaps not surprisingly, insufficient clarity pertaining to the interaction of the factors controlling shale rock permeability and well productivity currently hamper the ability to accurately forecast future gas production. Such uncertainties also adversely affect the commercial prospects of gas projects (Morales-German, Navarro and Dubost 2012). Owing to their nano-scale pore sizes, flow in shale porous media is an involved process complemented by many co-existing mechanisms, such as viscous flow, Knudsen diffusion, slip flow and gas adsorption-desorption (Guo, Wei and Liu 2015). Many researchers have studied the physical mechanisms manifesting in gas shale rocks (Gouth *et al.* 2013; Mehmani, Prodanović and Javadpour 2013; Yu *et al.* 2017). However, there is a big gap between molecular scale models which accurately capture the physical processes and verified by analytical solutions, and field scale models based on well production data which rest on averaged values of reservoir properties.

In shale formations, not only the magnitude of porosity influences fluid transport but also pore structure and geometry come into play. Thus, it is essential to develop and investigate geometrically accurate models based on real shale images instead of models with averaged parameters. Furthermore, one can incorporate results from nano- or micro-models into macro-models enabling them to predict the well production rate, a parameter of interest to petroleum engineers. Hereafter, micro-level refers to a scale of 10^{-6} m (μm). The investigation of cumulative gas production and adsorption/desorption processes, at the micro-scale, can help improve the accuracy of the ultimate recovery estimation which is crucial for rational decision-making. In addition, modelling techniques based on real rock images can reduce the time necessary for core investigations while improving accuracy (Karniadakis, Beskok and Aluru 2005).

1.2.   Research objectives

Gas shale reservoirs are characterised by an extremely complex structure, with flow being driven by an array of physical mechanisms (Darabi *et al.* 2012; Freeman, Moridis and Blasingame 2011; Javadpour, Fisher and Unsworth 2007). The theory for

transport processes occurring in the shale matrix has yet to be fully explicated. This work aims to help clarify the flow characteristics and mechanisms in gas shale reservoirs and complements the prevailing state of understanding pertaining to flow in shale pores and pore throats. The objectives of our research are as follows:

- To build a micro-scale model grounded on a real shale pore network geometry so as to investigate the flow processes manifesting in the shale matrix.
- To implement the flow mechanisms related to shale gas reservoirs, namely, viscous flow, slip-flow, real gas behaviour, Knudsen diffusion, Klinkenberg permeability, and adsorption/desorption.
- To analyse the impact that shale pore geometrical structure exerts on the magnitude of the flowrate.
- To develop a non-dimensionalisation approach to allow the comparison of simulation results and core measurements at different spatial and temporal scales.
- To investigate the adsorption and desorption processes under different pressure conditions at the microscopic level.
- To perform a sensitivity analysis to investigate which shale reservoir characteristics govern flow the most.

1.3. Thesis outline

This thesis can be subdivided into five sections. In the first part, we offer a brief description of gas shale reservoirs, their characteristics, the pertinent flow processes, as well as their complexities. Although gas reserves in shale reservoirs make-up a considerable proportion of the world's hydrocarbon reserves, their exploitation is exceptionally challenging. The problem at the heart of this investigation was originally stated in the research objectives. In the second part, the relevant literature is presented. We begin with the shale rock characteristics and their determination through core investigation methods. Furthermore, we review the flow processes manifesting in the shale matrix and highlight their differences from those in conventional reservoirs. In the third part, we present our adopted approach and constructed model from actual micro-scale shale imaging data. The equations of flow in porous media are considered

and the numerical mesh is presented together with the discretisation procedure. Subsequently, the detailed modelling parameters are outlined. In the fourth part, we discuss the research results including the cumulative gas production and the flowrate investigation at the microscale. Hereafter, we elaborate on the non-dimensional approach allowing the comparison of numerical simulation results with core experimental findings. Finally, the sensitivity analysis of the developed model is detailed. In the last section, we concisely review the results and conclude by presenting future research directions.

2. Literature review

In this chapter, we outline various research and field attempts regarding shale gas reservoirs. Although a substantial amount of work has been done, gas shale reservoirs are still not fully understood. We begin with a general description of shales which are much more complex and heterogeneous in nature than convectional rocks. Next, we review the shale core investigation methods which include mercury injection capillary pressure, nitrogen adsorption, low-field NMR and gas production tests. We then analyse the flow mechanisms in shale nanopores (pores with sizes in range of nanometers, 10^{-9} m) which comprise viscous flow, slip-flow, Knudsen diffusion, and Klinkenberg permeability. As well as in conventional reservoirs, it is crucial to accurately model natural gas properties. Hence, viscosity was considered as a function of the gas molecular weight, pressure and temperature. Moreover, real gas compressibility which governs natural gas density was factored in the model. We conclude with the mechanism of adsorption and cover the topic of hydrocarbon production from gas shale reservoirs.

2.1. Description of shales

Generally speaking, shale is a fissile organic-rich mudstone. However, when referring to shale gas, the word shale does not allude to a specific type of rock. Instead, it describes rocks consisting of silt particles with sizes ranging between 4 μm to 60 μm, and clay-size particles smaller than 4 μm. Shale may comprise of various clay minerals with different properties such as kaolinite, illite, montmorillonite, clastic non-organic mineral fragments (for example, quartz) and organic matter (kerogen). Variabilities in mineral composition result in different physical properties which, in turn, govern the flow processes that manifest in shales (Kovalchuk and Hadjistassou 2018). The presence of a substantial amount of organic matter is crucial to the efficient gas production process as natural gas is usually sourced from the same shale rock (Clarkson *et al.* 2016; Darabi *et al.* 2012). In nature, shales can serve as closed hydrocarbon system constituting the reservoir, the source rock and the seal, and could host substantial volumes of oil and natural gas (Tahmasebi, Javadpour and Sahimi 2015; Zhang *et al.*

2017). Methane generated from organic material, under a large overburden pressure and high temperature conditions, can be trapped in shale (Lee and Kim 2016).
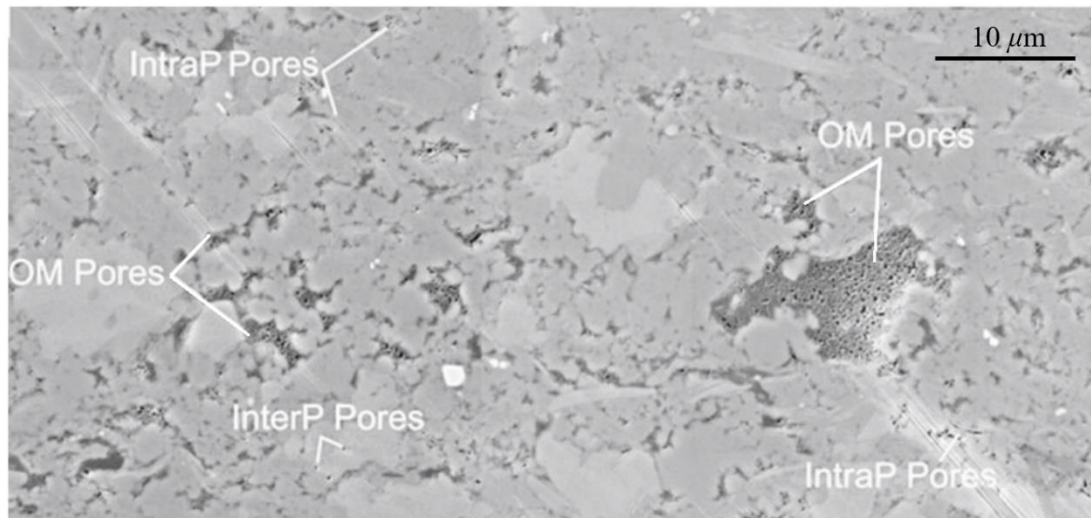
Figure 1. Scanning electron microscope (SEM) image of a Barnett shale sample with visible porosity of ≈4.2% (point count). The following pore types are also discernible: organic matter (OM) intraparticle, intraparticle (IntraP) and interparticle (InterP) pores. Adapted from Mehmani, Prodanović and Javadpour (2013).

One of the most powerful investigation methods for gas shale reservoirs is pore-scale imaging and modelling which is becoming a routine probing technique of core analysis (Blunt *et al.* 2013). Recent high-resolution imaging studies using SEM technologies, as illustrated in Figure 1, have revealed that matrix pores in shale consist of interparticle (between particles), intraparticle (within discrete particle boundaries) and organic matter intraparticle pores (pores within particles of organic matter). Their sizes ranged on the order of a micrometre (interparticle pores) down to between 100 nm to 3 nm for intraparticle pores (Mehmani, Prodanović and Javadpour 2013).
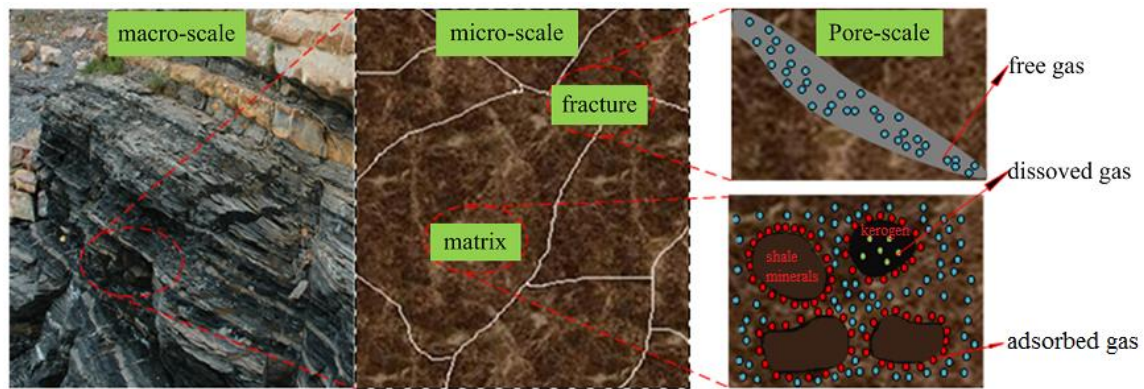
Figure 2. Illustration the structures in shales at different spatial scales. Courtesy: Guo, Wei and Liu (2015).

Mapping the pore distribution and geometry of shales is of great importance in clarifying the mechanics of the gas transport process in rock media. Figure 2 shows the gas distribution and geometry of shale layers from macro- to micro-scales. It informs us that gas in the shale matrix is encountered in three major forms: a) free gas stored in the pore network and fractures, b) adsorbed on the surface of the shale mineral and organic material, and c) dissolved in kerogen. The presence of nanosize pores in shales results in a considerably large inner surface area and, hence, the adsorption and desorption processes, which depend on the size of the surface area, become important (Etminan *et al.* 2014). During production and pressure depletion, gas desorbs from the pore wall and free gas permeates in the matrix system. Owing to the pressure difference between the matrix and the fracture system, the gas finds its way from the matrix to the rock fractures. Eventually, gas flows to the wellbore and is produced to the surface. Permeability in shale matrix also varies with confining pressure (or effective stress) in the reservoir. The depletion of the reservoir pressure causes the pore enclosure and size of throat to shrink. Upon pressure depletion this yields a reduction in permeability both within the micro-pores and the fractures (Ali 2012).

2.2. Methods used for the characterisation of shales

Core investigations are very important for gas shale reservoirs as well as for conventional reservoirs (Rao and Knight 2016). Because of the shale pores' tortuosity and spatial variability, a large number of core samples is required to estimate shale

porosity, permeability, mineralogy and the total organic carbon (TOC) (Tahmasebi, Javadpour and Sahimi 2015). At the same time, due to the minute size of the pores, laboratory investigations of shale rock samples are expensive and time-consuming (Sheng, Javadpour and Su 2018).

The pore structure of shale can be characterised by multiple parameters such as the pore size, the pore morphology, the pore volume, the specific surface area, and the spatial distribution. The pore structure characteristics are important factors in determining shale gas storage capacity and reservoir performance, and for their investigation one requires to employ different methods compared to conventional reservoirs (Yuan *et al.* 2014). The methods used for shale cores include: a) mercury injection capillary pressure (MICP), b) low-field nuclear magnetic resonance (NMR), and c) nitrogen (N_2) adsorption, d) gas production tests, and e) micro-scale imaging techniques.

The MICP and N_2 are destructive techniques as regards to the pore size distribution (PSD) measurements. Importantly, the MICP can characterise the PSD in the range of mesopores (5 nm < pore diameter < 50 nm) to macropores (pore diameter > 50 nm) while the N_2 technique can be applied to pores smaller than 2 nm in diameter. The MICP method treats pore throats and pore bodies as tubes and measures only connected pores while the NMR provides full experimental characterisation of the size of pore bodies arising from throats and isolated pores. The nuclear magnetic resonance method generates insights as to the pore-throat ratios that relate to porous media connectivity controlling fluid flow. The smaller the ratio, the lower the connectivity; hence the smaller will the permeability and fluid flow velocity be. In the following section, these methods will be elaborated upon in more detail.

Gas production tests estimate the rock gas storage capacity and production potential for different types of gases in pores in the form of free gas, adsorbed gas and dissolved gas. Since gas production tests cannot give comprehensive information about the pore size distribution in core samples, it should be performed in conjunction with the MICP, the nitrogen adsorption or the NMR methods.

2.2.1. Mercury injection capillary pressure (MICP)

Gas shale reservoirs are characterised by small pore throats, which create high capillary pressures. Mercury intrusion experiments are performed to quantify the capillary pressure behaviour, a parameter useful for the determination of the porous media parameters such as the pore diameter, the total pore volume, and its surface area. Moreover, the rock density and pressure relationship can be investigated and correlated with the permeability in some rock types.

When the capillary pressure is known, the pore-throat radius can be deduced from the Laplace-Washburn equation:

$$r_{th} = \frac{2\sigma \cos\theta}{P_{cap}}, \qquad (1)$$

where P_{cap} is the capilary pressure (psi), σ is the interfacial tension (dynes/cm), θ is the contact angle (degrees), and r_{th} is the pore-throat radius (μm). The capillary entry pressure can be substantially large, particularly for shales with very small pore throats (permeability). The entry pressure is inversely proportional to the size of the pore in which mercury will intrude (radius).
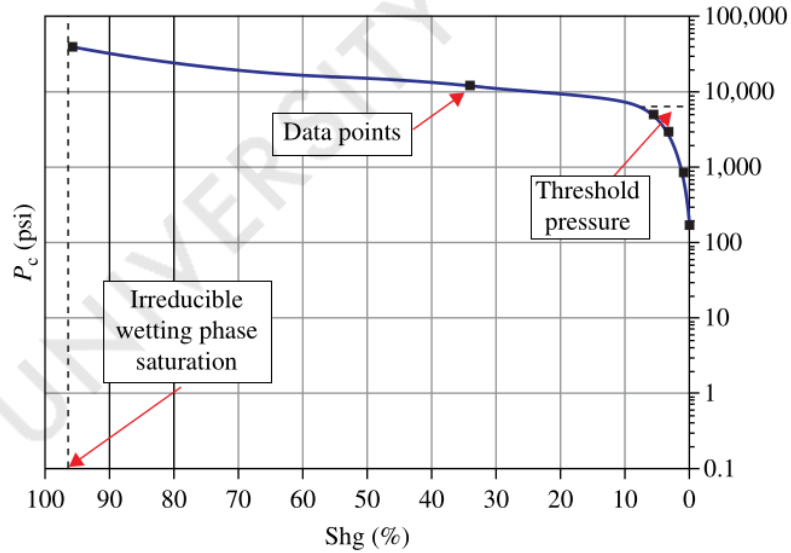
Figure 3. Typical capillary pressure profile. P_c - capillary pressure, Shg - non-wetting phase saturation. Source: Rezaee (2015).

Figure 3 displays the capillary pressure curve during the mercury injection process. At the lowest injection pressure when the non-wetting phase saturation equals to zero, mercury permeates to the biggest pores and then, while the injection pressure increases, reaches a plateau. Filling of the nanopores and pore throats in gas shale rock generates an inflection point where the pressure curve starts to yield a steep slope as the capillary pressure approaches high values. Since the MICP method works by progressively boosting pressure into the shale porous media and logging the pressure and injected volume at each step, mercury intrusion experiments cannot entirely characterise pore geometry. This technique measures only pore throat radii and cannot determine the size of the pore bodies which are present behind the throat (Rezaee 2015).

2.2.2. Nitrogen (N_2) adsorption

Pore geometry is intimately related to the pore surface area and gas adsorption. Therefore, the low-pressure adsorption measurements can shed light on the nanoporosity structure. Originally, the low-pressure adsorption methodology has been used extensively for surface chemistry analysis of porous materials, and recently has been applied for shale nanopore characterisation (Rezaee 2015).

Before adsorption measurements, the samples should be degassed at high temperature (110–140°C) and low pressure (1×10^{-3} bar). The main purpose of the degas procedure is to remove water and other adsorbed gases, which may influence the isotherm and could lead to incorrect shale properties (Firouzi, Rupp, *et al.* 2014). Nitrogen adsorption investigations are performed under low pressure and temperature conditions when nitrogen is in a liquid state and the quantity of gas adsorbed at different relative pressures (*P/P$_0$*) is measured, where *P* is the pressure in the system and *P$_0$* is the pressure of the adsorbent saturation. A pre-requisite for the N_2 measurement process is that all pores are filled by the adsorbate. Specific surface area is defined as the ratio between the total surface area of the pore walls of the rock to the total volume of the solid phase. The specific surface area is generally determined by the Brunauer-Emmett-Teller (BET) method and is calculated from the BET equation:

$$\frac{1}{W\left((P/P_0)-1\right)} = \frac{1}{W_m C} + \frac{C-1}{W_m C}\left(\frac{P}{P_0}\right), \qquad (2)$$

where W is the weight of the gas adsorbed at a relative pressure (P/P_0) (in grammes, g), P is the gas pressure in the system (Pa), P_0 is the pressure of the adsorbent saturation (Pa), and W_m is the weight of the monolayer nitrogen adsorbed to the sample (g). Term C is the magnitude of the adsorbent and adsorbate interactions and this constant is related to the energy of adsorption. The value of C varies by a wide range, from 5 to 350, depending on the adsorbate and adsorbent material as well as the experimental conditions and it should be measured experimentally (Fianu, Gholinezhad and Sayed 2019).

The mean pore radius can be determined from the surface area and the total volume of the adsorbed gas, at the maximum pressure. For example, assuming a cylindrical pore geometry, the mean pore radius (r_p^m) can be expressed as:

$$r_p^m = \frac{2V_{ads}}{S}, \qquad (3)$$

where V_{ads} is the entire volume of the adsorbed nitrogen (cm^3/g) and S is the specific surface area of the shale rock (cm^2/g). It is assumed that the pores that cannot be filled at a relative pressure of 1, make a negligible contribution to the total pore volume. The actual pore size distribution can be deduced from the thickness of the adsorbed layer and Kelvin's equation:

$$\ln\left(\frac{P}{P_0}\right) = \frac{2\gamma_b V_{mol}}{RT_b r_K}\cos\theta, \qquad (4)$$

where γ_b is the surface tension of liquid nitrogen at its boiling point (77 K) (N/m), θ is the contact angle between the adsorbate (liquid nitrogen) and the adsorbent (degrees), V_{mol} is the molar volume of liquid nitrogen (m^3/mol), T_b is the boiling point of nitrogen (77 K) (K). Parameter r_K is the Kelvin radius of the pore (m) (Rezaee 2015) which corresponds to the point of inflection on the hysteresis loop of the adsorption isotherm curve and may be interpreted as the radius of that pore having the most probable volume (Voigt and Tomlinson 1955).

2.2.3. Low-Field Nuclear Magnetic Resonance (NMR)

Low-field NMR is a non-destructive technique used in core plug investigations which measures the resonant motion induced by the magnetic field and the relaxation time of protons (hydrogen ^{1}H) appearing in water and hydrocarbon fluids in the porous rock. Before commencing the NMR scanning, core samples should be filled with brine of known properties or distilled water and then wrapped tightly with a transparent plastic wrap to prevent the fluid spreading out (Firouzi, Rupp, *et al.* 2014). A caveat of many of these analytical options is the fact that they assume that all pores in core plugs are saturated with fluid. The transverse relaxation time is mainly controlled by the pore size, the pore geometry and the diffusion transport and can be expressed as:

$$\frac{1}{T_2} = \frac{1}{T_{2Bulk}} + \rho_2 \left(\frac{S}{V} \right) + \frac{D \left(\gamma_p GTE \right)^2}{12}, \tag{5}$$

where ρ_2 is the surface relaxivity related to the mineral-fluid interaction (Pm/s), T_2 is the transverse relaxation time of the protons in a rock's pores (s). Parameter T_{2Bulk} is the transverse relaxation time (s), if all volume were to be filled by water, defined as a constant at specific pressure and temperature conditions for a constant water viscosity. Ratio S/V (Pm^{-1}) is the pore geometry index defined as the ratio of the pore surface to the pore fluid volume. The last term of the equation on the right hand side, refers to diffusion where D is the molecular diffusion coefficient (cm^2/s), γ_p is a constant of the gyromagnetic ratio of a proton (MHz/T), G is the field-strength gradient (G/cm), and *TE* is the inter-echo spacing used in the Carr-Purcell-Meiboom-Gill (CPMG) echo sequence (s) (Rezaee 2015).

2.2.4. Gas production test

Natural gas in shale pores is encountered in three different forms, i.e. as free gas in pore space, adsorbed gas on pore walls and dissolved gas in organic matter. The gas production test can yield valuable information to petroleum engineers about the gas storage capacity and production potential. The test experimental set-up, which is illustrated in Figure 4, is used to simulate flow from the matrix to a fracture and includes

a hydrostatic high-pressure core holder with two pads to seal the end faces of the core sample. The annulus between the core sample and the core holder provides a gas flow channel. The pads are connected to a high-pressure pump which maintains a constant confining pressure. Also, the testing system consists of a high-pressure cylinder with methane which supplies gas to the inlet of the core holder to sustain the production pressure, a gas flow metre and a backpressure regulator (BPR) which is used for production pressure control.
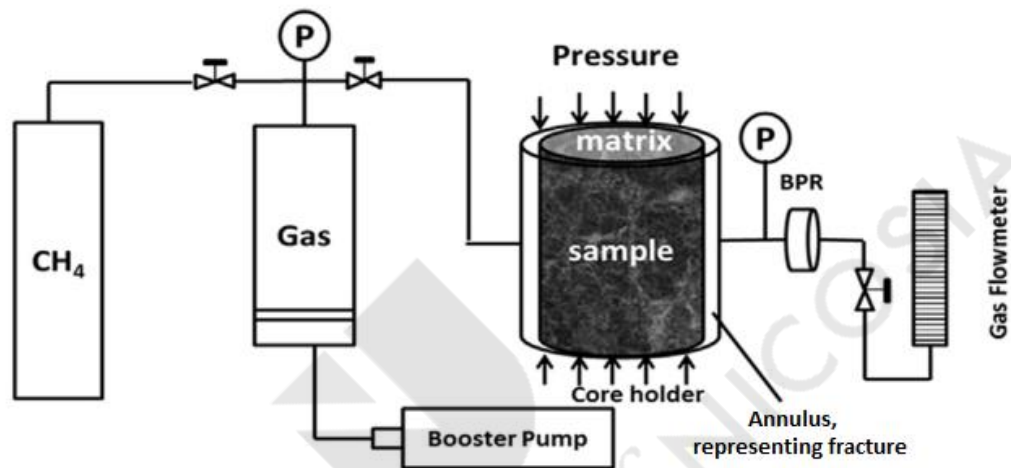
Figure 4. Schematic of the system used in gas production tests. Adapted from Sang *et al.* (2016).

Due to the extremely small permeability of the rock samples, preparation procedures before actual measurements require a considerable amount of time. Firstly, the core sample and all of the pressure lines should be kept under vacuum conditions for at least 12 hours, until the pressure inside the core samples reaches 0.001 Pa. Subsequently, the high-pressure gas cylinder is used to pressurise the core sample. The core samples should be pressurised for 15 days to maintain a uniform gas saturation in the core sample. To start a test, the required pressure is established in the annulus using the BPR and the outlet valve is opened to release gas. The accumulated gas production, at atmospheric pressure and ambient temperature (25.5°C), is recorded as a function of time. Obtained gas production data can be converted into reservoir conditions with the gas formation volume factor by the following relationship:

$$V_{res} = B \cdot V_{sc}, \tag{6}$$

where V_{res} and V_{sc} is the gas volume (m³) under reservoir and at standard conditions, correspondingly, and B is the formation volume factor which can be calculated as follows:

$$B = \frac{P_{sc}}{P_{res}} \cdot \frac{T_{res}}{T_{sc}} \cdot \frac{Z_{res}}{Z_{sc}}, \tag{7}$$

where P_{res} and P_{sc} is the pressure (MPa), T_{res} and T_{sc} is the temperature (K), and Z_{res} and Z_{sc} is the compressibility factor under the reservoir and at standard conditions, respectively.

2.2.5. Micro-imaging techniques

Meanwhile, alternative methods of investigation such as pore-scale imaging and modelling start to play an increasingly important role since they can help explain the macroscopic gas production behaviour by considering the physical processes at the pore level (Sheng and Thompson 2013). Two- and three-dimensional scanning electron microscopic (SEM) imaging of shale samples is becoming a vital characterisation tool because the key morphological features and flow properties of shales, such as the spatial distribution and connectivity of the pores, permeability, mineralogy and TOC can be discerned from these images (Lan, Moghanloo and Davudov 2017; Tahmasebi, Javadpour and Sahimi 2015).

The pore structure characteristics are important factors in determining the ability of shale to store gas and helps inform the evaluation of the shale reservoir. The pore structure of shale can be characterised by multiple parameters such as pore size, pore morphology, pore volume, specific surface area, and spatial distribution. Detailed studies of SEM images have demonstrated that pores in the shale matrix have very low connectivity. Curtis *et al.* (2011) noted that only 19% of the total porosity is connected. Hence, accurately measuring these pore structural parameters and investigating their controlling factors of great significance for the study of the shale gas accumulation and transport mechanisms.

2.3.   Gas shale production

Gas shale reservoirs are generally known for a substantial lateral extent which renders them promising for production purposes. However, shale reservoir permeability, which lies in the micro- to nano-Darcy range, renders gas extraction challenging both operationally and economically. During the last few decades, effective technologies for the extraction of these trapped hydrocarbons have undergone substantial improvement. In order to make gas production profitable, wells are generally completed horizontally with multistage hydraulic fracturing, which enhances the contact area between the shale formation and the well, as illustrated in Figure 5. Moreover, in some cases, batch drilling or multi-well pads are used, reducing the drilling time from several days to a few hours while also expanding the rock surface area exposed to production (Bringedal 2015). The optimal direction for horizontal drilling is at an orientation which maximises the number of natural fractures intersected by the well. These fractures will provide additional pathways for the gas, which is trapped in the shale reservoir, to flow in the tubing, once the hydraulic fracturing operation was performed.
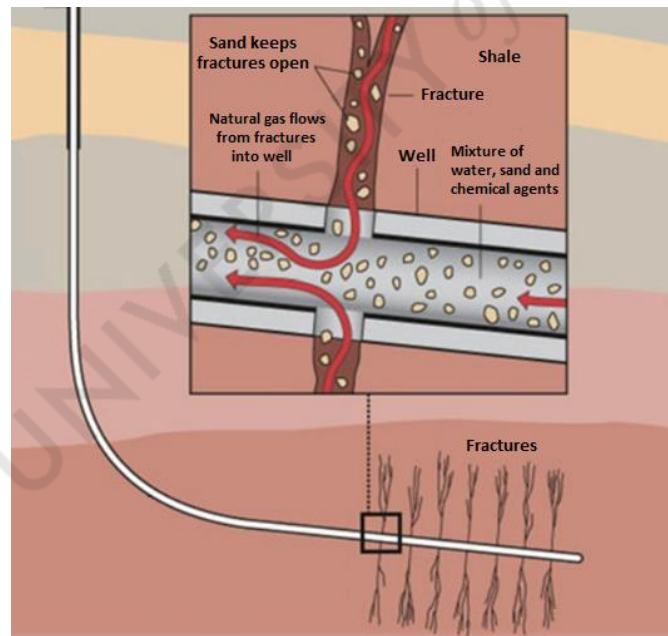
Figure 5. Hydraulically fractured horizontal well in a gas shale reservoir. Courtesy: Lee and Kim (2016).

Shales possess extremely low permeability, hence, the main goal of hydraulic fracturing is the exposure of as large surface area of the shale rock as possible to the pressure drop (Kalantari-Dahaghi and Mohaghegh 2011). For gas shale reservoirs, the usual hydraulic fracturing fluid is slickwater which consists of a low viscosity mixture of water, lubricants and sand (Lee *et al.* 2011). The composition of fracturing fluid and the chemical additives are chosen to be the most suitable for the specific reservoir and operational conditions. Additives in slickwater include friction reducers, acids to remove drilling mud damage within the near-wellbore area, oxygen scavengers and other stabilizers to prevent corrosion of metal pipes, and biocides to reduce biofouling of the fractures (Ketter *et al.* 2008).

The key to good shale gas production over time is having the proper distribution and placement of the sand particles to keep the fractures open. During hydraulic fracturing, up to 20% of the water can find its way to the surface through the well. This effect is known as flowback. Once on the surface, the returned water can be treated and reused for subsequent hydraulic fracture jobs, thereby significantly reducing the volume of water needed as well as environmental footprint.

2.4. Flow regimes

Due to the nanoscale characteristics of the shale matrix, flow regimes in the pores differ from flow in conventional formations, such as sandstone and siltstone. Consequently, Darcy's law cannot realistically describe the mechanics of flow in shale deposits. Since small size nanopores can contain fewer molecules of gas in comparison to macropores, the collisions between the gas molecules and the pore wall starts to play an increasingly important role compared to the intermolecular interactions (Kovalchuk and Hadjistassou 2018). Such a condition is termed as the "confined" or "pore proximity" effect because the molecular free path is restricted by the available void space in the pore (Bahadori 2016).

The Knudsen number (K_n) was proposed to divide and classify the four flow regimes, namely, a) the continuum flow regime, b) the slip flow regime, c) the transition regime and d) the free molecular flow regime. Defined as the ratio between the gas

molecules mean free path (λ) to the pore diameter (d), the Knudsen number is expressed by:

$$K_n = \frac{\lambda}{d} \quad . \tag{8}$$

The mean free path of the gas molecules is defined by:

$$\lambda = \frac{k_B T}{\pi d_m^2 P \sqrt{2}} \quad . \tag{9}$$

Here, k_B is the Boltzmann constant (1.3807×10^{-23} J/K), and T and P are the absolute temperature (K) and absolute pressure (Pa), respectively. The effective molecular diameters can be estimated from the appropriate covalent and van der Waals radii.
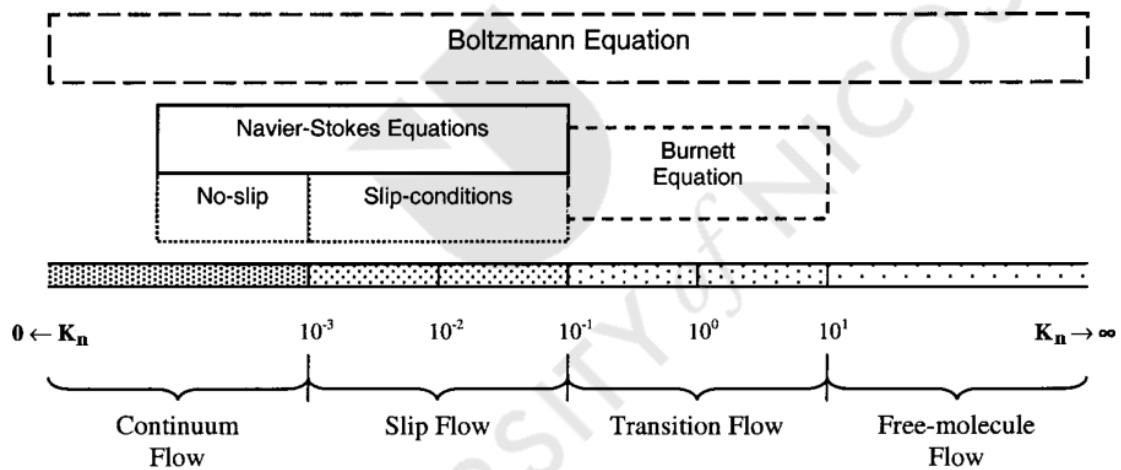
Figure 6. Knudsen numbers for different flow regimes. Source: Roy *et al.* (2003).

Figure 6 depicts the division between the various flow regimes. For small Knudsen numbers (K_n<0.001), the continuum fluid equations with the traditional no-slip velocity conditions on the walls can be used, i.e., the Navier-Stokes equation. When the Knudsen number increases ($0.001<K_n<0.1$) in the slip flow regime, the Navier-Stokes equation can be used for bulk flow modelling. Nonetheless, it is necessary to take into account the non-continuum effect which can be expressed as an empirical velocity slip near the walls. Large Knudsen numbers characterise the transition

($0.1<K_n<10$) and the free molecular ($K_n>10$) flow regimes. Flows in these two regimes cannot be described by the Navier-Stokes equation anymore. Therefore, one needs to resort to the Boltzmann equation of the gas kinetic theory (Chen *et al.* 2015). In real porous media with a diversity of pore sizes, different flow regimes could manifest concurrently (Firouzi, Alnoaimi*, et al.* 2014). It should be noted that, transition between flow regimes is smooth and this division is mainly empirical, so the aforementioned limits of the different regimes should not be treated as exact values (Michalis *et al.* 2010).

2.5.   Flow in nanopores of shale formations

Physically capturing the ratio of the molecular mean free path and the pore diameter, the Knudsen number (K_n) can be used to identify the particular fluid flow regime. For typical shale gas formations' temperatures, ranging between 310K and 360K, and pressures, spanning between 10 MPa and 35 MPa, the molecular mean free path of methane may range between 0.2 nm and 0.75 nm. Consequently, K_n takes values between 0.01 and 0.38 in pores with a size range from 2 nm to 50 nm. For these Knudsen numbers, Darcy flow (advection) becomes small and molecular diffusion with slip flow starts to play a significant role and shale permeability becomes dependent not only on the porosity, but also on the pore throat size, the pressure and the type of the gas (Dejam, Hassanzadeh and Chen 2017). Apparently, the continuum assumption of fluid flow may break down and the Navier-Stokes equation with no-slip boundaries ceases to apply (Zhang *et al.* 2014).
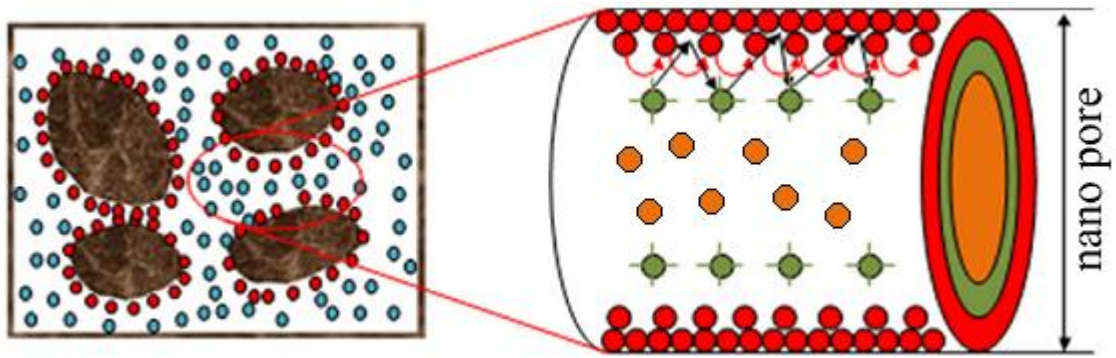
Figure 7. Gas flow in a shale nano-pore. Red dots represent adsorbed gas, green dots show Knudsen diffusion and orange ones signify viscous flow. Adapted from Guo, Wei and Liu (2015).

During gas production, a depletion in pressure can deform the shale pores and reduce the pore size, as well as induce a drop in permeability (Duru and Horne 2010). Therefore, the precise estimation of permeability and diffusivity values in gas shale reservoirs becomes critical when determining their efficiency for commercial operations (Haider and Aziz 2017). Figure 7 portrays the gas distribution and transport mechanisms in shale nano-pores which include viscous flow, Knudsen diffusion, and slip flow (Lee and Kim 2016). In the following subsections these mechanisms will be explained in more detail.

2.5.1. Fickian diffusion

When the pore diameter is much bigger than the mean free path of the gas molecules and the Knudsen number is appreciably lower than 1, the motion of the gas molecules is predominantly governed by molecular collisions. However, when the pore size becomes comparable to the mean free path, gas flow is characterised by Knudsen diffusion. In real porous media exhibiting various pore size distributions, molecular diffusion and Knudsen diffusion manifest themselves concurrently. Moreover, tortuosity of the pores influences the molecular motion, and consequently, the gas flow (He 2011). Figure 8 depicts the processes of molecular and Knudsen diffusion and their combinations.
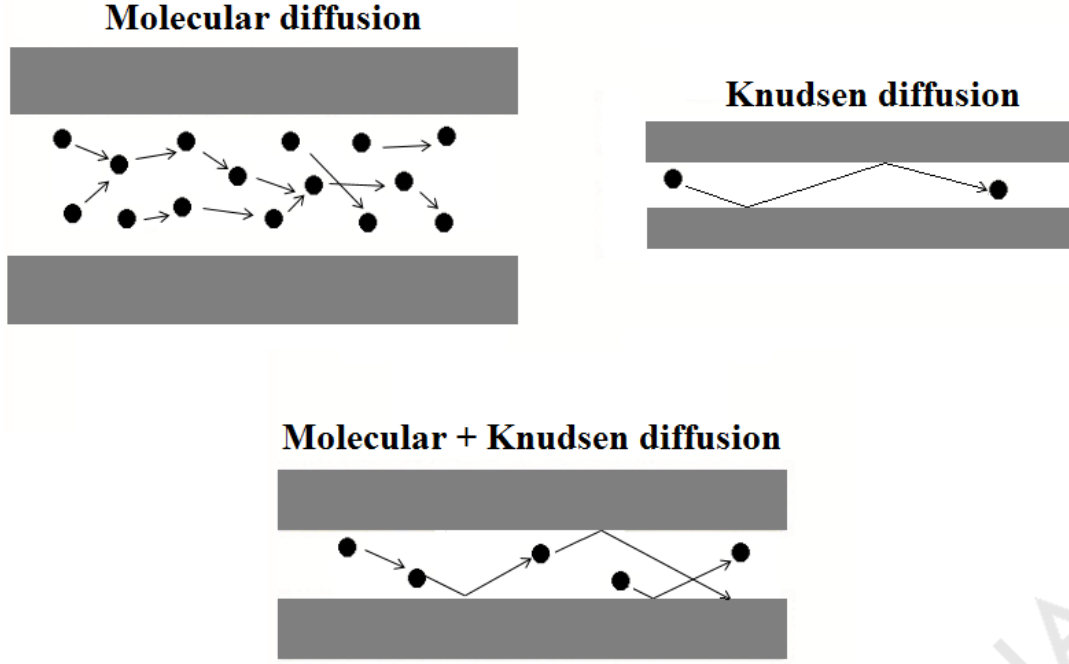
Figure 8. Types of porous diffusion and their combinations.

2.5.2. Knudsen diffusion

When gas molecules collide mainly with pore surfaces but not with other molecules, while transported along the pore walls by gas slippage and surface hopping of adsorbed gas molecules, the particles undergo Knudsen diffusion (Firouzi, Alnoaimi, *et al.* 2014). Under these circumstances, the gas mass flow can be expressed by:

$$J_k = -M_g D_k (\nabla C_m),\qquad (10)$$

where M_g is the gas molar mass (kg/mol), D_k is the Knudsen diffusivity of the rock (m^2/s), and C_m is the gas mole concentration (mol/m^3).

Knudsen's diffusivity in a local pore can be determined from:

$$D_k = \frac{d_p}{3} \sqrt{\frac{8RT}{\pi M}},\qquad (11)$$

where T is the absolute temperature (K), M is the molecular mass (kg/mol), and d_p is the effective pore diameter which can be determined by averaging the pore diameter in several directions (m) (Chen *et al.* 2015).

21

2.5.3. Klinkenberg permeability

In low-permeability formations (<0.001 md), or under low-pressure conditions, the gas absolute permeability depends on gas pressure since the mean free path is inversely proportional to the gas pressure. The explanation for this behaviour was given by Klinkenberg in the 1940s in his seminal work that took into account the phenomenon of gas slippage (Klinkenberg 1941). Accordingly, the steady-state flowrate through small capillaries is higher due to the slippage of gas molecules at the capillary walls. Klinkenberg combined Poiseuille's law for gas flow in capillaries with Darcy's law for flow in porous media to obtain what was later dubbed as the Klinkenberg's equation:

$$k_g = k_\infty \left(1 + \frac{b}{p_m} \right) , \tag{12}$$

where k_∞ is the permeability at infinite pressure (liquid permeability) (mD) and b is the gas slippage factor (Pa) (Bahoush and Kazemzadeh 2009). As it can be discerned from equation (12), at low pressures the slippage effect becomes more important and subsequently gas permeability is enhanced. At large mean pressures, the slippage effect is suppressed, and permeability decreases until the mean free path is reduced to zero at infinite pressure. Hence, under high pressure conditions the condensed gas is considered to behave as a liquid and its permeability becomes equivalent to the permeability of an inert liquid, k_∞ (Firouzi, Alnoaimi, *et al.* 2014). The gas slippage factor can be calculated from:

$$b = \frac{16\mu}{3000r} \left(\frac{8\pi RT}{M} \right)^{0.5} + \left(\frac{8\pi RT}{M} \right)^{0.5} \frac{\mu}{r} \left(\frac{2}{\alpha} - 1 \right) , \tag{13}$$

where α is the tangential momentum accommodation coefficient (TMAC) characterising the slip effect. Parameter α depends on the wall surface smoothness, the gas type, the temperature, and the pressure and varies between 0 and 1. Usually TMAC takes a value of 0.8 whereas a more accurate number for a specific gas can be deduced from laboratory experiments or numerical methods (Guo, Wei and Liu 2015).

Further investigations demonstrated that smaller capillaries yield much higher fluid flow velocities than predicted by the Klinkenberg's slippage theory (King 2007).

Based on a numerical study, Fathi *et al.* (2012) proposed a more sophisticated Klinkenberg's equation in the following form:

$$k_g = k_\infty \left[1 + \left(\frac{b}{p_m} \right)^2 \left(\frac{L_{Ke}}{\lambda} \right) \right],$$
(14)

where L_{Ke} is associated with the kinetic energy of the bouncing-back molecules (m). Here b is the gas slippage factor (Pa) which is used in the Klinkenberg's equation and can be calculated from equation (13). An example of the dependence of Klinkenberg permeability on pressure is shown in Figure 9.

Consulting equation (14) and comparing to Klinkenberg's theory, the quadratic expression and the term inside the second parenthesis (RHS) are new, capturing the kinetic effect of the gas molecules. This kinetic effect becomes important in the small capillaries (less than 10 nm), therefore, equation (14) describes shale rock's permeability more accurately.

In large capillaries, the kinetic effect of the gas molecules is negligible, hence, the (L_{Ke}/λ) ratio is on the same order as (p_m/b) and Klinkenberg's equation is applicable. Furthermore, at significantly high pressures, the slippage effect is suppressed, and the gas molecules are considered to behave as a liquid and term (b/p) (equation (14)) diminishes to zero. Therefore, the permeability becomes equivalent to the permeability of a non-reactive liquid, k_∞ (Firouzi, Alnoaimi*, et al.* 2014).
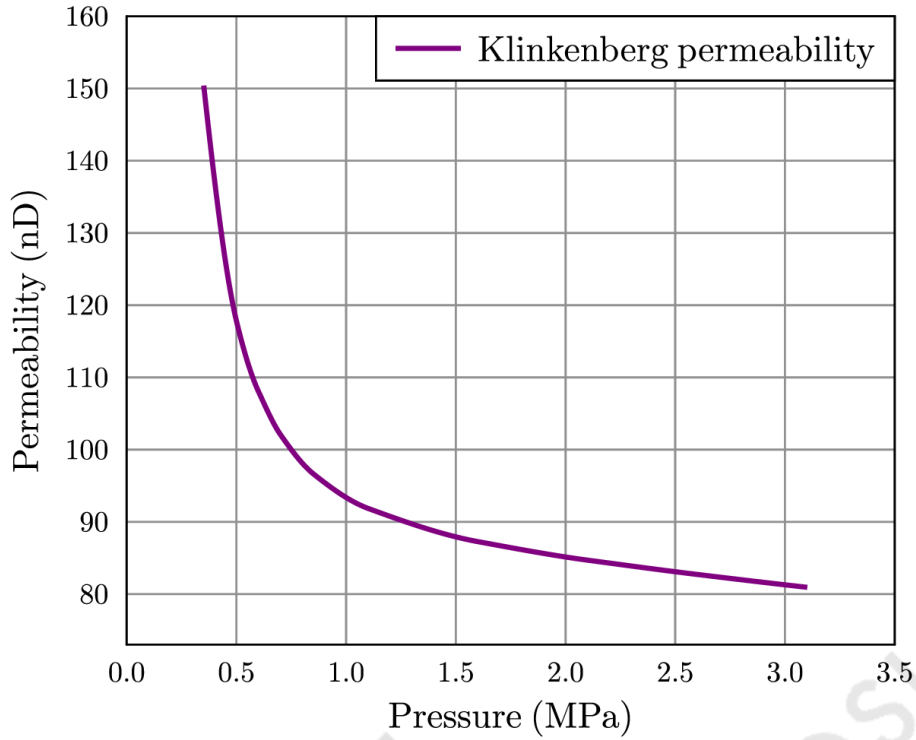
Figure 9. Klinkenberg permeability behaviour in relation to pressure.

Moreover, during gas desorption from the pore walls, spurred by a pressure drop, gas transport channels expand in size. An increase in pore size results in a reduction of the frequency of molecular gas collisions with the pore walls, and thus Knudsen diffusion and slip weaken their leverage as a transport mechanism. Whereas Klinkenberg permeability, as shown in equation (12), captures the relationship between the pore size and the number of gas collisions, in contrast equation (13) ascertains that the smaller the pore radius (r), the smaller the magnitude of the slip effect coefficient (b). At the same time, as the pore radius enlarges, the viscous flow indicated by the orange dots in Figure 7 starts to play a more dominant role and imparts a bigger influence to gas flow (Guo, Wei and Liu 2015). Although this effect is not significant, it cannot be omitted.

2.5.4. Slip boundary conditions for the Navier-Stokes equations

In nano-size pores, when the Knudsen number is larger than 0.001 and the slip flow regime occurs, the Navier-Stokes equations can still be applied to the flow,

however slip flow effects near the pore walls should also be taken into account (McNenly, Gallis and Boyd 2005). To address this issue, slip boundary conditions have been proposed which incorporate the rarefied gas slipping at the pore surface and determine actual velocity slip at the fluid-pore wall interface (Lockerby, Reese and Gallis 2005; McNenly, Gallis and Boyd 2005).

Slip boundary conditions can be considered using the following relationship:

$$U_s - U_w = \frac{2-\alpha}{\alpha}\left(\frac{1}{\rho(2RT_w/\pi)^{1/2}}\right)\tau_s - \frac{3}{4}\left(\frac{\Pr(\gamma-1)}{\gamma\rho RT_w}\right)q_s \ , \qquad (15)$$

where q_s are the tangential heat flux components to the wall (J/(s·m²)); τ_s is the viscous stress component corresponding to the skin friction (N/m²); γ is the ratio of specific heats; U_w and T_w are the reference wall velocity (m/s) and temperature (K), correspondingly, and α is the tangential momentum accommodation coefficient. The Prandtl number (Pr) is expressed by (Karniadakis, Beskok and Aluru 2005):

$$\Pr = \frac{C_p\mu}{\kappa} \ , \qquad (16)$$

where μ is the dynamic viscosity (Pa·s), κ is the thermal conductivity (W/m·K), and c_p is the specific heat capacity (J/kg·K).

The tangential momentum accommodation coefficient is usually measured experimentally from the mass flowrate through a single microtube in the slip flow regime and represents the statistical characteristics of the mean exchange value of the tangential momentum (Yamaguchi, Matsuda and Niimi 2012). The tangential momentum accommodation coefficient depends on the gas and the pore surface temperatures, the local pressure, the velocity and the main direction of fluid flow. The tangential momentum accommodation coefficient (σ_v) can be calculated from:

$$\sigma_v = \frac{\tau_i - \tau_r}{\tau_i - \tau_w} \ , \qquad (17)$$

where τ_i and τ_r denote the tangential momentum of the incoming and the reflected molecules (kg·m/s), respectively, and τ_w is the tangential momentum of the molecules reemitted from the surface (kg·m/s). For stationary surfaces τ_w is 0 (Karniadakis, Beskok and Aluru 2005).

25

2.6. Compressibility

Another challenge in gas reservoir analysis is related to the accurate estimation of the gas compressibility factor values, since gas properties vary significantly during production (Zhang *et al.* 2017). This is necessary in reserves estimation, engineering applications, material balance calculations and gas production. The magnitude of deviations between the real gas behaviour and the ideal gas law increases with rising pressure and temperature and changes substantially with the composition of the gas (Okoro *et al.* 2017). The non-linear nature of the partial differential equations (PDEs), for real gas behaviour, renders the pertinent simulation models more complex, requiring significant time to converge (Zhang *et al.* 2017).

The ideal gas law is the simplest equation which can be used to capture the relation between pressure, temperature and volume of an ideal gas. For a more realistic determination of the gas behaviour, the real gas law could be used:

$$\rho = \frac{P \cdot MW}{ZRT} \ , \tag{18}$$

where ρ is the gas mass-density (g/cm^3), P is the absolute pressure (Pa), MW is the gas molecular weight (g/mol), Z is the gas compressibility factor, R is the gas constant (8.314 J/(K·mol)), and T is the absolute temperature (K). As it can be observed from equation (18), the compressibility factor is necessary to determine the gas density at particular temperature and pressure conditions. Standing and Katz have developed charts for the Z factor as a function of P_r and T_r which are the pseudo-reduced pressure and pseudo-reduced temperature, respectively (Rao and Knight 2016):

$$P_r = \frac{P}{P_c} \ , \tag{19}$$

$$T_r = \frac{T}{T_c} \ . \tag{20}$$

For methane, the critical pressure and temperature are P_c = 4.6408 MPa and T_c = 190.5 K (Constant 1963). Abou-Kassem and Dranchuk (2017) have proposed a numerical relation for the Z factor, as a function of P_r and T_r, over ranges between 2-30 and 1-3 for P_r and T_r, respectively, as follows:

$$Z = 1 + \left(A_1 + \frac{A_2}{T_r} + \frac{A_3}{T_r^3} + \frac{A_4}{T_r^4} + \frac{A_5}{T_r^5} \right) \rho_r + \left(A_6 + \frac{A_7}{T_r} + \frac{A_8}{T_r^3} \right) \rho_r^2$$
$$- A_9 \left(\frac{A_7}{T_r} + \frac{A_8}{T_r^2} \right) \rho_r^5 + A_{10} \left(1 + A_{11} \rho_r^2 \right) \left(\frac{\rho_r^2}{T_r^3} \right) \exp\left(-A_{11} \rho_r^2 \right) \quad . \tag{21}$$

The pseudo-reduced density (ρ_r) is defined as follows:

$$\rho_r = \frac{0.27 P_r}{Z T_r} \quad . \tag{22}$$

The constants of equation (21) are listed in Table 1.

Table 1. Constants for Z-factor calculations.

Constant	Value
A_1	0.3265
A_2	-1.07
A_3	-0.5339
A_4	0.01569
A_5	-0.05165
A_6	0.5475
A_7	-0.7361
A_8	0.1844
A_9	0.1056
A_{10}	0.6134
A_{11}	0.721

The Z factor of natural gas can be determined from equation (21) by utilising a trial and error method (Rao and Knight 2016).

2.7. Viscosity

Natural gas viscosity, as well as other fluid properties, is important in calculating the gas flow rate through the reservoir rock. Fluid viscosity is a function of gas composition, pressure, and temperature. As a result, viscosity changes during gas

production. However, gas viscosities are rarely measured because many laboratories do not have the required equipment for such measurements (Elsharkawy 2002). Gas viscosity is frequently estimated from equations of state or empirical correlations. Thus, it is particularly important to use an accurate method to predict gas viscosity.

Methods utilised for the calculation of natural gas viscosity can be divided into three groups (Erdogmus, Adewumi and Ibraheem 1997). The first group estimates viscosity by empirical correlations using pseudo-critical gas properties calculated from the gas composition or gas molecular weight. In these methods, gas density is generally used to compute viscosity. Hence, the accuracy of the viscosity calculations depends on the choice of the gas mass density estimation method. The second category employs gas composition to predict the gas properties via the method of corresponding states. The third group, and the most recent methods, are based on equations of state (EOS) approach (Guo *et al.* 2001; Guo *et al.* 1997; Lawal 1986). In our study one of these methods was employed, the Lee-Gonzalez-Eakin correlations. In EOS-based viscosity models the mass density calculation is not required for viscosity. Moreover, they also secure stable convergence in the vicinity of the critical point.

Viscosity correlations presented by Lee-Gonzalez-Eakin (LGE), are preferentially used to predict viscosity of sweet and dry gases because of their accuracy and simplicity (Elsharkawy 2002). As a result, most PVT laboratories are using EOS models to report gas viscosities. The LGE gas viscosity correlation used in this study utilises the following equations:

$$\mu_g = D_1 \times 10^{-4} \exp\left(D_2 \rho^{D_3}\right) , \qquad (23)$$

where

$$D_1 = \frac{\left(9.379 + 0.01607 M_g\right) T^{1.5}}{209.2 + 19.26 M_g + T} , \qquad (24)$$

$$D_2 = 3.448 + \left(\frac{986.4}{T}\right) + 0.01009 M_g , \qquad (25)$$

$$D_3 = 2.447 - 0.224 D_2 , \qquad (26)$$

where M_g is the gas molecular weight (g/mol), ρ is the gas mass density (g/cm³), and T is the temperature (ºR) (Elsharkawy 2004).

2.8. Adsorption

The nanosize pores in shales results in a considerably large inner surface area and, hence, adsorption and desorption processes, which depend on the size of the surface area become important (Etminan *et al.* 2014). Adsorption is a surface phenomenon during which gas molecules adhere to a solid surface and form layers via physical or chemical bonds (Foo and Hameed 2010). The adsorption mechanism in shale gas reservoirs refers mainly to physical adsorption, which means that the adsorption is fully reversible, allowing gas molecules to completely adsorb and desorb. Furthermore, the interaction force between the solid surface and the adsorbed gas molecules is controlled by the weak van der Waals forces (Yu, Sepehrnoori and Patzek 2014).

Adsorbed gaseous methane is stored in a liquid-like form, so the overall storage capacity of the rock is enhanced (Tiab and Donaldson 2016). Although gas desorption is a relatively slow process, it can account for 20-85% of the total gas production, especially during the final stages of exploitation (Chen *et al.* 2019; Chen *et al.* 2015; Li, Min*, et al.* 2016). During reservoir depletion, the adsorbed phase is released providing not only additional gas for production but also helps maintain pressure and perhaps maintain open productive pore throats for fluid flow. If the reservoir pressure increases, for example, during water flooding, gas molecules adsorb on the pore walls and that causes the process of gas dissociation to reverse (Sui, Yao and Zhang 2015).

The degree of gas adsorption is a function of the system's pressure and temperature (Sui, Yao and Zhang 2015). At constant temperature, the amount of gas adsorbed on the solid surface is exclusively governed by pressure. This relationship is generally called an adsorption isotherm. At low pressures, only few gas molecules attach themselves to the solid surface (Guo, Wei and Liu 2015). As the pressure increases, more gas tends to accumulate on the pore walls. As it was stated earlier, the bigger the surface area the greater the amount of adsorbed gas, however, the pore size distribution is also important. Pores in shales can be divided into macropores (diameter

exceeds 50 nm), mesopores (diameter ranges between 2 nm and 50 nm) and micropores (diameter is less than 2 nm) (Lee and Kim 2016). In micropores, the adsorption energy from multiple surfaces coalesces leading to an overall increase of the attraction effect relative to the macropores. As a result, materials with a larger micropore volume are usually more adsorptive in nature.

The usual method for assessing the methane adsorption capacity in shale gas is the high-pressure methane adsorption experiments which yield the adsorption isotherms (Li, Min, *et al.* 2016; Zou and Rezaee 2019). In the past, a wide variety of isotherm models has been proposed including the Langmuir, the Freundlich, the Brunauer-Emmett-Teller, and others. For a complete list interested readers may consult Foo and Hameed (2010). Molecular simulations and experimental studies with different shale samples have been extensively utilised to investigate gas adsorption in shale rocks (Heller and Zoback 2014; Li, Min, *et al.* 2016; Zou and Rezaee 2019).

The specific surface area, defined as surface area per gramme of solid, plays an important role in controlling the adsorption capacity. Rough solid surfaces and small pore sizes can yield a larger specific surface area, and, thereby, increase the amount of adsorbed gas (Lee and Kim 2016; Solar *et al.* 2010; Yu, Sepehrnoori and Patzek 2014). Moreover, in smaller pores, the adsorption energy from multiple surfaces coalesces leading to an overall increase of the attraction force relative to bigger pores. As a result, rocks with smaller pores are usually more adsorptive.

The magnitude and profile of the isotherm describing adsorptive potential depends on mineralogy, diagenesis, pore structure and distribution, the amount of organic matter present, gas properties, and external conditions, such as temperature, pressure, etc. (Chen *et al.* 2017; Fan *et al.* 2018; Li, Min, *et al.* 2016; Zhang *et al.* 2017). The relation between shale formation properties and adsorptive potential can be a complicated affair. For example, Ross and Bustin (2007) concluded that shale samples with a relatively high clay mineral content exhibit a low gas adsorption capacity due to the high equilibrium water content. However, the higher the clay mineral content, the larger the reservoir pore space for free gas. Thus, the proportion of clay minerals that are beneficial to shale gas production must strike a balance between the equilibrium water content, which is detrimental to gas adsorption, and the total porosity, which is favourable for free gas storage.

In addition to the adsorption capacity, the isotherm shape plays an important role as observed through the comparison of the samples from the Barnett, in Texas, and the Montney, in Canada. For example, in spite of having a higher capacity for adsorption and a higher Langmuir volume, the adsorption isotherm for the Montney formation sample revealed a higher Lagmuir pressure. In turn, a high Lagmuir pressure allows greater desorption at high pressures and results in a slightly higher production of adsorbed (and therefore total) gas per tonne of rock (Heller and Zoback 2014).

For shale formations, it should be noted that the pore radius expands during gas desorption from the pore wall. Taking into consideration the gas adsorption/desorption, the effective pore radius can be expressed as:

$$r_{eff} = r_{max} - d_{CH_4}\left(\frac{P/P_L}{1 + P/P_L}\right).$$

(27)

Here, r_{eff} is the radius of the pore with adsorbed gas molecules on its walls (nm), d_{CH_4} is the molecular diameter of methane (nm), P is the absolute pressure (Pa), P_L is the Langmuir pressure (Pa), and r_{max} is the pore radius without any adsorbed gas molecules (nm). As the reservoir pressure drops during the production phase, gas molecules desorb from the pore walls. Therefore, as one can observe from equation (27) the pore radius is increasing with production which allows gas to flow more easily. In contrast, if the reservoir pressure increases, for example during water flooding, gas molecules adsorb on the pore walls and that causes the process of gas dissociation to reverse.
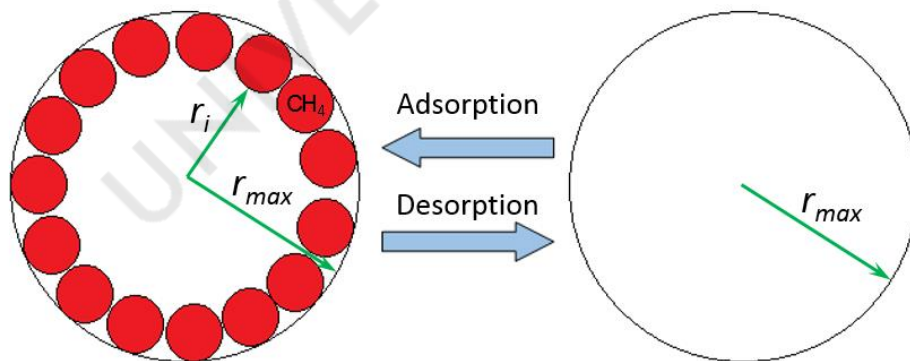
Figure 10. Variation in pore radius due to gas adsorption/desorption. Modified from Guo, Wei and Liu (2015).

Figure 10 depicts the mechanism of gas adsorption and desorption. For the ideal scenario when the reservoir pressure diminishes to nearly 0, the effective pore diameter will reach the maximum value (r_{max}). Moreover, it should be noted that during gas desorption the gas transport channels enlarge and that results in different flow contributions from the various mechanisms, namely, viscous flow, flip flow, Knudsen diffusion and velocity changes. Although an increase in pore radii due to gas desorption is not significant, under the given reservoir conditions, it can exert a disproportionate effect in the size and geometry of the pore throats which are much smaller than the pores (Guo, Wei and Liu 2015).
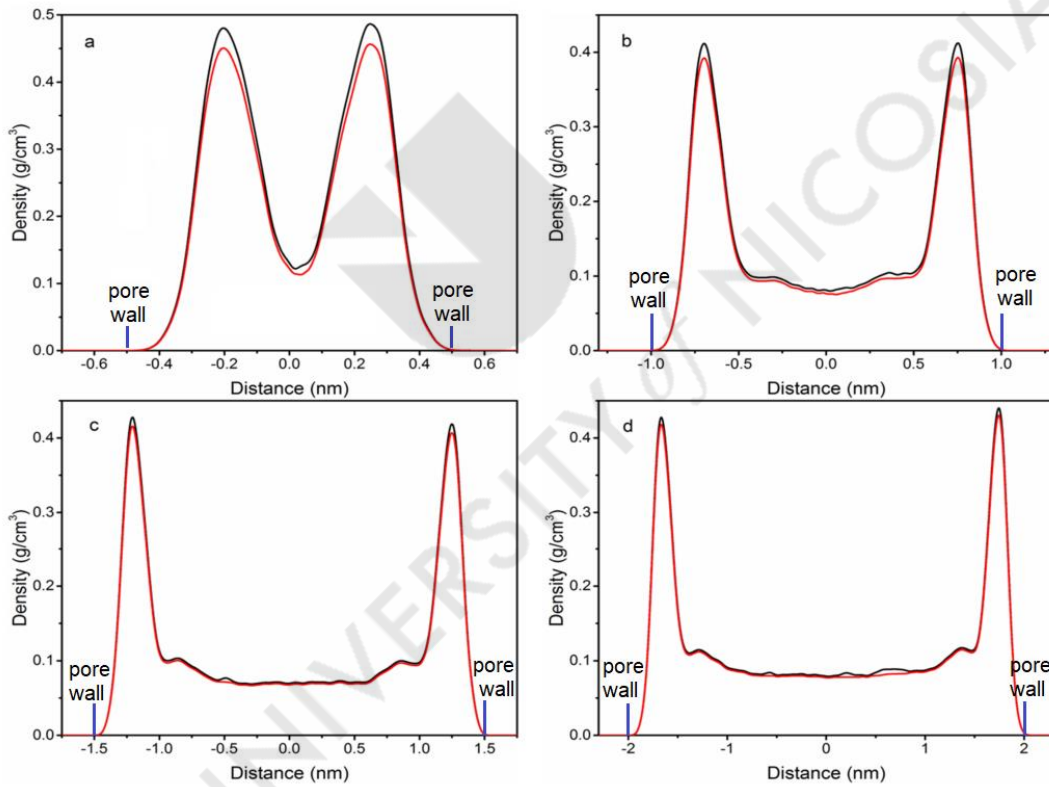
Figure 11. Methane density profiles in shale pores with different sizes at a pressure of 8 MPa and temperature of 298 K. Pore diameters considered comprised: (a) 1.0 nm, (b) 2.0 nm, (c) 3.0 nm and (d) 4.0 nm. Adapted from: Sui, Yao and Zhang (2015).

With respect to adsorption, the gas density in the pores is not uniform. Figure 11 presents the mass density profiles for CH_4 in nanopores for different pore sizes at a

pressure of 8 MPa. The density profiles for all pore sizes exhibit a pronounced peak near the pore wall, where adsorption takes place, and at a reduced and often extensive region peripheral to the centre. The maximum methane density of the adsorbed layer will drop with increasing pore size. This is because the smaller the pores, the more the walls affect the superimposition and enhancement of CH_4 sorption. As the pore sizes increase and the combined effect becomes smaller or vanishes, the density of the adsorbed CH_4 layer drops until it reaches the bulk limit (Sui, Yao and Zhang 2015). Moreover, the thickness of the adsorbed gas layer shrinks. The adsorption process was explored more thoroughly for methane gas. However, the effect described above was also observed for natural gases with different compositions (Esteves *et al.* 2008).

3. Numerical simulation

This chapter is dedicated to the modelling methods. Here we discuss the modelling procedure, how the computational mesh is constructed and how fluid and rock properties are assigned to the cells. The equations governing flow in the constructed model are also presented. Furthermore, we proceed to explain the discretisation methods and discuss the modelling software which solves the equations of flow numerically within the computational domain. The flow equations and initial and boundary conditions for the model have been presented. In conclusion, the constructed model's parameters, initial and boundary conditions are listed and analysed.

3.1.   Modelling of the shale pore network

The complexity of shale gas systems, the diversity of the flow processes, the limitations of the experimental techniques, and the impossibility of obtaining direct pore-scale observations have made it difficult to study these systems through the application of traditional averaging approaches (Raoof and Hassanizadeh 2010). Hence, pore-scale modelling of the subsurface flow systems is an important issue today since it can explain the macroscopic behaviour by accounting for the pertinent physics at the pore level (Sheng and Thompson 2013). In order to produce realistic predictions, pore network models require accurate descriptions of the morphology of real porous media and consideration of the shale distinguishing features (Coelho and Neumann 2016; Raoof and Hassanizadeh 2010).

Pore geometry and pore surface characteristics have a major influence on gas storage, transport, and flow in porous media. Apparently, the shale porous structure cannot be represented by an average porosity value since it consists of pores with different shapes and sizes which are connected by contracting and diverging tortuous pathways (Firouzi, Rupp, *et al.* 2014). For example, in multiphase flow, methane (non-wetting fluid) may be completely surrounded by water (wetting phase) and in this way gas may be trapped so no further movement will be possible through capillarity-controlled displacement. Distribution of the pores in a shale matrix and the shape of these gas blobs can significantly affect fluid transport in shale reservoirs. Therefore, it

is imperative to ensure that a computational model captures the principal features and characteristics of the pore geometry of the shale matrix (Raoof and Hassanizadeh 2010). In addition, the tortuosity of the pores, the appearance of the pore throats which are much smaller than the parent pores and their poor connectivity may lead to insufficiently accurate models featuring simple porous media geometries.

In shale gas reservoirs, pore-scale processes govern the fundamental behaviour of multi-phase, multi-component porous media systems. Ignoring one of these factors, such as the slippage effect, Knudsen diffusion, adsorption/desorption and variations in natural gas flow characteristics, would result in incorrect gas flow calculations. Therefore, it is crucial to incorporate these factors into the models in order to obtain a more accurate shale gas flow prediction, and accordingly to estimate gas production. Since there is no field or core investigation data which translate into pore scale modelling results, a common method to verify the level of accuracy of these approximations is to compare the results of numerical simulations with analytical findings (Guo, Wei and Liu 2015).
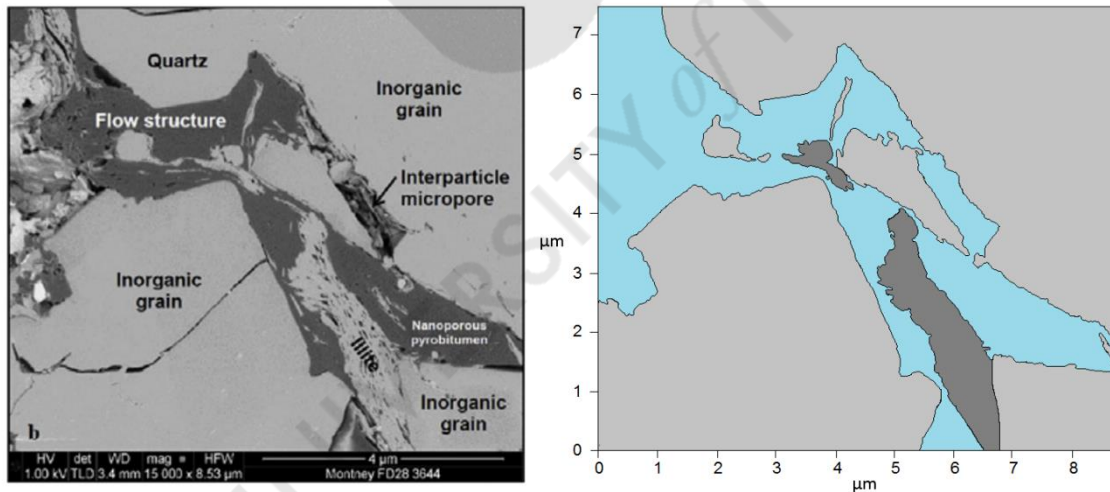
Figure 12. Left inset portrays an SEM-image of a shale pore-flow structure (Clarkson *et al.* 2016). The proposed model (right) bears geometric similarity with the SEM-image. Light grey zones illustrate quartz, darker grey zones display illite, while blue-coloured areas depict pore channels.

As far as this work is concerned, a 2D pore-scale model was constructed drawing inspiration from actual SEM imaging data from Montney formation in Canada, which

incorporates pore size, structure and tortuosity. It is important to construct a model of sufficient geometric accuracy that captures the properties of the porous medium as closely as possible. This is because at the micro- and the submicron-dimensions even the faintest changes in geometry can result in considerably different computational or mathematical models. Consequently, the SEM image was converted into a contour plot which was, subsequently, transformed into a vector image. This vector image which constituted the geometrical model was then discretised into a computational grid of the shale porous medium to which the fluid and rock properties were assigned. Both the SEM-image and the constructed model are presented in Figure 12. Quartz occupies the lightly grey coloured domain, illite is depicted in dark grey colour and the pore channel is shaded in blue.

3.2.   Governing equations

The theory of flow through a porous medium is based on the conservation laws:

- The mass of a fluid is conserved. That is, there is no unaccounted mass loss or gain in the system;
- The time rate of change of momentum equals to the sum of the forces acting on the fluid (Newton's second law).

Bearing in mind that the shale pore dimensions are in the nanometre range, in this research investigation their aggregate effect has been approximated to the micro-level through volume-averaged quantities. The volume averaged conservation equations for mass and momentum used in this study are presented in the sequel (Chen 2000; Coats 1980).

Conservation of Mass

The equation of mass conservation within a porous medium is given by:

$$\frac{\partial}{\partial t}(\varphi\rho) + \nabla \cdot (\varphi\rho U) = 0 \ , \tag{28}$$

where φ is the porosity of the rock, ρ is the fluid mass density (kg/m^3) and U is the fluid flow velocity (m/s).

Conservation of Momentum

The momentum conservation equation within a porous medium is expressed by:

$$\frac{\partial}{\partial t}\left(\varphi\rho U\right)+\nabla\left(\varphi\rho U\cdot U\right)=-\varphi\nabla P+\nabla\left(\varphi\tau\right)+\varphi F-\frac{\varphi^2\mu}{k}U-\frac{\varphi^3 C_F\rho}{\sqrt{k}}\left|U\right|U \quad , \qquad (29)$$

where φ is the rock porosity, P is the pressure (Pa), μ is the viscosity of the fluid (Pa·s), C_F is the quadratic drag factor, τ is the shear stress (N/m^2), F is the body force vector, U is the fluid flow velocity (m/s), and k is the permeability (mD) (Bettotti 2017). The last two terms in the equation represent an additional drag force acting from the pore walls on the fluid within the pores, and usually leads to a significant pressure drop across the porous rock. In a purely fluid region, when $\varphi\rightarrow1$ and $k\rightarrow1$, equation (29) yields the Navier-Stokes equation (Amao 2007; Kovalchuk and Hadjistassou 2019; Yu, Sepehrnoori and Patzek 2014).

3.3.   Discretisation

As it was discussed before, a shale pore network exhibits an extremely complex structure. Hence, the flow equations cannot be solved analytically and need to be discretised and computed numerically. Having obtained the geometry of the shale formation, we have discretised the computational domain into unstructured triangular elements as illustrated in Figure 13. Considering that the computational model should be sufficiently accurate and yet not very time consuming to yield results, it is important for the model to be able to capture all pores peculiarities at a reasonable computational run time. For that reason, the density of the discretisation mesh is physically and geometrically dependent. In quartz domains, the cells' size is larger since no flow occurs within them. Where the pore channel is narrow, the mesh density is the highest, capturing more accurately the intricate granularity of the gas transport, which permits better modelling of the flow processes.
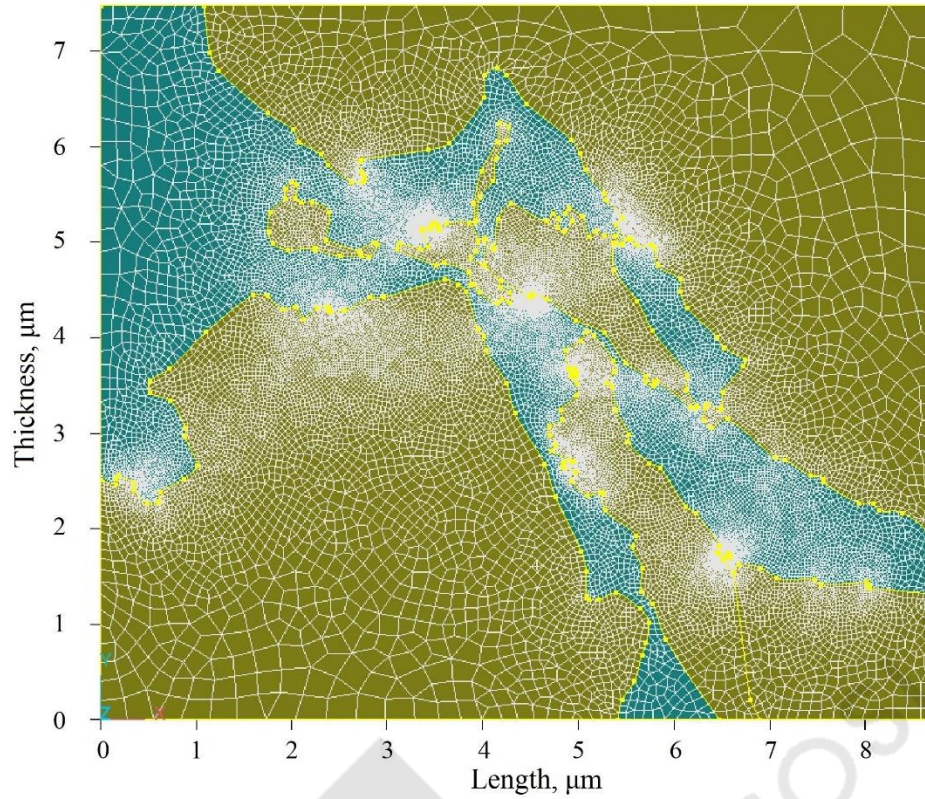
Figure 13. Computational mesh of the pore-scale model of the gas shale matrix.

To ensure that the computational grid is appropriate for the particular modelling task and to converge at a reasonable time period, a grid dependence study has been performed, as shown in Figure 14. It included several grid refinement iterations and the corresponding error estimation for each discretisation mesh. As it can be observed at Figure 14, past iteration 4 further mesh refinements yield no tangible decrease in errors. Therefore, a denser mesh will increase the time required for the model to converge but will not improve modelling accuracy. Leveraging on the grid dependence study, the selected computational grid consists of 122,108 cells.
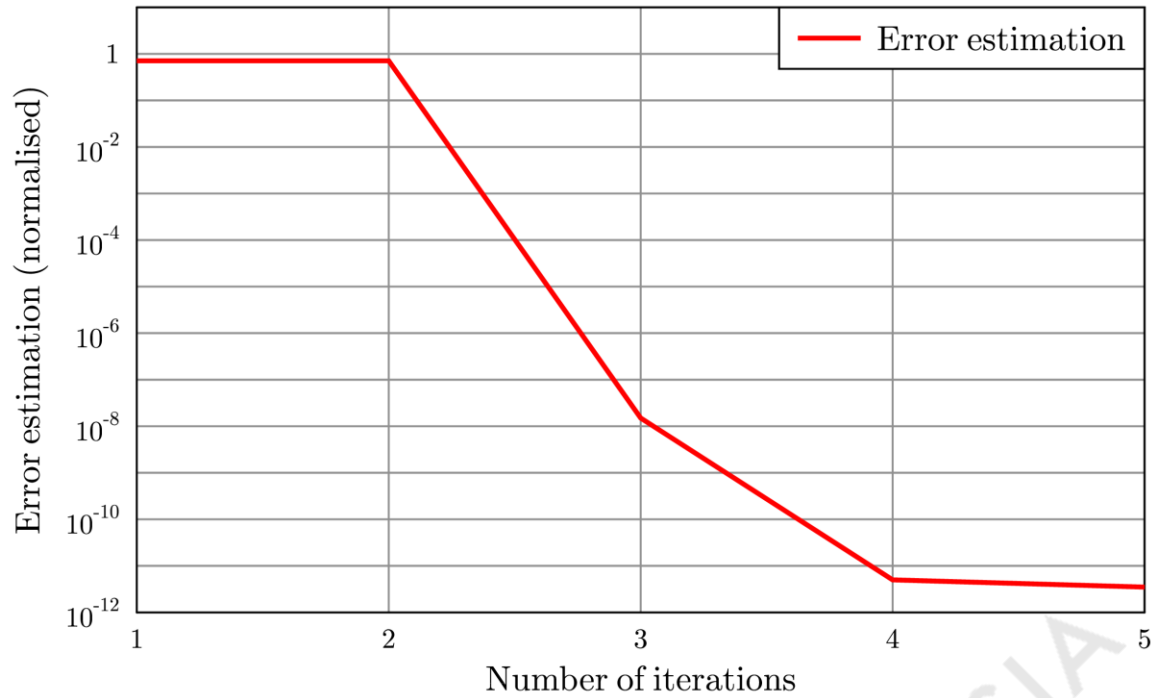
Figure 14. Grid dependence study. The error estimation refers to the different grid refinement iterations.

3.4.   Modelling Software

In the beginning of the research, the CFD-ACE+ platform was used for shale transport process modelling. The multi-physics CFD-ACE+ solver was utilised to model the pertinent physical processes. The Porous Media module in CFD-ACE+ software is suitable for modelling fluid transport in a material consisting of a solid matrix with interconnected voids saturated by fluid (single or multiphase). The porous medium model considers a wide range of physical processes related to porous media and can be used to solve the equations of flow as well as for the analysis of surface reactions inside a porous bed. CFD-ACE+ flow solutions can generate detailed information about the flow field of a given geometry such as the magnitude and the direction of the flow velocity, the pressure distribution, and the fluid mass-density (ESI-CFD 2014; Morales-German, Navarro and Dubost 2012; Morales-German *et al.* 2012).

While the research presented here was progressing, it was decided to shift software to COMSOL Multiphysics since the scope of the research was extended beyond the capabilities of CFD-ACE+. COMSOL is a comprehensive general-purpose

finite element software offering the broad physical modelling capabilities needed to model flow and other related physical phenomena (COMSOL 2017). COMSOL Multiphysics can solve some of the most sophisticated models for single- and multi-phase compressible flows, chemical reactions and combustion and could help gain deeper insights into the complex, often counterintuitive interactions caused by complicated flow processes (Pepper and Heinrich 2017).

Results obtained from CFD-ACE+ are presented in §4.1 "Micro-scale transient pressure and velocity results" and §4.2 "Non-dimensionalisation approach" (ideal gas scenario). Findings determined from COMSOL Multiphysics software are described in sections from §4.2 to §4.5, namely, "Non-dimensionalisation approach" (real gas scenario), "Steady-state pressure and velocity results", "Adsorption modelling results", and "Sensitivity analysis". To ensure that the transition to COMSOL did not affect the accuracy of the model, simulations with the same physical processes and the same parameters and values were performed in both software suites and their results were compared. Both models showed good agreement and demonstrated similar results with the discrepancies between them being insignificant.

3.4.1. CFD-ACE+ discretisation

Once the mesh was constructed, the model was divided into a number of cells also known as control volumes (CVs) (see Figure 15). All space dependent variables and material properties were averaged within each cell and the obtained values were assigned to the entire subdomain and stored at the cells' centres. In other words, these quantities were assumed fixed (constant) within the control volume and equal to the average value of any variable or property within a cell.
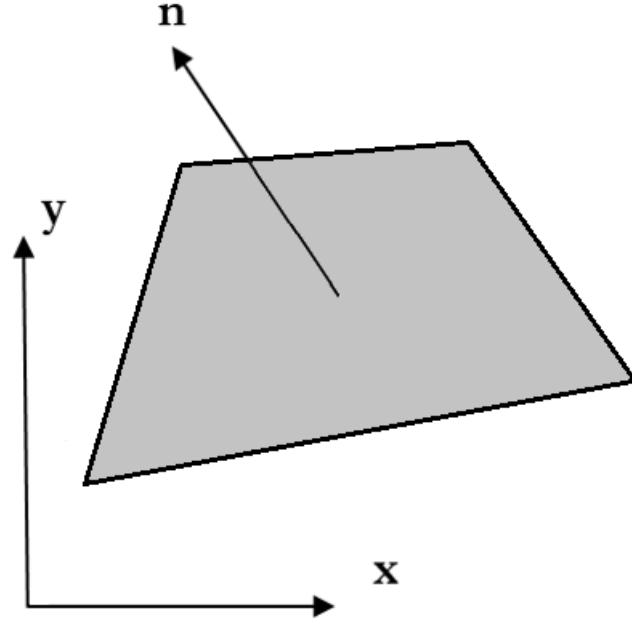
Figure 15. A 2D computational cell (control volume).

The next steps involved casting the governing equations to each of the control volume cells. The integration of the finite difference approximations over each of these computational cells or control volumes generated a set of algebraic equations. Finally, these algebraic relations were solved using suitable matrix solution methods (Hall 1999). An example of a discretisation procedure is demonstrated on the basis of a generalised transport equation:

$$\underbrace{\frac{\partial \rho \varphi}{\partial t}}_{transient} + \underbrace{\nabla \cdot \left(\rho \vec{V} \varphi \right)}_{convection} = \underbrace{\nabla \left(\Gamma \nabla \varphi \right)}_{diffusion} + \underset{source}{S_\varphi} \quad . \tag{30}$$

This equation is also known as the generic conservation equation for a quantity φ. Integrating this equation over a control-volume cell θ, we have:

$$\int_\theta \frac{\partial (\rho \varphi)}{\partial t} d\theta + \int_\theta \nabla \left(\rho \vec{V} \varphi \right) d\theta = \int_\theta \nabla \left(\Gamma \nabla \varphi \right) d\theta + \int_\theta S_\varphi d\theta \quad . \tag{31}$$

Transient Term

The transient term in equation (29) is integrated as follows:

41

$$\int_\theta \frac{\partial(\rho\varphi)}{\partial t} d\theta = \frac{\rho_n \varphi_n \theta_n - \rho_{n-1}\varphi_{n-1}\theta_{n-1}}{\Delta t} \; , \qquad (32)$$

where the subscript *n* denotes the current time step, while subscript *n–1* refers to the previous time step.

Convection Term

The convection term shown in equation (29) discretised as follows:

$$\int_\theta \nabla \bullet \left(\rho \vec{V} \varphi \right) d\theta = \oint_A \rho\varphi \vec{V}\bullet\vec{n}\, dA = \sum_e \left(\rho_e \varphi_e V_e^n \right) A_e = \sum_e C_e \varphi_e \; , \qquad (33)$$

where subscript *e* denotes one of the faces of the cell in question, A_e is the area of face *e*, V_e^n represents the velocity component in the normal direction to the face, and C_e is the mass flux across the face. The value of φ, at control volume faces, was interpolated by employing an upwind scheme.

3.4.1.1. Upwind scheme

In this work, the upwind interpolation scheme was used for casting the partial differential equations. For illustration purposes, let us consider a 2D control volume, as shown in Figure 16. Because the solution variable φ is available only at the cell-centres, the cell-face values of φ need to be interpolated. In this scheme, quantities at cell faces were determined by assuming that the cell-centre values of any field variable represent a cell-average value and hold throughout the entire cell. That is, the face quantities are identical to the cell quantities.
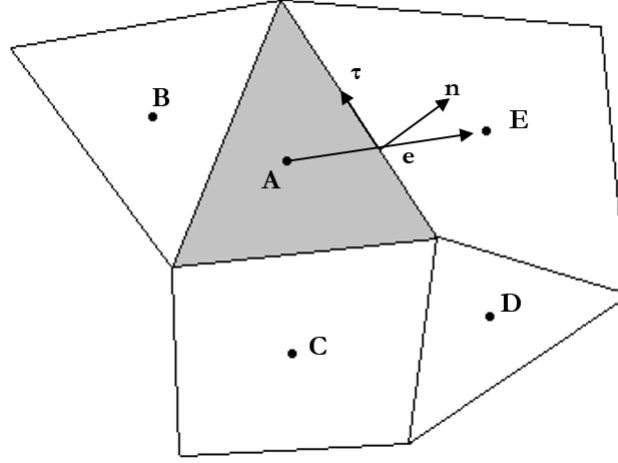
Figure 16. Two-dimensional computational cell for the upwind scheme (ESI-CFD 2014).

Thus, φ_e was taken to be the value of any property φ at the upstream grid point, i.e., φ_e equals to either φ_A or φ_E depending on the flow direction at cell face e. Mathematically, φ at this face can be expressed as:

$$\varphi_e^{UP} = \begin{cases} \varphi_A \ if \ V_e^n > 0 \\ \varphi_E \ if \ V_e^n < 0 \end{cases} \tag{34}$$

As its name implies, this scheme has first-order accuracy and is one of the most stable schemes (Yang and Wei 2017).

3.4.2. COMSOL Multiphysics discretisation

The finite element method (FEM) is a discretisation procedure that can be applied to solve a variety of engineering problems resulting in corresponding numerical models. Firstly, the solution domain is discretised into finite elements which can exhibit different shapes. The finite element method introduces interpolation functions that are defined for each computational cell, or mesh element. Additionally, as part of the finite element method, shape functions are defined to represent the candidate solution. The finite element method provides considerable freedom in selecting interpolation and shape functions for different mesh element types and equations. Depending on the problem, interpolation and shape functions can be linear, quadratic, cubic, etc. This

43

freedom makes the method applicable for complex geometries with "unstructured" meshes, where the size and form of the participating elements can differ greatly.

After establishing the finite element model, the matrix equations expressing the physical mechanisms within the elements were combined to form the matrix equations describing the behaviour of the entire system and the initial and boundary conditions are imposed. That is, the physical equations are approximated by a linear combination of basic functions as demonstrated in Figure 17. Then, the obtained set of partial differential equations which describes the pertinent physical mechanisms and their initial and boundary conditions were solved simultaneously to yield nodal results within the computational region (COMSOL 2017; Pepper and Heinrich 2017). The solution to the PDEs is represented by dependent variables, such as structural displacements, velocity fields, temperature fields, and electric potential fields.
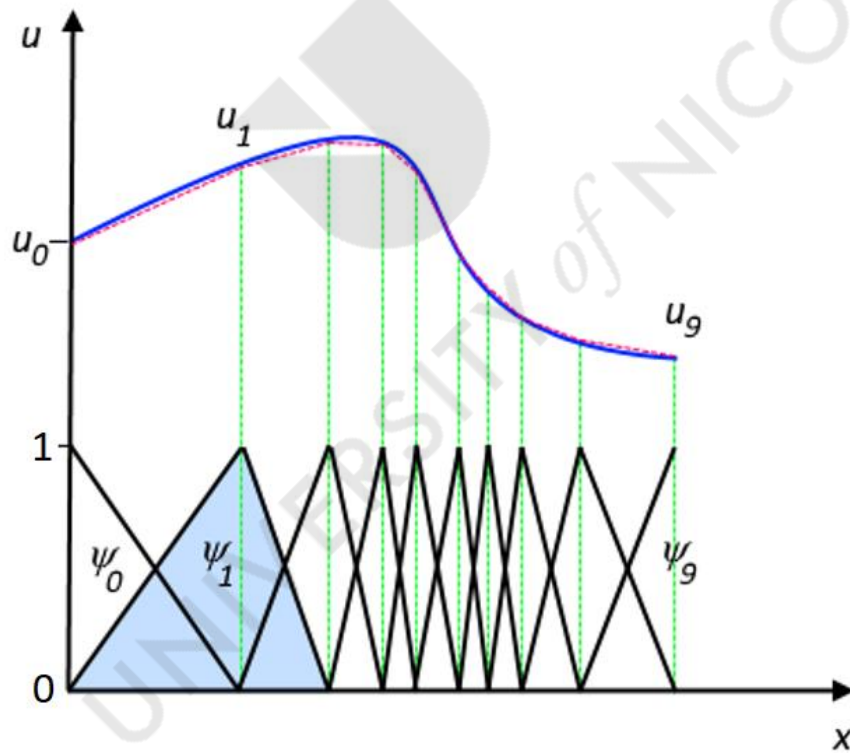
Figure 17. Finite element approximation (is represented by dashed red line) for the function u (is coloured in blue) by combination of basic functions Ψ_i. Adapted from (COMSOL 2017).

3.4.2.1.   Temporal discretisation

For transient simulations, the governing equations need to be discretised in both space and time. Temporal discretisation involves the integration of every term in the differential equations over a time step. A generic expression for the time evolution of a variable φ is given by

$$\frac{\partial \varphi}{\partial t} = F(\varphi) \ , \tag{35}$$

where $F(\varphi)$ is the function of the variable φ. The corresponding discrete form of the equation can be expressed as

$$\frac{\varphi_{n+1} - \varphi_n}{\Delta t} = F(\varphi_{n+1}) \ . \tag{36}$$

For temporal discretisation, a method to evaluate $F(\varphi)$ should be chosen. For the development of the numerical models of this study, an implicit time discretisation method was used. In the method the following relationship was employed, so the next step value can be estimated as follows:

$$\varphi_{n+1} = \varphi_n + \Delta t \cdot F(\varphi_{n+1}) \ , \tag{37}$$

where Δt is the finite time step. This is referred to as "implicit" integration since φ^{n+1} in a given cell is related to φ^{n+1} in neighbouring cells through $F(\varphi^{n+1})$. This implicit equation is solved iteratively at each time step before moving to the next time interval. The benefit of the fully implicit scheme is that it is unconditionally stable with respect to the time step size. In our research the implicit equations were solved utilising Backward Differentiation Formula (BDF) method. This solver uses backward differentiation formulas with variable orders of accuracy. High order equations are used when possible giving advantages in speed and accuracy and automatically switched to lower order when it is necessary to obtain stability.

The explicit scheme formulation implies that once the solution $(T_{i,t})$ is known at a given time, the solution for the next time step $(T_{i, t+\Delta t})$ can be explicitly stated. In other words, for an explicit time-marching scheme, there is no need to solve a system of equations at each time step. The drawback with explicit time-marching schemes is that

in order to realise scheme stability, time-stepping restrictions must be satisfied. In the COMSOL Multiphysics solver, time-stepping algorithms automatically switch between explicit and implicit steps depending on the problem of interest (COMSOL 2017).

3.5.   Parameters of the computational model

Porosity of the shale image was calculated by utilising the point counting software JMicroVision. Firstly, the volume of each mineral was estimated (Figure 12). As it can be noted in Figure 12, illite is characterised by micro-porosity, which is clearly visible on the SEM image. Light grey areas, in the illite zones, were treated as a mineral while dark grey areas, in the same regions, were counted as pores. Notably, the quartz mineral is non-porous in nature other than one fracture which was omitted simply because our model is predominantly concerned with the permeability of the matrix. As it can be observed on Figure 12, shale cement is characterised by nano-porosity which is not discernible on the SEM image. Hence, taking into account the volumetric parts of the quartz, illite and shale cement and the porosity of the minerals, shale cement's porosity was deduced in such a way so the average porosity of the entire model equals to the typical porosity value for Montney formation (Ghanizadeh *et al.* 2018).

Obtaining accurate permeability values for a particular porosity magnitude in shales is not easy undertaking compounded also by a limited number of permeability investigations. Moreover, different formations can have different permeability values for the same porosity level (Bloshanskaya *et al.* 2017). Considering that the SEM image (Figure 12) used to construct the computational model originated from the Montney formation, Canada, a Montney porosity-permeability correlation (Egbobawaye 2013) was utilised to deduce the respective permeability of the model (see Figure 18).
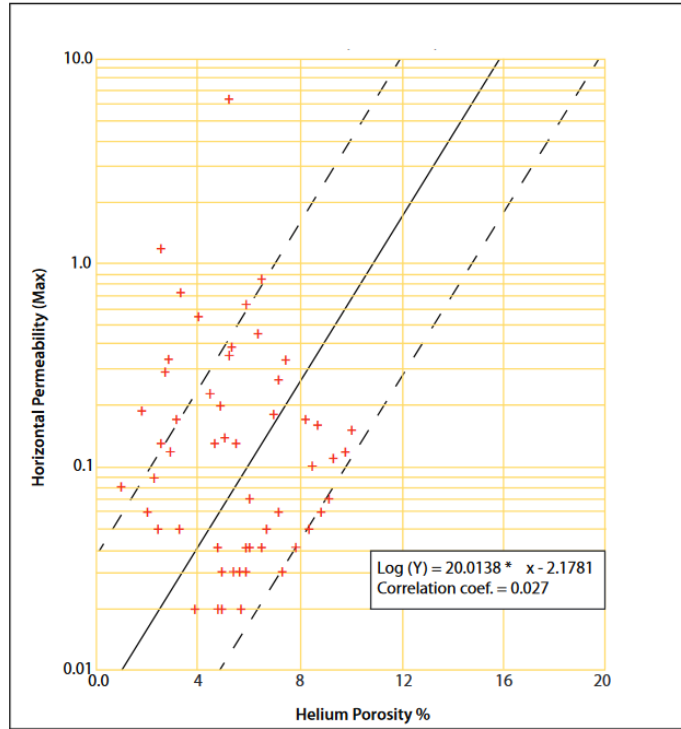
Figure 18. A porosity-permeability relationship for Montney formation. Courtesy: Egbobawaye (2013).

In the model, illite is characterised by a porosity of 24.2% while shale cement exhibits a porosity of 19%. Due to nano-size of the pores, gas permeability is strongly related to reservoir gas pressure, as it was firstly stated by Klinkenberg (Firouzi, Alnoaimi, *et al.* 2014) and was elaborated in further studies (Fathi, Tinni and Akkutlu 2012) (please refer to §2.5.3 "Klinkenberg permeability", page 22). The apparent permeability does not remain constant during different stages of shale gas production (Zhang *et al.* 2015). Consequently, permeability assigned for the constructed model obeys equation (14). For illite, a liquid permeability was set to 5.64µD and shale cement was characterised by a liquid permeability of 1.82µD.

Reference pressure was set to 275.8 bars (27.58 MPa), in line with reservoir conditions in the Montney formation. Gas viscosity was calculated from the Lee-Gonzalez-Eakins methodology based on pressure, temperature and gas composition (see §2.7 "Viscosity", page 27) (Elsharkawy 2004). Unless otherwise stated, the modelled gas was methane. Modelling results for the gases with different composition are considered in sections §4.2 (pages 68-69) and §4.5 (pages 87-88). Initial

47

temperature was set to 353.15K and was maintained constant throughout the entire model and invariant during modelling runs.

Collectively, the initial temperature of 353.15K and the preceding pressure conditions yielded Knudsen numbers ranging from 0.00626 to 0.125 which correspond to slip-flow, as illustrated in Figure 6. To take into account slip flow behaviour, slip boundary conditions for the pores have been applied. For more details please refer to §2.5.4 "Slip boundary conditions for the Navier-Stokes equations" at page 24.

4. Research findings

This chapter is dedicated to the research results. The steady-state and transient modelling results are presented and analysed here. The obtained results are validated by analytical solutions and real data from shale core measurements. Firstly, the modelling results have been compared with analytical solutions of flow in nano-pores. After that, modelling results have been validated against core investigation data as the constructed model, at such, is based on real SEM micro-image data and reflects flow processes in a small unfractured piece of rock. For that reason, a non-dimensionalisation approach has been developed which enables the comparison of simulation results with core measurements several orders of magnitude larger in spatial scale. Finally, the sensitivity analysis of the constructed model has been conducted to identify the reservoir and fluid properties govern flowrate the most.

4.1.   Micro-scale transient pressure and velocity results

The main goal of the transient modelling part of this study was to gain new insights pertaining to the flow behaviour in the pore network. For that reason, we simulated the field behaviour at the microscopic level and reproduced the natural gas depletion scenario complying with the computational model. That is, we imposed wall boundary conditions for the entire model except for one outlet which emulates the reservoir (element) production output.

Reference pressure was set to 275.8 bars (2.758×10^7 N/m^2). This pressure value could be added to any gauge pressure input to calculate the absolute pressure. Initial pressure was selected based on the required pressure difference and the initial temperature was set to 353.15K. Figure 19 shows the model's boundary conditions. Note that no fluid flow manifests through the inlet and outlet 1. Fluid efflux occurs only at "Outlet 2" with boundary pressure 0 N/m^2. Temperature was maintained constant throughout the entire model and remained invariant during modelling. A time step sensitivity study has been performed which identified a time step of 10 nanoseconds (10^{-8} s) as the most appropriate to maintain balance between modelling accuracy and computational efforts. The modelling parameters are considered in detail in §3.5 "Parameters of the computational model", page 46.
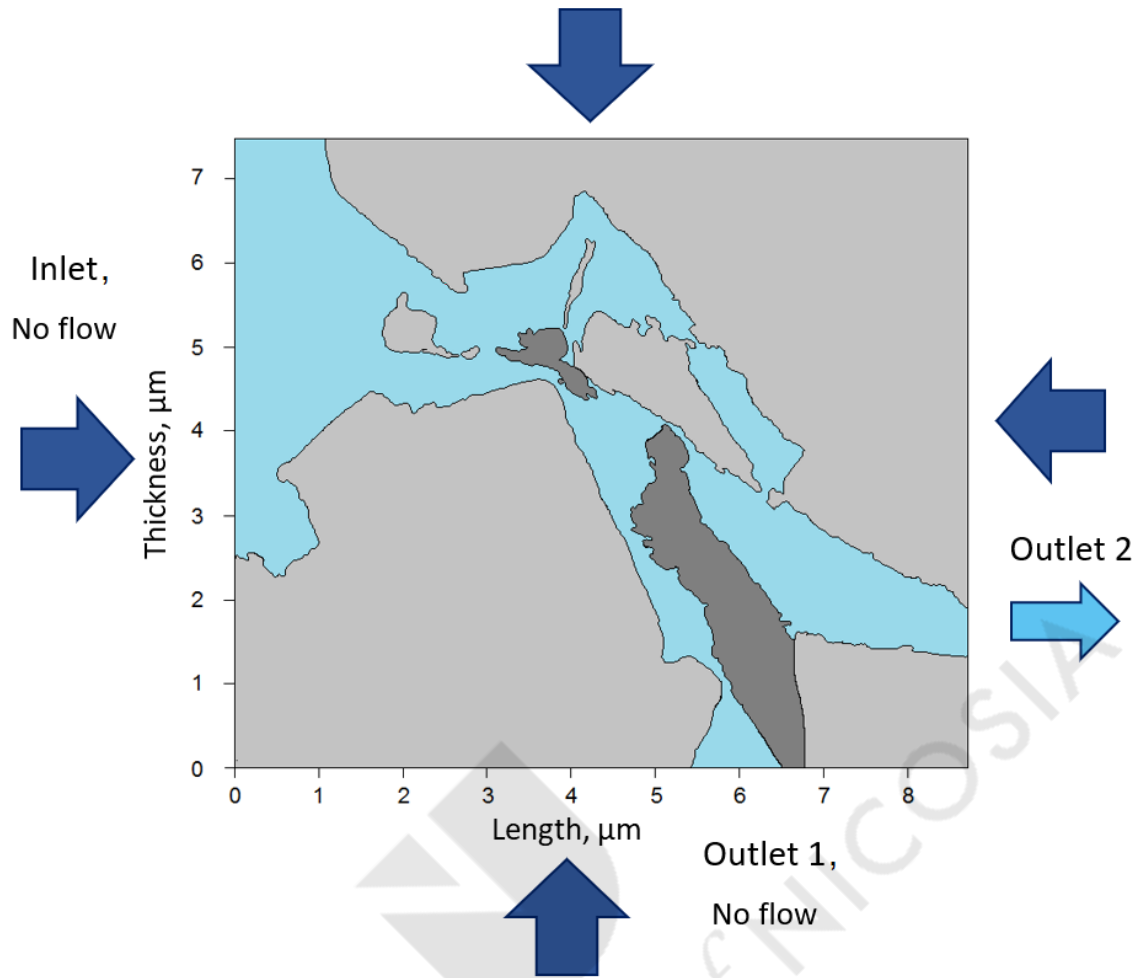
Figure 19. Boundary conditions of the transient flow model. Light grey zones illustrate quartz, darker grey zones display illite while blue coloured areas depict pore channels filled by shale cement. Dark blue arrows indicate confining pressure and light blue arrow denotes the fluid flow direction.

Microscale numerical simulations can provide the opportunity to investigate flow processes manifesting inside a shale matrix. For that reason, the points have been deliberately selected to probe a number of possible phases which can occur in a given porous medium during the depletion scenario. These point locations permit us to gain insights into the behaviour of the pressure and the velocity magnitude changes difficult to obtain experimentally. In Figure 20, the monitoring locations for the second model are presented. Here, 3 points have been selected with Point 1 being just near the outlet, Point 2 at the middle part of the model and Point 3 located closer to the model's far field.
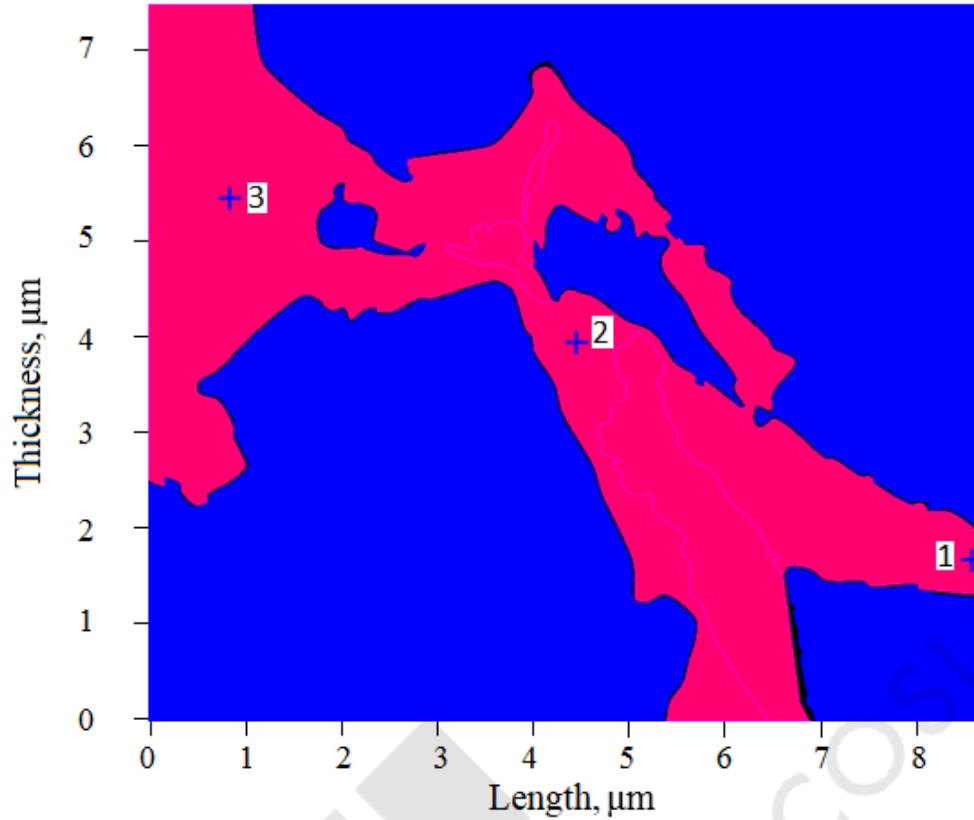
Figure 20. Probing locations of the model with porous illite denoted by the blue crosses and numbers 1, 2, and 3. Red colour displays the pore channel and porous illite where gas flow manifests while blue colour indicates impermeable quartz.

Plots from Figure 21 to Figure 23 display pressure profiles for the different locations as indicated in the computational model (Figure 20). Time is normalised to the whole period of flow, that is, the normalised time interval equals unity in each individual case. As it can be seen from the plots, the pressure profile in the near outlet point (Point1) is characterised by a steep decline. Moving inwards, the pressure profile at Point 2 becomes smoother decaying exponentially. Propagating further, the pressure at the far location (Point 3) exhibits a slow reduction in the flowrate value at the beginning. This is due to the time it takes during the depletion situation for the pressure drop to permeate to the distant part of the rock sample at the micro-level or of the field at the macro-scale.
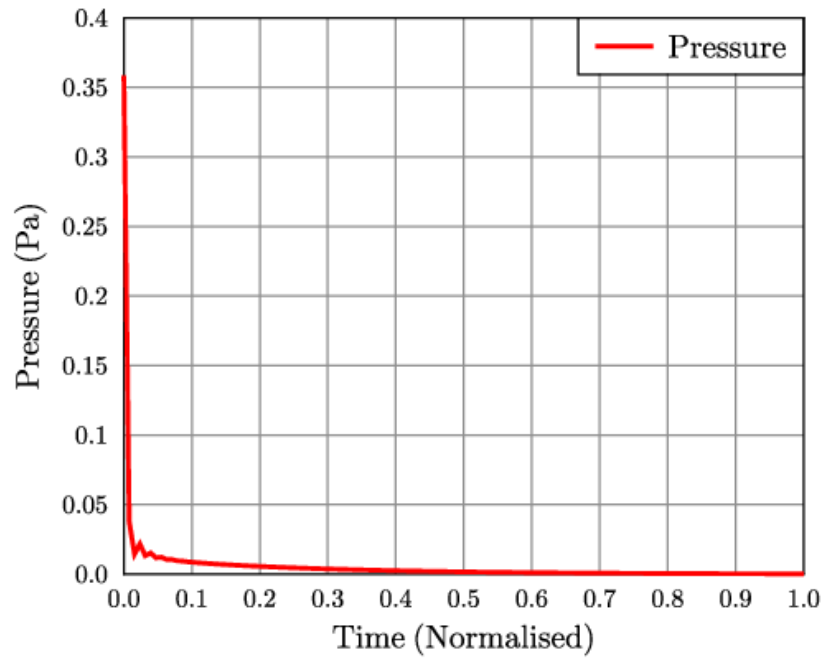
Figure 21. Pressure profile at the near field (Point 1, Figure 20) of the model with porous illite.
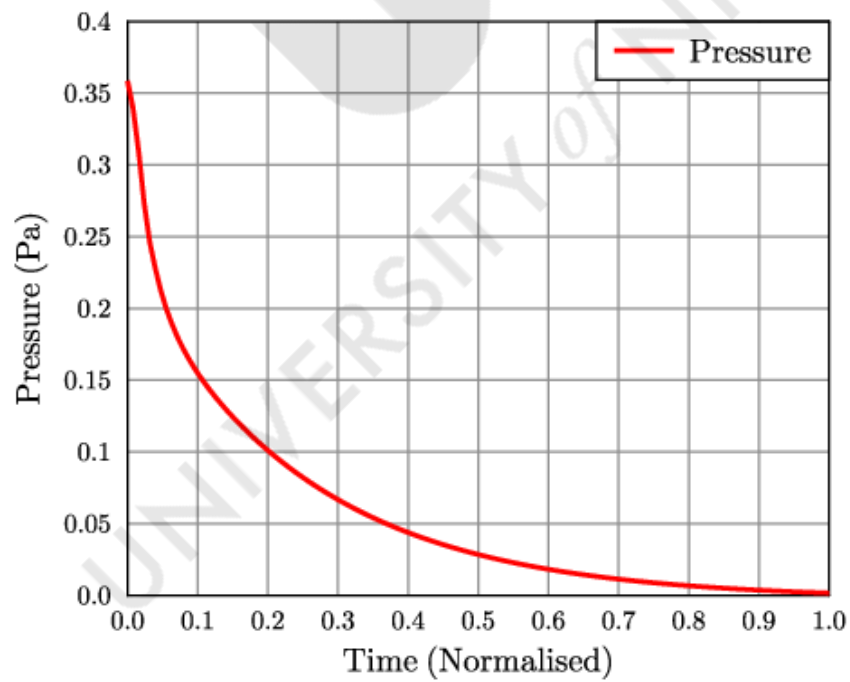
Figure 22. Pressure change at the medium location (Point 2, Figure 20) of the model with porous illite.
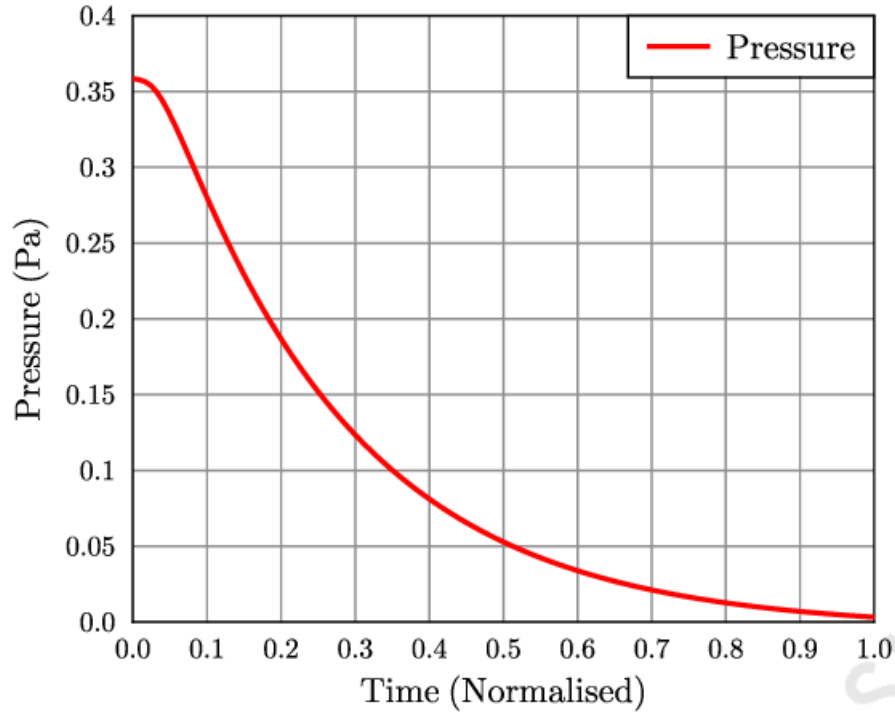
Figure 23. Pressure variation at the far area (Point 3, Figure 20) of the model with porous illite.

Next, Figure 24 to Figure *26* demonstrate the velocity magnitude profiles for different locations of the computational model. With regard to Point 1 (please refer to Figure 20) natural gas undergoes a sharp boost in velocity. The velocity magnitude profiles at the medium (Point 2) and far (Point 3) spatial locations are gentler. However, they are characterised by the same features as the velocity profile of Point 1: growth up to the maximum peak and gradual decrease up to the end. Moreover, as it can be seen in Figure 26, a very small wiggle appears at the beginning of the velocity magnitude profile at the far point (Point 3). This behaviour manifests because of a fast paced pressure gradient between the middle and the far parts of the model. The presence of a channel narrowing at the centre of the model, which acts as a flow restriction, results in faster pressure changes in the centre of the model than in the far field from outlet (please see Figure 22 and Figure 23 for the comparison of the pressure profiles).
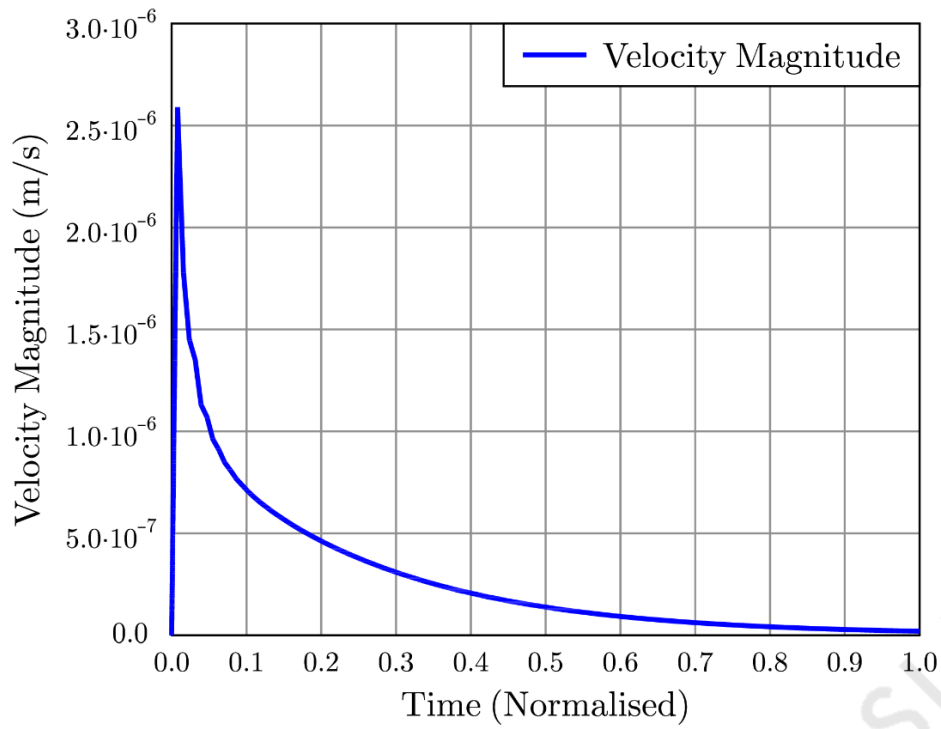
Figure 24. Velocity magnitude profile at the near field denoted by the cross (Point 1) of the model with porous illite (please see Figure 20). Velocity magnitude is a scalar velocity value, in simpler terms, the speed.
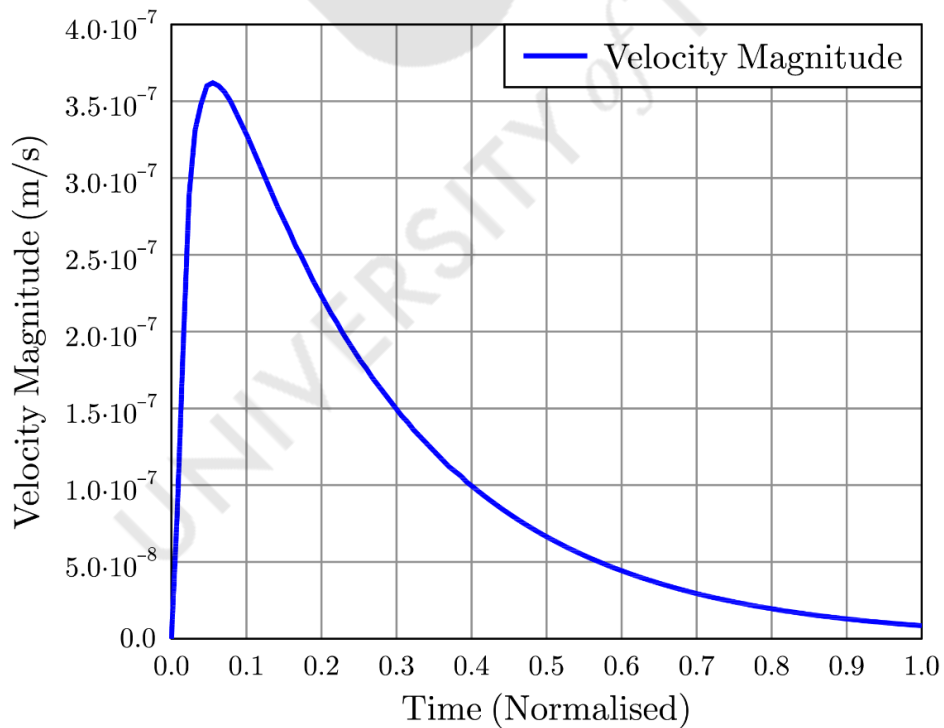
Figure 25. Velocity magnitude profile at the medium location (Point 2) of the model with porous illite (please refer to Figure 20). Velocity magnitude is a scalar velocity value, in simpler terms, the speed.
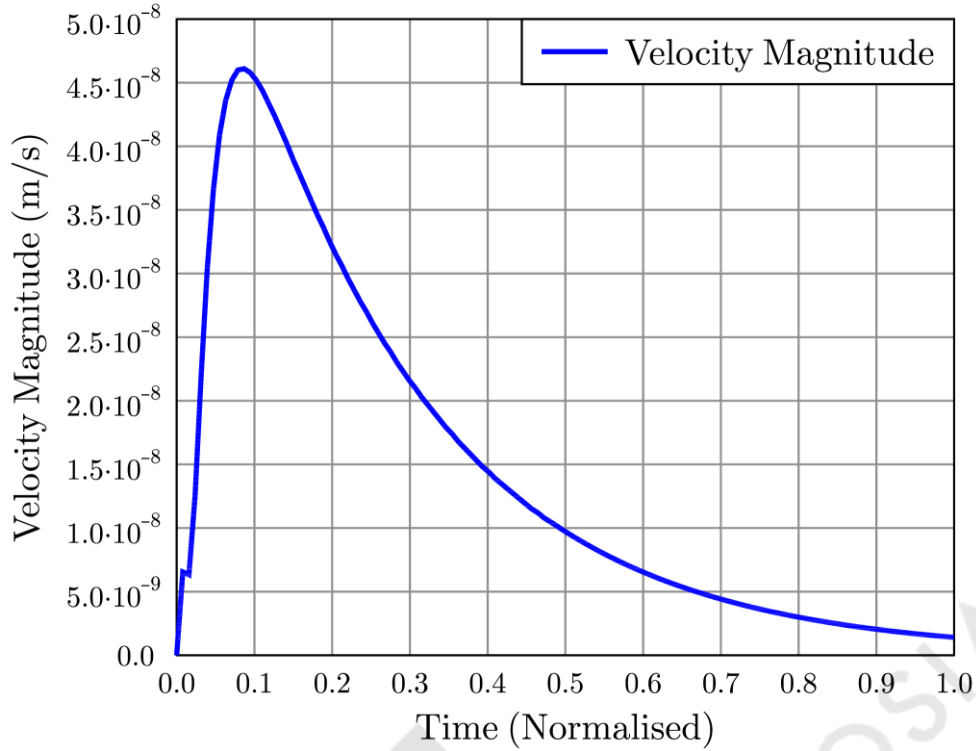
Figure 26. Velocity magnitude profile at the far area (Point 3) of the model with porous illite (please consult Figure 20). Velocity magnitude is a scalar velocity value, in simpler terms, the speed.

Since we were unable to trace any field or core investigation data at the microscale to compare with our modelling results, we opted to relate the numerical modelling results with theoretical findings (Guo, Wei and Liu 2015). For validation purposes we compared the modelling results with calculated flowrates in nano-size capillaries for various Knudsen numbers. Ren *et al.* (2015) suggested a range of gas flow velocities, in nanopores, for different Knudsen numbers at a pressure gradient of 0.1 MPa/m. Making use of the same pressure gradient of 0.1 MPa/m we have developed a validation framework, as presented in Figure 27, which facilitates the verification of numerical results with theoretical predictions. Similarly, to make possible the comparison of numerical versus analytical results the model's Knudsen number was maintained the same as the Knudsen number of the flow in nanopores.
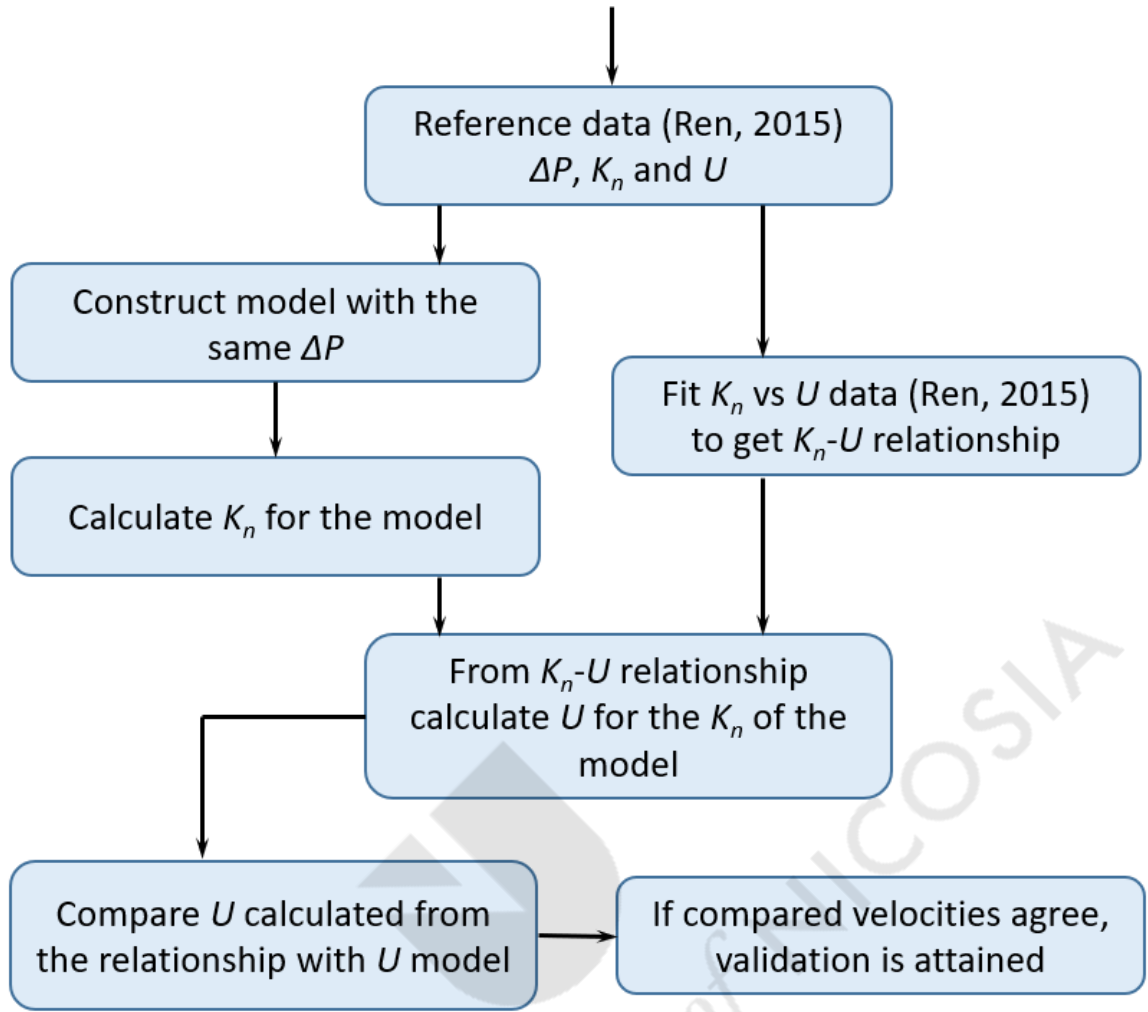
Figure 27. Algorithm for the validation of the computational results. ΔP is the pressure difference between the inlet and the outlet of the computational model (Pa), K_n is the Knudsen number, U is the flow velocity (m/s).

The relationship between velocity magnitude and Knudsen number was obtained from a curve fitting exercise applied to the data (Ren *et al.* 2015), as shown in Figure 28. Flow velocity in nanopores, for the corresponding Knudsen number, as obtained from (Ren *et al.* 2015) was calculated from:

$$U = 1.854 \cdot 10^{-10} \cdot K_n^{-1.758} \quad . \tag{38}$$
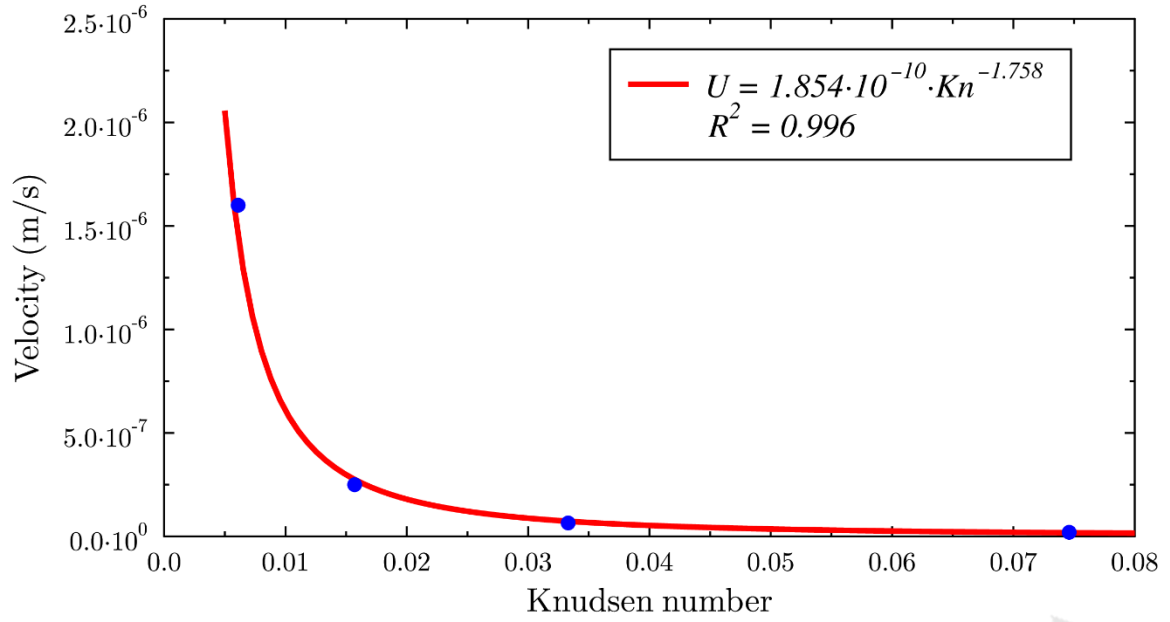
Figure 28. Knudsen number-velocity relationship for flow in nanopores. Pressure gradient amounts to 0.1 MPa.

For the model proposed herein and the Knudsen number range, gas flow velocity ranged between $7.2 \cdot 10^{-9}$ m/s and $1.4 \cdot 10^{-6}$ m/s. Notably, the Knudsen number obtained from the average pore diameter value, yielded a gas velocity of $6.1 \cdot 10^{-7}$ m/s which almost matched the model velocity at all regions. An exception to this agreement in velocity were the pore channel throats which acted as flow restrictions (please see Figure 29). According to the colour contours of the model, the maximum velocity magnitude in the pore channel (except the narrowest part of the pore channel) is $1.2 \cdot 10^{-6}$ m/s which are shown in the yellow colour zones. Noticeably, for most model areas (please refer to Figure 29), flow velocity ranged between $2 \cdot 10^{-7}$ m/s (light-blue colour) and $8 \cdot 10^{-7}$ m/s (green colour). In summary, the validation process is concisely explained in Figure 27.
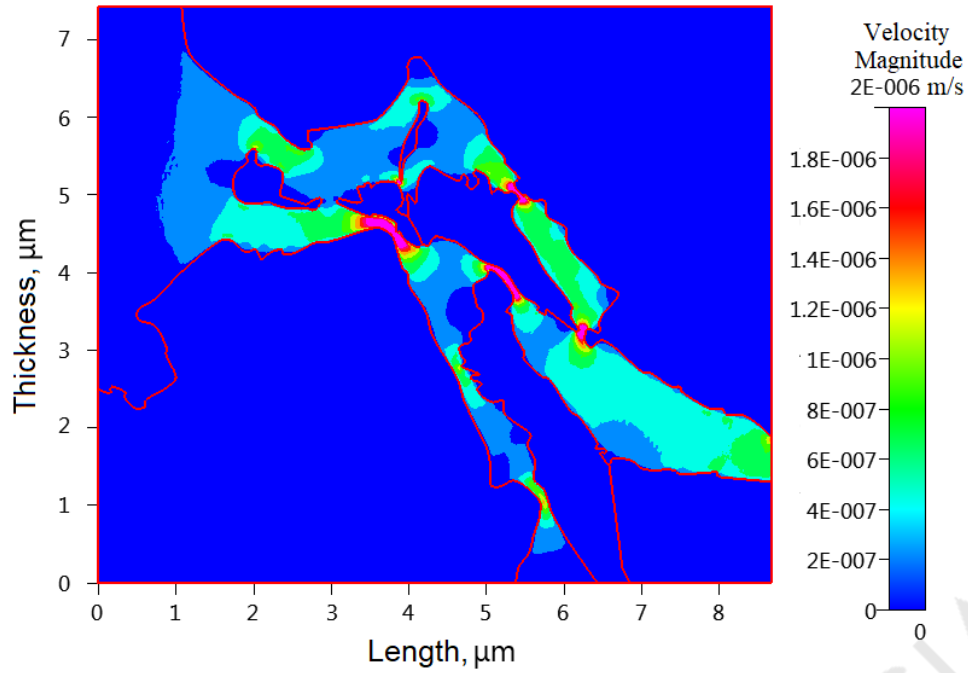
Figure 29. Velocity distribution contours obtained from the numerical model with a pressure gradient of 0.1 MPa.

4.2. Non-dimensionalisation approach

Although analytical solutions are widely employed for verification of nano- and microscale numerical simulations, comparing modelling results with actual data bears more practical significance. Actual data could be well production measurements from a gas shale field or a shale core investigation data of credible nature, i.e., trustworthy. Volume flowrate is either measured at the oil/gas field or during laboratory core measurements. Hence, to facilitate the comparison of model results with real data, the velocity magnitude should be converted into volume flowrate.

Here, it is key to compare model data with intact shale sections without any natural or induced fractures. Hence, it is not recommended to compare our results with well production data. This is because well flow derives from the sum of different flow streams originating from hydraulic fractures, induced natural fractures and the matrix. Apparently, these component streams cannot be decoupled and output flow from the matrix is difficult to be distinguished. Instead, it is deemed appropriate for model

validation purposes to utilise shale core experimental measurements which do not feature natural or induced fractures.

Bearing similarity with the core sample, the numerical model exhibits a cylindrical shape. To convert velocity magnitude from the 2D model into 3D volumetric flowrate, the outlet area of the computational domain was proportionally scaled in relation to the outlet size of the model thickness. To this end, the gas volume flow can be calculated from:

$$q(t) = U(t) \cdot t_{step} \cdot A_{outlet} = U(t) \cdot t_{step} \cdot \frac{d_{outlet}}{h_{model}} \cdot \pi \left(\frac{h_{model}}{2} \right)^2 \qquad (39)$$

where U is the fluid flow velocity (m/s), t_{step} is the computational time step (s), A_{outlet} is the outlet area (m^2), and (d_{outlet}/h_{model}) is the ratio of the outlet diameter to the model thickness. The pertinent dimensions of the model are illustrated in Figure 30. Data related to the velocity at the outlet have been obtained from transient modelling results, as plotted in Figure 24, and the time step was taken to be 10 ns. The cumulative gas flow can be determined by aggregating the volume flow from a step-by-step sequence.
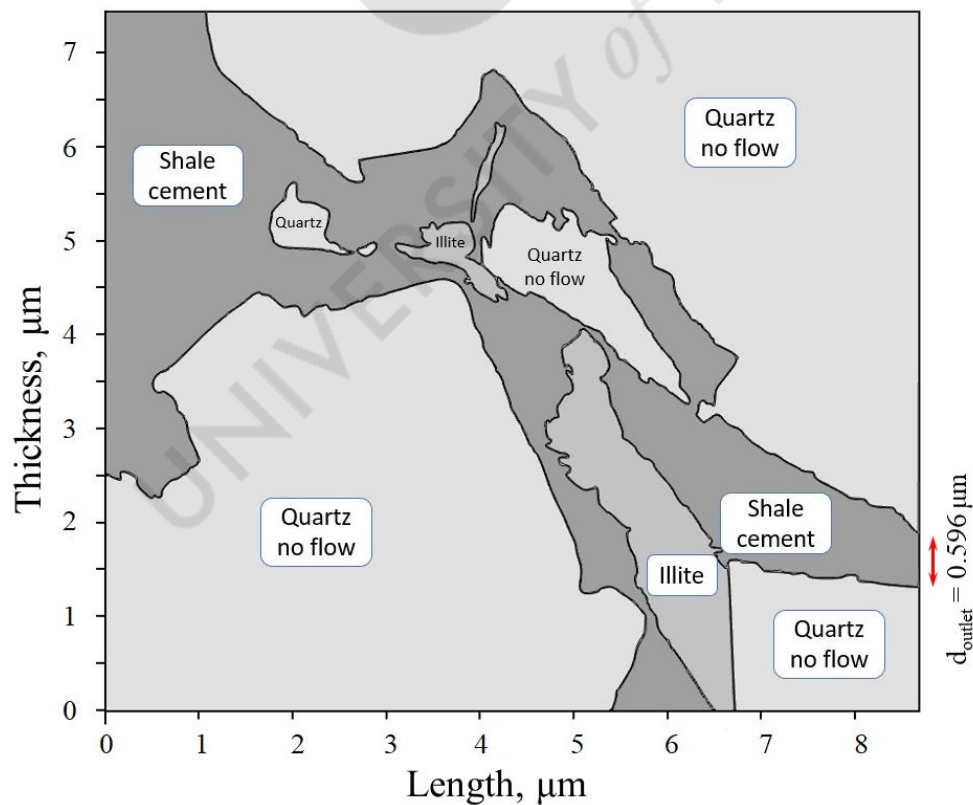
Figure 30. Computational model structure and dimensions.

This work employed gas production test measurements for the validation of the numerical modelling results. Figure 31 and Figure 32 present the cumulative gas flow data for the shale core for production pressures of 0.1 MPa, 10 MPa and 15 MPa. Pressure difference for the specific gas production test scenarios was calculated as a variation between the initial and production pressures. Table 2 lists the parameters of the core samples. For comparison purposes, the cumulative production of free gas has been used, as in the model only free gas is present.

Table 2. Core samples' parameters.

Parameter	Core 1	Core 2	Core 3	Core 4
Length (cm)	2.48	1.47	4.8	4.52
Diameter (cm)	2.51	2.54	2.52	2.52
Bulk volume (cm^3)	12.27	7.45	23.94	22.54
Porosity[1] (%)	2.60	5.37	6.71	8.50

[1]Calculated from the pressure pulse decay method (Sang *et al.* 2016).
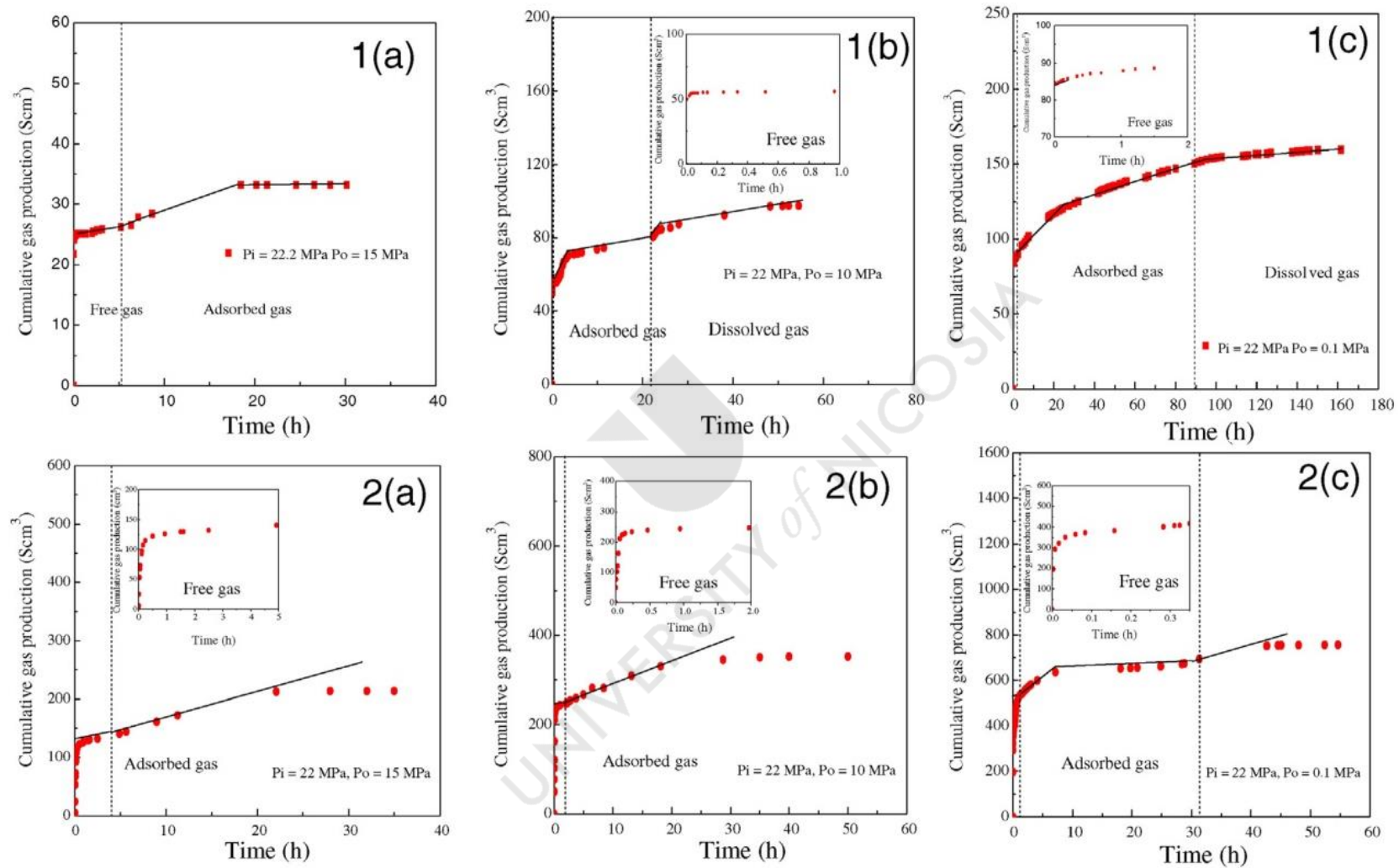
Figure 31. Core investigation data for samples 1 (up) and 2 (down). Initial pressure (P_i) for both samples is 22 MPa. Production pressures (P_0) are: a) 15 MPa, b) 10 MPa, and c) 0.1 MPa. Source: Sang *et al.* (2016).
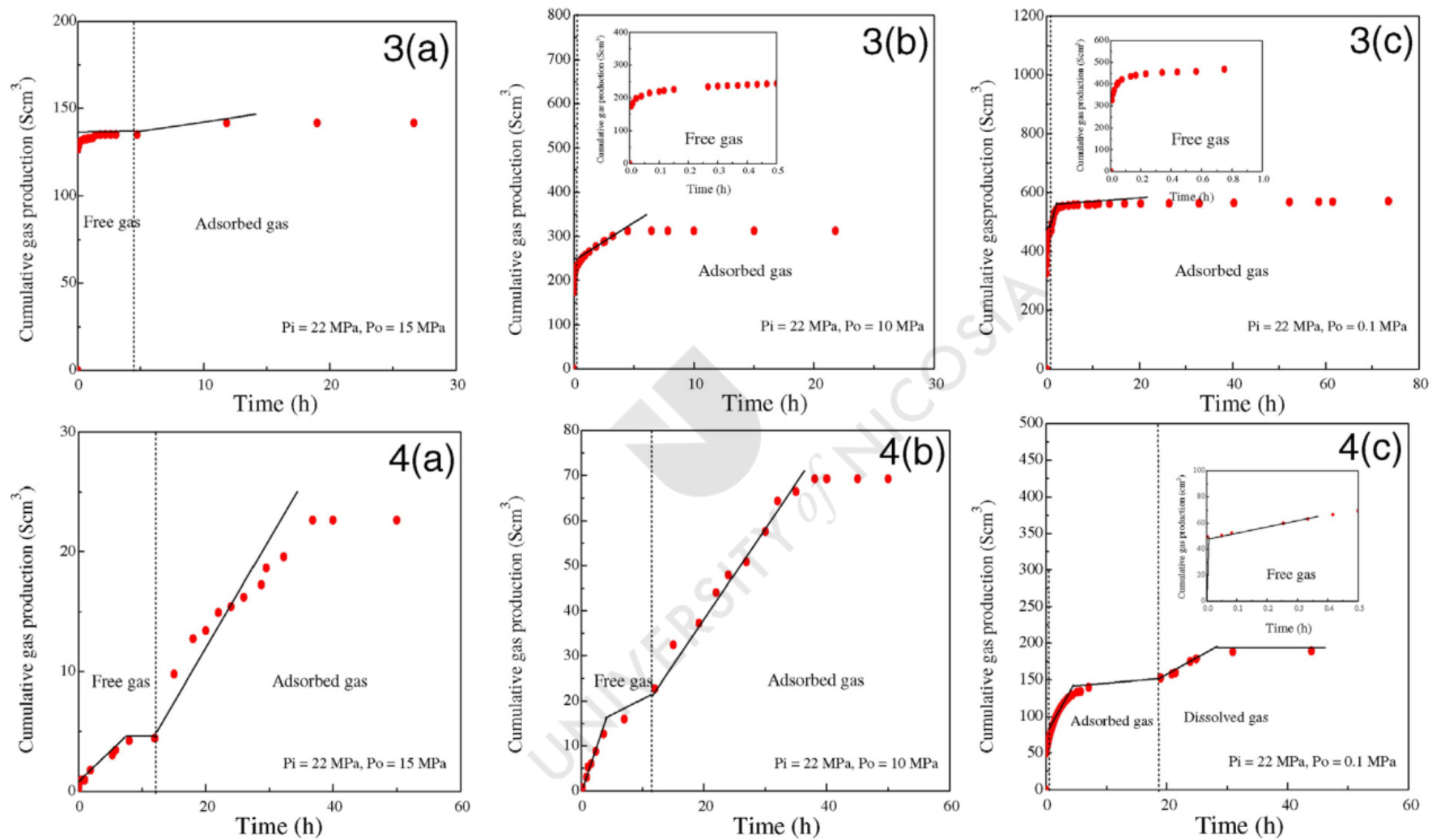
Figure 32. Core investigation data for samples 3 (up) and 4 (down). Initial pressure (P_i) for all samples is 22 MPa. Production pressures (P_0) are: a) 15 MPa, b) 10 MPa, and c) 0.1 MPa. Source: Sang *et al.* (2016).

To alleviate the discrepancies emanating from the different spatial and temporal scales between the model results and the shale core measurements, we have opted to non-dimensionalise all findings. Non-dimensional gas production was achieved by utilising the following expression:

$$Q_n = \int_0^{t_{total}} q_n(t)dt_n \tag{40}$$

where Q_n is the gas non-dimensional cumulative gas production, $q_n(t)$ is the non-dimensional flowrate of the natural gas, t_n is the non-dimensional time and t_{total} is the total time of gas flow (s). Non-dimensional flowrate and non-dimensional time can be calculated from the following relationships (Islam *et al.* 2017):

$$q_n(t) = \frac{141.2q(t)B_g\mu}{kh_{net}(p_i - p_{pr})} \tag{41}$$

$$t_n = \frac{0.00633kt}{\varphi\mu c_t l^2} \tag{42}$$

where $q(t)$ is the volume flowrate (m^3/s), B is the gas formation volume factor, μ is the dynamic viscosity (Pa·s), k is the rock permeability (mD), h_{net} is the net pay (in our case is the diameter of the outlet for the model and the length for the core samples) (m), p_i is the initial pressure (Pa), p_{pr} is the production pressure (Pa), φ is the porosity, c_t is the total compressibility ((Pa)$^{-1}$), and l is the length of the sample or the model size (m).

Substituting equations (41) and (42) into equation (40), we obtain the following expression:

$$Q_n = \int_0^{t_{total}} q_n(t)dt_n = \int_0^{t_{total}} \frac{141.2q(t)B_g\mu}{kh(p_i - p_{pr})} \cdot \frac{0.00633k}{\varphi\mu c_t l^2}dt = \frac{0.893796}{h(p_i - p_{pr})\varphi c_t l^2}\int_0^{t_{total}} B_g q(t)dt \tag{43}$$

The total compressibility of the reservoir rock filled by gas can be expressed by:

$$c_t = (1 - \varphi) \cdot c_m + \varphi \cdot c_g \tag{44}$$

63

where φ is the porosity, c_m is the matrix compressibility ($(Pa)^{-1}$), c_g is the gas compressibility ($(Pa)^{-1}$). Since the matrix compressibility is much smaller than the gas compressibility, it is possible to neglect the matrix's compressibility. Thus, under ideal gas conditions, gas compressibility can be approximated in the context of pressure:

$$c_t = (1-\varphi) \cdot c_m + \varphi \cdot c_g \approx \varphi \cdot c_g \approx \frac{\varphi}{p_i} \tag{45}$$

Next, the formation volume factor is applied to the volume flowrate to convert it under standard conditions, that is, equation (43) can be recast as:

$$Q_n = \frac{0.893796}{h(p_i - p_{pr})\varphi c_t l^2} \int_0^{t_{total}} B_g q(t) \partial t = \frac{0.893796 p_i}{h(p_i - p_{pr})\varphi^2 l^2} \int_0^{t_{total}} B_g q(t) \partial t \tag{46}$$

where Q_{sc} is the cumulative gas production under standard conditions (m^3).

To enable the comparison of the modelling results with core investigation data, the pressure gradient for the model has been equated with the pressure gradients for the core measurements. Again, for comparison purposes, the cumulative gas production of free gas has been used given that the model considers only free gas. The cumulative gas productions and total times of production for the core samples are presented in Table 3 and the cumulative gas production and the total time interval for the model are listed in Table 4. On the basis of these data, the non-dimensional cumulative gas productions (refer to equation (43)) and the times (consult equation (42)) have been calculated. Table 5, for the core samples, and Table 6, for the model, display the non-dimensional flowrate findings for the computational model.

Table 3. Cumulative natural gas production and time for various core samples.

Parameter	Pressure difference, (MPa)	Core 1	Core 2	Core 3	Core 4
Cumulative gas production under standard conditions (cm^3)	7	4	27	141	133
	12	16	58	247	258
	21.9	60	90	410	473
Total time (h)	7	12	6	4	4.8
	12	12	1	2	0.5
	21.9	0.5	1.5	0.35	0.8

Table 4.Cumulative natural gas production and time for the model.

Pressure difference, (Pa)	Cumulative gas production in standard conditions, ($\times 10^{-21}\,\text{m}^3$)	Total time, (μs)
100	1.62	3.55
200	3.24	3.75
400	6.48	4
800	12.96	4.2
1600	25.9	1.5
3200	51.8	1

Table 5. Non-dimensional cumulative natural gas production for core samples.

Parameter	Pressure difference, (MPa)	Core 1	Core 2	Core 3	Core 4
Non-dimensional cumulative gas production	7	1064	2773	1558	1856
	12	2482	3475	1573	1896
	21.9	5101	2955	1575	1948

Table 6. Non-dimensional cumulative natural gas production for the model.

Pressure difference, (Pa)	Non-dimensional cumulative gas production, Q_n
100	1621
200	1621
400	1623
800	1626
1600	1631
3200	1643
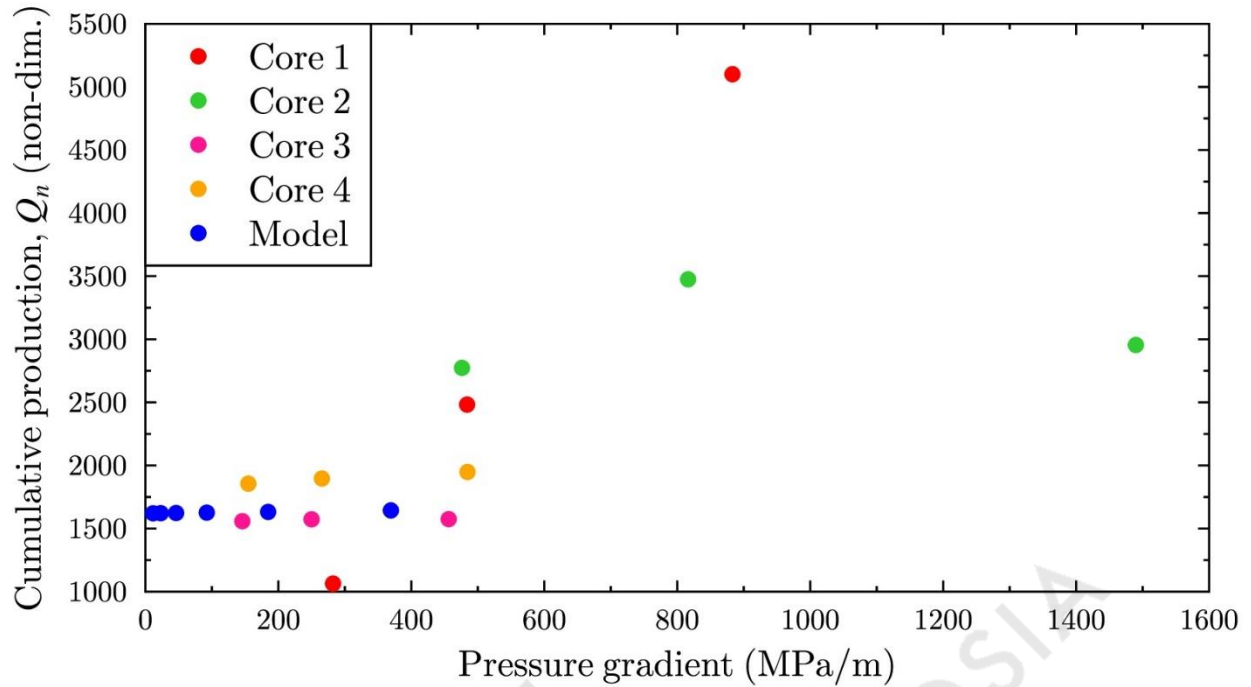
Figure 33. Non-dimensional cumulative natural gas production–pressure gradient validation plot for the model and the core samples.

Figure 33 presents the non-dimensional cumulative gas production and pressure gradient relationships for core measurements and the numerical model. As it can be observed in Figure 33, the non-dimensional cumulative gas production obtained from the computational model (shaded in blue) is almost the same and can be represented by horizontal trend. Although the non-dimensional cumulative gas production for the core samples varies slightly with pressure, it can be said that the non-dimensional gas production and pressure gradient relationships exhibit a horizontal pattern for core samples 2 to 4. Some deviations arise from the extended duration required for whole gas volume to produce and not for the ideal investigation conditions. The exception is provided by sample 1 which is characterised by an extremely low porosity (2%). For the sample 1, the non-dimensional cumulative gas productions changes significantly as a function of the pressure. This behaviour emanates from the dramatically slow gas flow velocity in sample 1. Therefore, so more time is required for the gas flow to reach equilibrium under small pressure gradients.

The best agreement is observed between the non-dimensional modelling results and cumulative gas production data of core sample 3 from the gas production test. To investigate this correlation more thoroughly, the same pressure gradients as for the core gas production test have been applied to the model (see Figure 34). In addition, in the non-dimensionalisation approach, we considered the real gas behaviour and calculated the total compressibility used in equation (43) employing the following formula:

$$c_t \approx \varphi \cdot c_g = \varphi \cdot \left(\frac{1}{p} - \frac{1}{Z} \frac{\partial Z}{\partial p} \right). \tag{47}$$

For real gas conditions, equation (43) can be rearranged as:

$$Q_n = \frac{0.893796}{h(p_i - p_{pr})\varphi c_t l^2} \int_0^{t_{total}} B_g q(t) \partial t = \frac{0.893796}{h(p_i - p_{pr})\varphi^2 \left(\frac{1}{p_i} - \frac{1}{Z} \frac{\partial Z}{\partial p} \right) l^2} \int_0^{t_{total}} B_g q(t) \partial t \cdot \tag{48}$$

Here the Z-factor was calculated for the pressure ranges pertinent to the model with the aid of equation (21). Figure 34 demonstrates the non-dimensional cumulative gas production values for the model and for core sample 3.
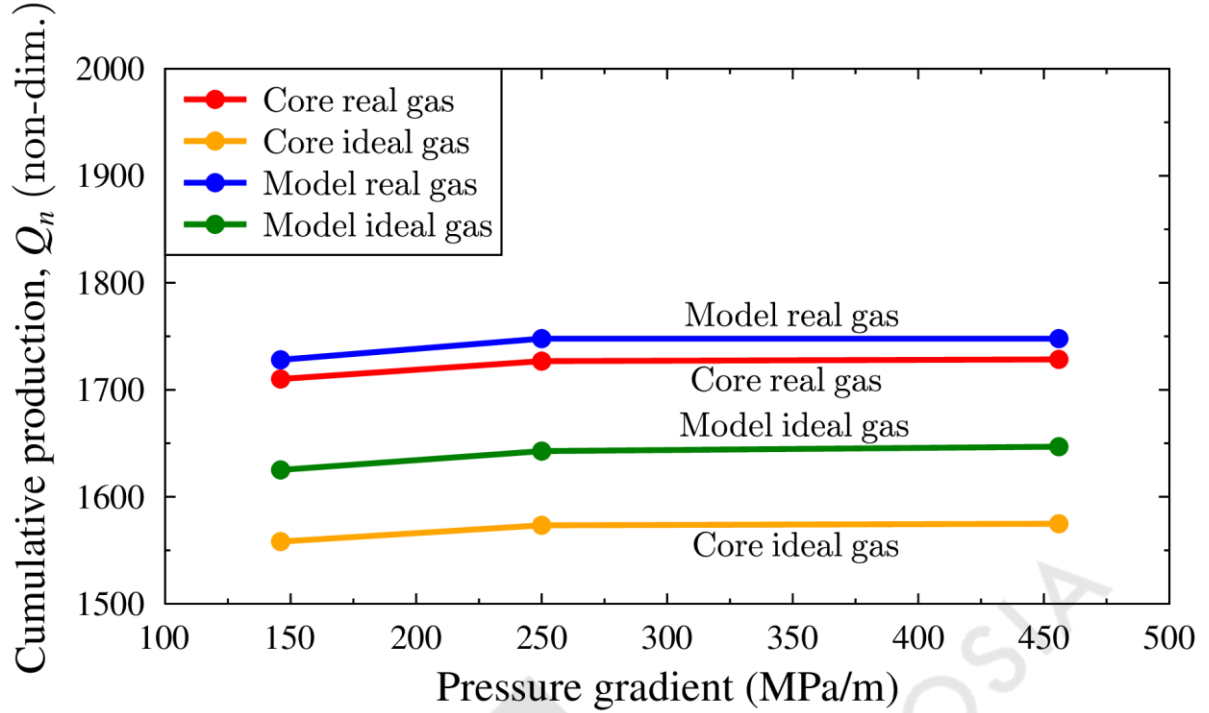
Figure 34. Comparison of the non-dimensional cumulative natural gas production findings for the core sample 3 and the computational model. Non-dimensional modelling results and experimental findings were obtained from two different approaches that considered the ideal and the real compressibility, respectively.

As observed from Figure 34, incorporating the real gas compressibility in the non-dimesionalisation formula helps match the accuracy of the computational simulation results with the actual core measurements. Whatsmore, if the real gas behaviour is omitted this leads to an underestimation of gas production. To further examine the actual behaviour of the gas, we formulated two additional cases with different gas compositions. In the first scenario the model with porous media was filled with a mixture of gases, that is, 70% methane and 30% ethane. In the second case, the model's porous domain was assumed to be replete with ethane.

The model scenario whose porous media featured methane was used as the basis of comparing the different cases. A summary of the cumulative gas production for the models, filled by gases with different composition, is presented in Table 7. In addition, the non-dimensional cumulative gas production for the modelling scenarios is listed in Table 8.

Comparing model results it becomes apparent that the heavier the molecular weight of the gas, the larger is the cumulative gas production, as illustrated in Figure 35. Concluding, it is essential to investigate thoroughly not only for the reservoir geometry and behaviour but also the reservoir fluid properties.
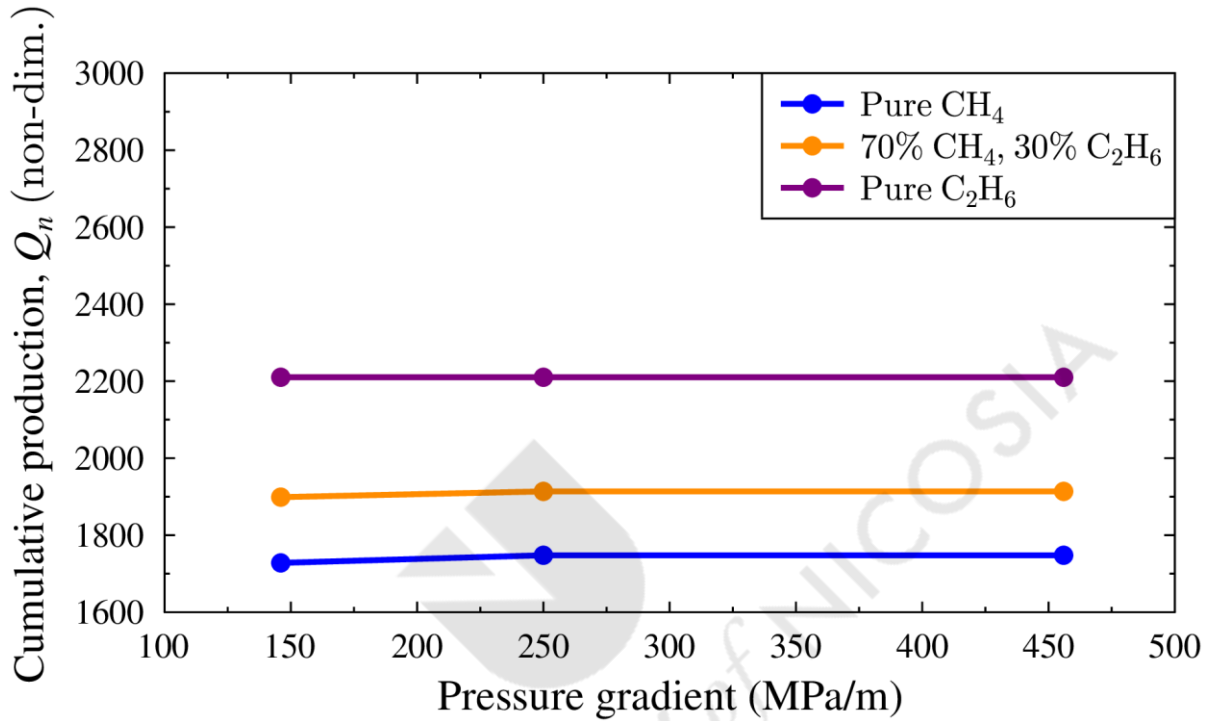
Figure 35. Non-dimensional cumulative gas production comparison for the model runs exhibiting natural gases with different composition. As it can be seen from the plot, the heavier the molecular weight of the gas, the larger the cumulative gas production is.

Table 7. Cumulative production for the modelling cases with natural gases of different chemical compositions under standard conditions.

Parameter	Pressure difference (Pa)	Model methane ($\times10^{-20}$)	Model 70% methane, 30% ethane ($\times10^{-20}$)	Model ethane ($\times10^{-20}$)
Cumulative gas production under standard conditions (m^3)	1,264	2.42	2.23	0.854
	2,167	4.14	3.29	1.46
	3,954	7.57	6.03	2.67

Table 8. Non-dimensional cumulative production for the modelling scenarios with natural gases of different chemical compositions.

Parameter	Pressure difference (Pa)	Model pure methane	Model 70% methane, 30% ethane	Model pure ethane
Non-dimensional cumulative gas production	1,264	1,728	1,899	2,210
	2,167	1,748	1,913	2,210
	3,954	1,748	1,913	2,210

4.3. Steady-state pressure and velocity results

After validating the cumulative gas production results, the flowrates for the computational model and the shale core samples under steady state flow conditions have been compared. Facilitating the comparison between the modelling results and the experimental findings, gas flowrate data from four reservoir core samples (A-1, A-2, A-3, A-4) from the Sichuan gas field, in China, have been employed (see Figure 36). Rock cores possess a diameter of 2.5 cm while their length measures 5 cm long. Experimentally, each core was tested in the core holder under a range of confining pressures. Gas was injected

into the cores at different dosage rates until pressure has stabilised to a steady-state. Subsequently, the output gas volume rate was measured under steady-state conditions (for more detailed description of the experimental procedure, please consult Song *et al.* (2015)). Figure 36 shows the relationship between the measured flowrate and the pressure drawdown.
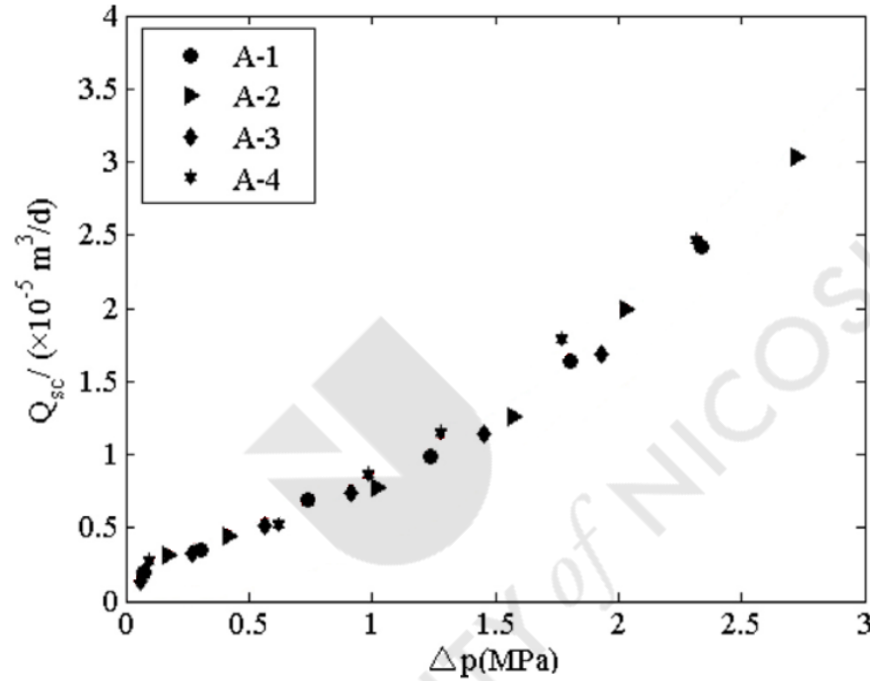
Figure 36. Gas flowrate and pressure relationship for core samples (A-1, A-2, A-3, A-4) from Sichuan gas field under steady-state conditions. Modified from Song *et al.* (2015).

To compare experimental core findings and simulation results, we reproduced the same flow conditions at the micro-level for different pressure gradients in the same pressure range used for the core investigation. That is, we imposed wall boundary conditions for the entire model except for the inlet and the outlet vertices so as to emulate gas flow through a core sample. The pertinent dimensions of the model and the velocity magnitude used for flowrate calculations are depicted in Figure 37. Core measurements and modelling results for the various pressure gradients are listed in Table 9

.
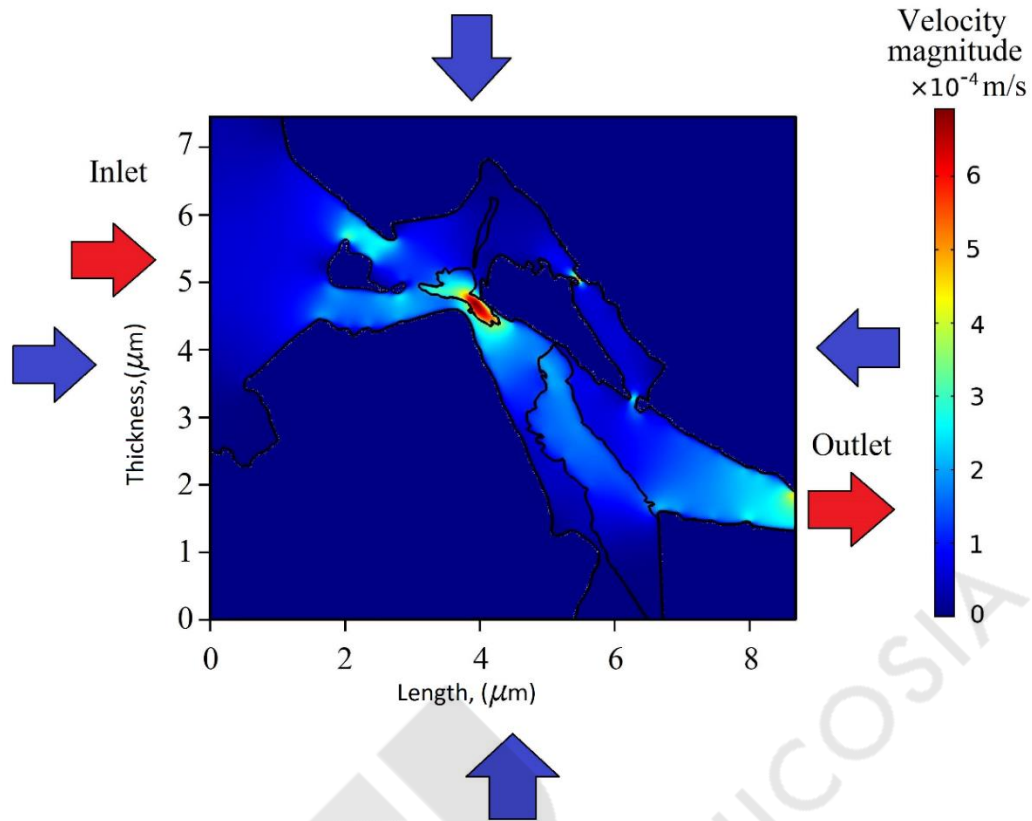
Figure 37. Computed natural gas flowrate for a pressure gradient of 20 MPa/m. Blue arrows depict confining pressure, while red arrows denote flow directions in and out of the shale domain.

Table 9. Natural gas flowrate under steady-state conditions.

Pressure gradient	Flowrate under standard conditions	
(MPa/m)	Core samples ($\times 10^{-11}$ scm/s)	Model ($\times 10^{-15}$ scm/s)
5	5.7	2.61
10	6.03	5.22
20	9.26	10.4
30	15	15.8
40	22.9	20.9
50	32.6	26.3
60	43.9	31.3

Since the shale cores and the model have several orders of magnitude difference in spatial and temporal scales, non-dimensionalisation was used to compare experimental findings and modelling results. Hereafter, equation (41) has been used to determine the non-dimensional flowrates for core investigation data and the modelling results. Calculated non-dimensional flowrates are presented in Figure 38.
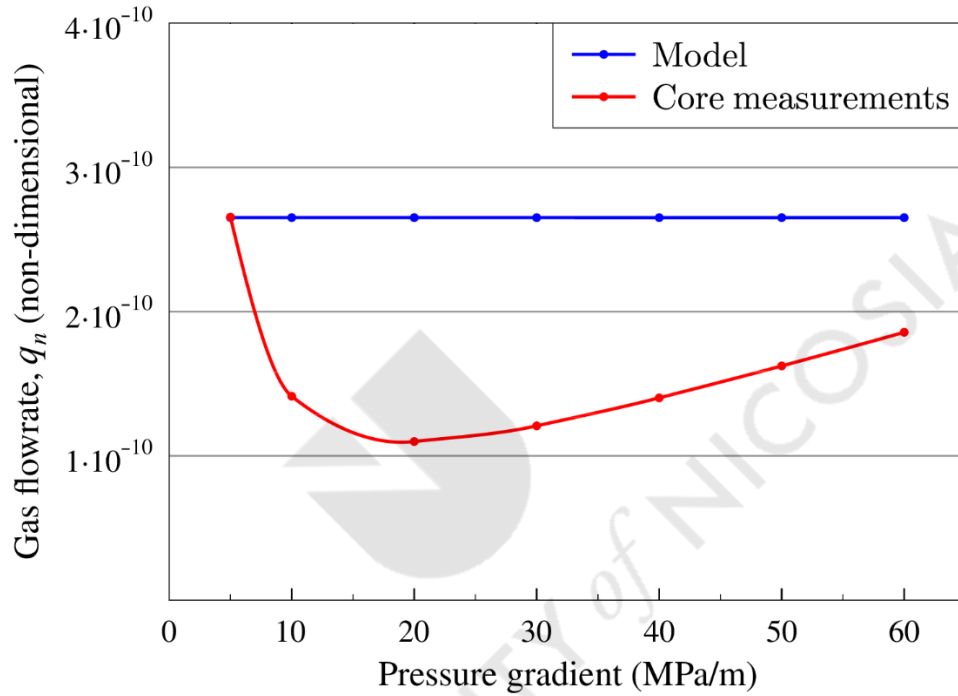
Figure 38. Non-dimensional natural gas flowrates under steady-state conditions for the computational model and the core measurements. Notably, the discrepancy between the simulated and experimental results, after it originally diverges, shrinks with the rising pressure gradient.

As it can be observed from Figure 38, the non-dimensionalisation method does not produce a sound basis for comparison of the gas flowrates for the microscopic model and the core measurements, since gas properties vary significantly with pressure. To address the variabilities in gas properties the concept of pseudo-pressure (p_p) was applied based on Al-Hussainy $et\ al.$'s (1966) formulation:

$$p_p = 2 \int_0^P \frac{P dP}{\mu(P) Z(P)} \qquad (49)$$

The pseudo-pressure (Al-Hussainy, Ramey Jr and Crawford 1966) obtained from equation (49) was introduced in equation (41) to compute the non-dimensional flowrate. Both the non-dimensional modelling results and the core findings are displayed in Figure *39*.
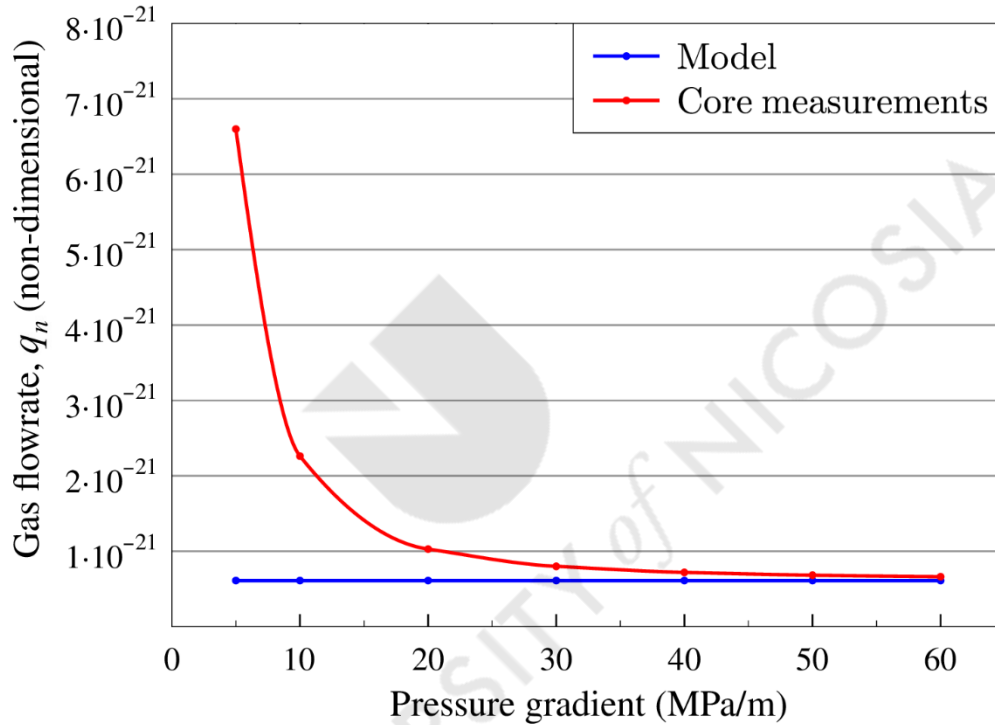
Figure 39. Non-dimensional gas flowrate of the core measurements and the computational model as a function of the pseudo-pressure gradient. Here, the discrepancy between the non-dimensional modelling results and the core measurements can be explained by the dependence of the permeability on pressure.

As it can be noticed from Figure 39, when the pressure gradient is high (>30 MPa) the non-dimensional gas flowrates of the model and the core measurements exhibit very good agreement. However, at low pressure gradients (<20 MPa) the model and the experimental gas flowrate diverge substantially. This behaviour can be explained by

dependence of the permeability on pressure. Detailed description of the physical mechanism and formulae need to be applied in the non-dimensionalisation approach are given in §2.5.3 "Klinkenberg permeability", page 22. Taking into account Klinkenberg permeability and pseudo-pressure, the non-dimensionalisation formula can be recast as:

$$q_n(t) = \frac{141.2 q(t) B_g \mu(p)}{k_\infty \left[1 + \left(\dfrac{b}{p_m} \right)^2 \left(\dfrac{L_{Ke}}{\lambda} \right) \right] h \cdot 2 \displaystyle\int_{p_{pr}}^{p_i} \dfrac{p}{\mu(p) Z(p)} dp} \tag{50}$$

where b can be calculated from equation (13). Non-dimensional theoretical gas flowrate results exhibit excellent match with experimental measurements, as demonstrated in Figure 40 (Kovalchuk and Hadjistassou 2020).
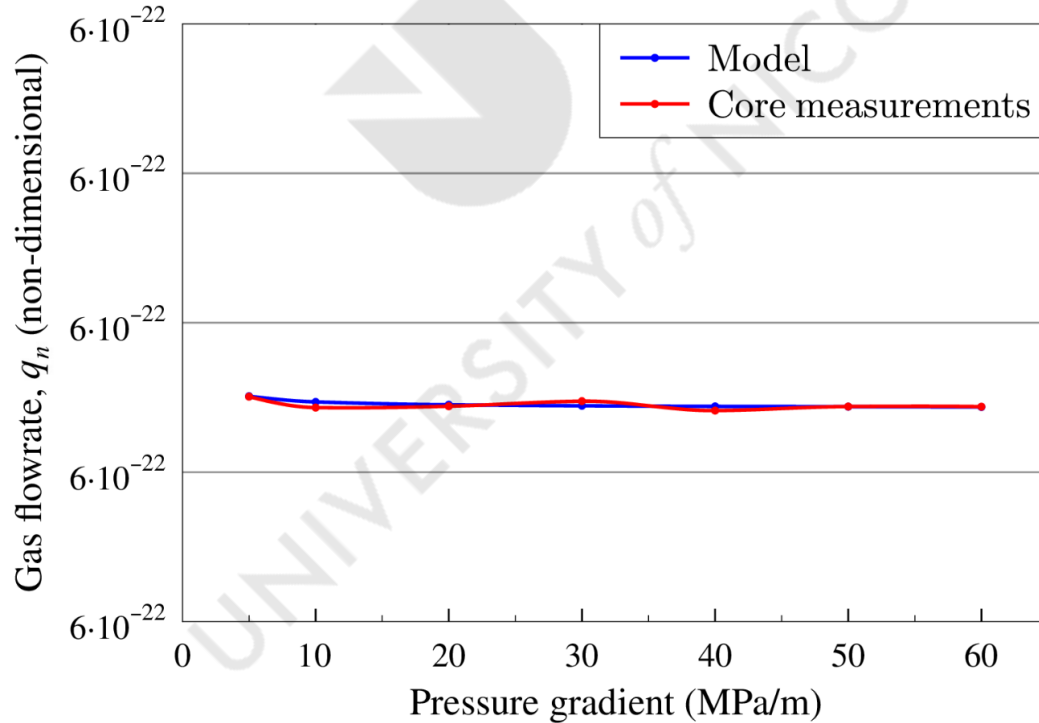
Figure 40. Non-dimensional computed flowrate results and core measurements considering pseudo-pressure and improved Klinkenberg permeability. Non-dimensional modelling results exhibit sound agreement with experimental findings.

4.4.   Adsorption modelling results

As it was stated before, natural gas in shales is contained not only as free gas in the pore structure and fractures, but also in liquid form, including adsorbed gas on the pore surfaces (Li *et al.* 2018; Yang *et al.* 2016; Yuan *et al.* 2014). The nanosize of the pores in shales results in a considerable inner surface area, and hence adsorption and desorption processes become important (Etminan *et al.* 2014). Therefore, accurate estimation of the amount of free and adsorbed gas and the precise analysis of the transient flow behaviour in shale gas formations are crucial for predicting production performance, devising or adjusting the production strategy, and fracture design in shale gas reservoirs (Li *et al.* 2018; Yang *et al.* 2016; Yu, Sepehrnoori and Patzek 2014; Yuan *et al.* 2014; Zhang *et al.* 2017). The usual method for describing the methane adsorption capacity is with the aid of adsorption isotherm (Li, Min*, et al.* 2016; Zou and Rezaee 2019). In the past, a wide variety of isotherm models has been proposed. In this section, the types of isotherm employed to match the core measurements data are presented and analysed. Then, modelling results including non-dimensional cumulative gas production with incorporated adsorption are considered and discussed.

4.4.1. Adsorption isotherm types

4.4.1.1.   The Langmuir isotherm

The Langmuir adsorption isotherm, originally developed to describe gas-solid-phase adsorption on activated carbon, nowadays is one of the most widely used. Its empirical model describes the equilibrium between the adsorbent (a generally solid material that adsorbs another substance) and the adsorbate (a substance which is adsorbed) systems and assumes a monolayer adsorption, that is, the layer of the adsorbed gas is one molecule thick (Foo and Hameed 2010; Liu *et al.* 2019). Consequently, only a finite number of gas molecules can be adsorbed, while sites for adsorption are taken as identical and equivalent and there is no lateral interaction between adjacent adsorbed molecules (Liu *et al.* 2019). In other words, the Langmuir isotherm describes homogeneous adsorption

during which all sites possess equal attraction for the adsorbate. Moreover, the Langmuir's model has postulated a fast decrease of the intermolecular attractive forces with increasing distance from the pore wall (Foo and Hameed 2010).

The original Langmuir equation is expressed by:

$$V_{ads} = V_L \cdot \frac{P}{P + P_L},$$

(51)

where V_{ads} is the adsorbed gas volume (cm^3/g), V_L is the Langmuir maximum sorption capacity (cm^3/g), P is the pressure (MPa), P_L is the Langmuir pressure (MPa) (Chen *et al.* 2017). Also, the Langmuir model can be described through the fractional surface coverage θ or through gas volumes.

4.4.1.2.   The Brunauer-Emmet-Teller (BET) isotherm

The Brunauer-Emmet-Teller (BET) isotherm was developed in 1938 by S. Brunauer, P.H. Emmet and E. Teller (Fianu, Gholinezhad and Sayed 2019). To derive this isotherm, the main assumption was that the number of adsorption layers on the surface of the organic carbon was infinite. The BET equation is given by:

$$V(P) = \frac{V_m C \frac{P}{P_0} \left[1 - (n+1)\left(\frac{P}{P_0}\right)^n + n\left(\frac{P}{P_0}\right)^{n+1} \right]}{1 - \frac{P}{P_0} \left[1 + (C-1)\frac{P}{P_0} + C\left(\frac{P}{P_0}\right)^{n+1} \right]},$$

(52)

where V_m is the maximum adsorption gas volume when the entire absorbent surface is being covered with a complete gas monolayer (cm^3/g), C is a constant related to the net heat of adsorption, P_0 the saturation pressure of the gas (Pa), which can be calculated from the reduced Kirchoff equation (see equation (54)) and n is the maximum number of adsorption layers, i.e., the adsorbed gas is one molecule thick. The adsorbent surface refers to the entire pore network available for gas adsorption. When $n = 1$, the equation will be reduced to the Langmuir isotherm and when $n = \infty$, the equation can be recast as

78

$$V(P) = \frac{V_m C \cdot P}{P_0 - \left\{ P\left[1 + \frac{(C-1)P}{P_0} \right] \right\}} \quad . \tag{53}$$

The reduced Kirchoff equation for calculating the saturation pressure is of the following form:

$$P_0 = P_c \cdot \exp\left(\frac{T_{nbp}}{T_c} \left[\frac{\ln P_c}{1 - \left(T_{nbp} / T_c \right)} \right] \left[1 - \frac{T_c}{T} \right] \right) , \tag{54}$$

where P_c is the critical pressure (Pa), T_{nbp} is the temperature at normal boiling point (K), and T_c is the critical temperature (K).

4.4.1.3. The Klotz isotherm

The concept of Klotz was originally and successfully applied to protein interactions with small molecules (Buttersack 2019). Its application to capillary condensation has to consider that all equilibrium constants involved could be merged into a single one when surface effects with the pore walls can be neglected. Such surface interaction can be induced by primary adsorption sites interacting with the fluid inside the pore, which is either in the gaseous, or, after condensation, in liquid state. The Klotz equation is given by:

$$V(P) = \frac{V_m C \cdot K \dfrac{P}{P_0} \left[1 - (n+1)\left(K\dfrac{P}{P_0} \right)^n + n\left(K\dfrac{P}{P_0} \right)^{n+1} \right]}{\left(1 - K\dfrac{P}{P_0} \right) \left[1 + (C-1)K\dfrac{P}{P_0} + C\left(K\dfrac{P}{P_0} \right)^{n+1} \right]} \tag{55}$$

where V_m is the maximum adsorption gas volume when the entire absorbent surface is being covered with a complete monolayer (cm^3/g), C is a constant related to the net heat of adsorption, P_0 the saturation pressure of the gas (Pa), which can be calculated from the reduced Kirchoff equation (please refer to equation (54)), n is the maximum number of adsorption layers, and K is the binding constant of already adsorbed molecules (Buttersack 2019).

The Klotz isotherm is an S-shape isotherm which may be caused by solute-solute attractive forces at the surface which result in cooperative adsorption (positive cooperativity). Non-polar hydrophobic methane molecules have low affinity with clays and adsorb onto the surface of shale pores via Van der Waals attractions (Inglezakis, Poulopoulos and Kazemian 2018; Limousin *et al.* 2007). However, as soon as a clay surface is covered by these compounds, other organic molecules are adsorbed more easily which can result in a multi-layer adsorption at high pressures (Inglezakis, Poulopoulos and Kazemian 2018; Nakagaki, Handa and Shimabayashi 1973).

4.4.2. Adsorption modelling

For adsorption modelling it is important to match the isotherm profile and to estimate the isotherm parameters in such a way so as to fit the experimental data. The simplest and the most widely used isotherm model is the Langmuir isotherm. However, for the gas production test measurements (Sang *et al.* 2016) utilised in this research for the validation of simulation results, the Langmuir isotherm can be suitable to match only for narrow pressure range, for instance, for low pressure values or for high pressure values. As it was noted by Sang (Sang *et al.* 2016), this can happen since the adsorption isotherm measured during this gas production test is up to 22 MPa, whereas in the majority of the literature, isotherms were measured at a methane equilibrium pressure of up to only 15 MPa. Figure 41 presents the Langmuir isotherms fitted for high pressure and for low pressure domains. Parameters employed to calculate the Langmuir isotherms are listed in Table 10.
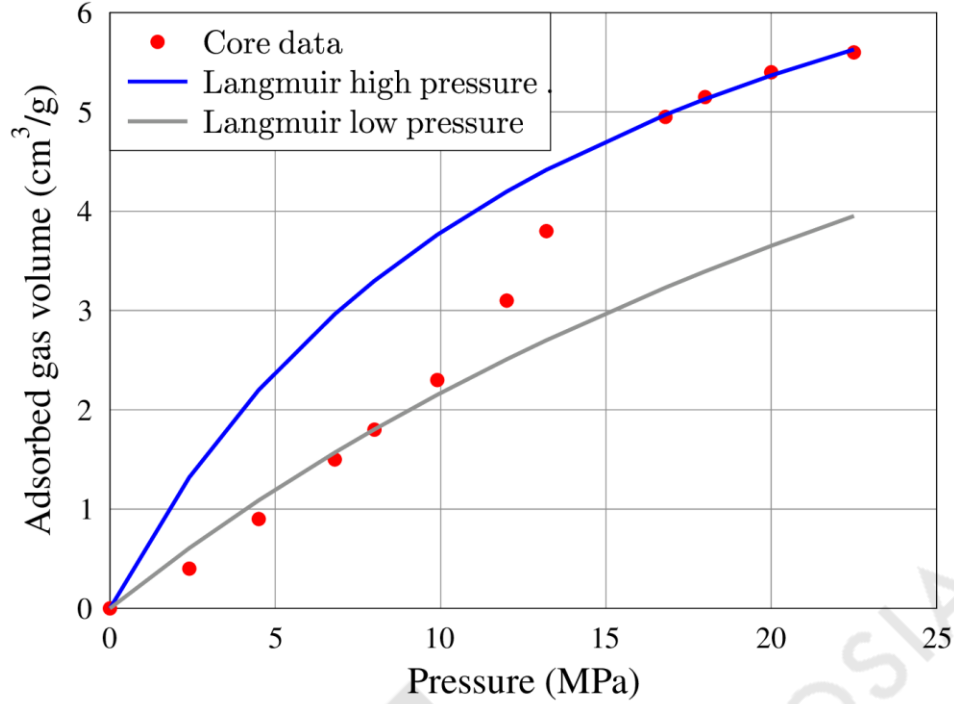
Figure 41. Langmuir isotherms can be fitted with the gas production test measurements only for a narrow pressure range, for example, for high pressure region and for low pressure regime.

Table 10. Langmuir isotherms parameters used to fit high pressure and low pressure regions.

Parameters	Langmuir isotherm high pressure fitted	Langmuir isotherm low pressure fitted
P_L, MPa	14.36	43.2
V_L, cm^3/g	9.22	11.54

As observed Figure 41, the isotherm shape for core measurements can be described more accurately by a sigmoidal isotherm profile. This behaviour can be indicative of forming multiple adsorbed layers during an increase in pressure. As a result, the Langmuir isotherm which was developed to describe monolayer adsorption is not recommended for comparing data within widely differing pressure ranges. To capture the sigmoidal behaviour of the isotherm from the core findings, the BET and the Klotz isotherm models were chosen (for detailed description please refer to §4.4.1.2 "Brunauer-Emmet-Teller

81

(BET) isotherm", page 78 and §4.4.1.3 "Klotz isotherm", page 79). These models are generally suitable for multilayer adsorption simulations.

Figure 42 displays three different isotherms which were compared with the core measurements. The parameters which are used to calculate the isotherms and the root mean square errors between them and the core measurements are listed in Table 11. It should be noted that, the parameters for the Langmuir isotherm have been estimated to match the high pressure isotherm area since the simulation model was constructed for reservoir conditions.
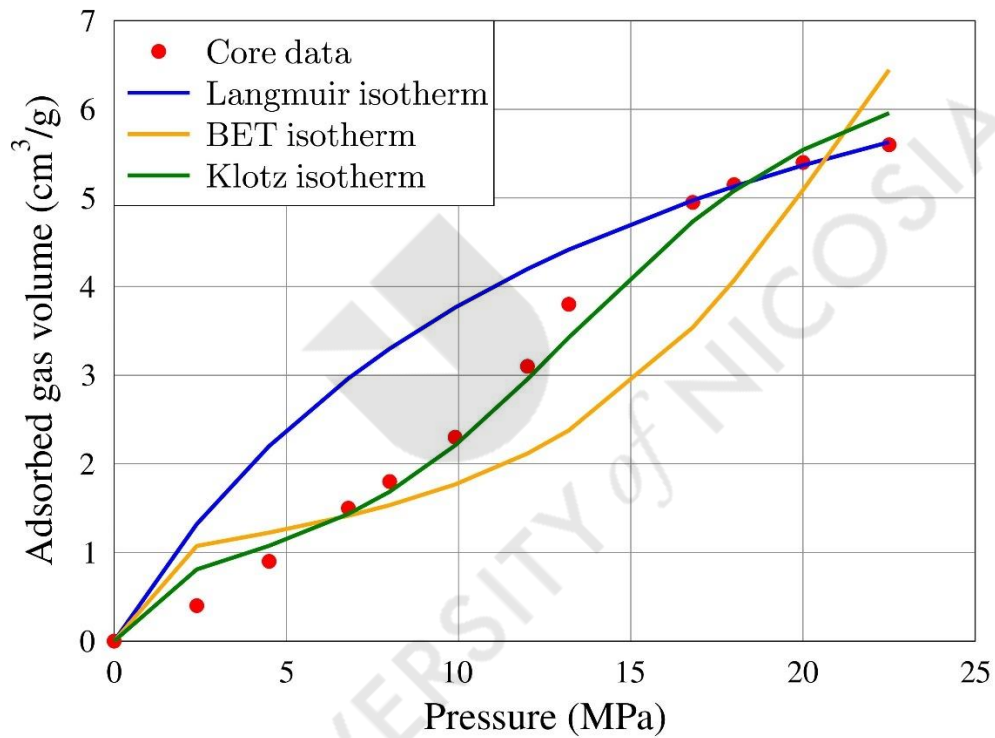
Figure 42. Adsorbed gas volume data from the core sample and calculated isotherms.

Although the BET isotherm has a smaller root mean square error than the Langmuir isotherm, the isotherm shape is completely different from the experimental data. Hence, the adsorption mechanism is not captured accurately and, thus, employing the BET isotherm does not generate accurate simulation results. The Klotz isotherm fits the core measurements reasonably well and is characterised by the least quadratic mean error. Moreover, the difference between the calculated isotherm and the experimental data does

82

not vary considerably for different pressure values. Consequently, the Klotz isotherm can be applied for a wide range of pressures.

Table 11. Parameters utilised for the calculation of the isotherms and the normalised errors between the computed and experimental data.

Isotherm models	Parameters	Normalised Root Mean Square Error (*NRMSE*)
Langmuir	P_L = 14.36 MPA V_L = 9.22 cm^3/g	0.307
BET	V_m = 1.1 cm^3/g C = 25 N = 9	0.108
Klotz	V_m = 0.82 cm^3/g C = 25 N = 9 K = 1.9	0.048

The normalised Root Mean Square Error (*NRMSE*) in this study is defined as:

$$NRMSE = \frac{1}{N} \cdot \frac{\sum_{i=1}^{N}\left(V_{calc} - V_{core}\right)^2}{V_{calc} \cdot V_{core}} \tag{56}$$

where V_{core} is the adsorbed gas volume from the core measurements (cm^3/g), V_{calc} is the adsorbed gas volume (cm^3/g) which is computed from the chosen isotherm model (Langmuir, BET or Klotz), and N is the number of observations.

Figure 43 displays the cumulative gas production for the model with free gas and free and adsorbed gas for the initial pressure of 1,264 Pa. As it can be observed from Figure 43, ignoring the adsorption and desorption processes leads to a dramatic underestimation of gas production.
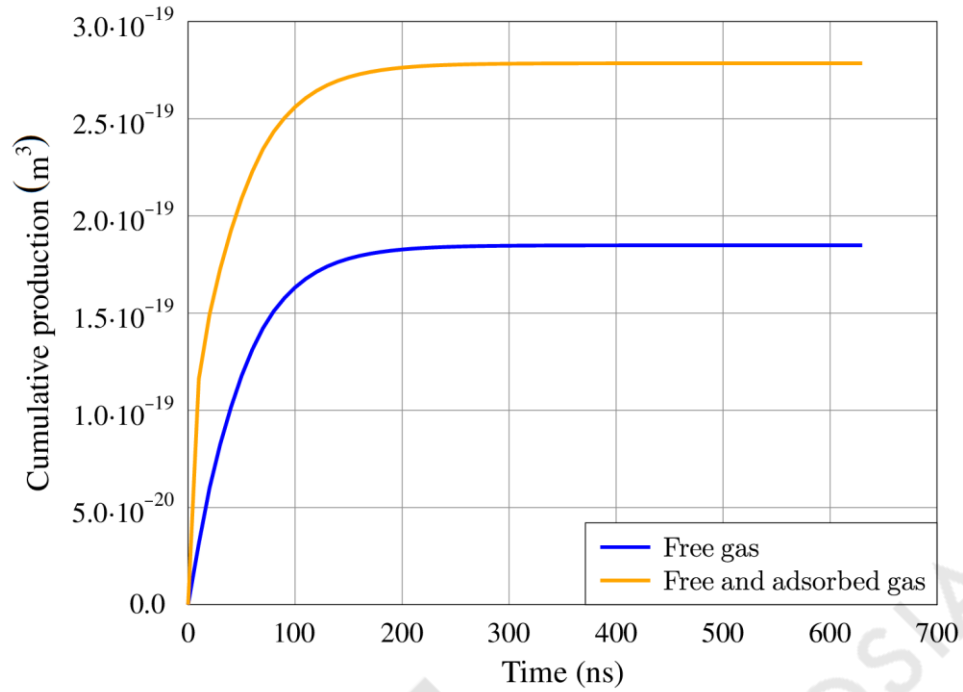
Figure 43. Cumulative production of the model with porous media filled by methane. Initial pressure 1,264 Pa.

Microscale cumulative production data for adsorbed gas was compared with gas production test measurements (Sang *et al.* 2016) using the non-dimensionalisation procedure. The non-dimensional flow rate was obtained from equation (48). The gas production test data for the core sample are presented in Table 12. Cumulative gas production findings for the models with different isotherms are listed in Table 13. On the basis of these data, the non-dimensional cumulative gas production values have been derived and are detailed in Table 14 and Table 15, respectively.

Table 12. Cumulative gas production for the core sample at various pressure differences.

Pressure difference, (MPa)	Cumulative gas production under standard conditions (free gas), (scm)	Cumulative gas production under standard conditions (free and adsorbed gas), (scm)
7	145	210
12	251	353
21.9	458	661

Table 13. Cumulative gas production for the models with free and adsorbed gas simulated with different isotherm models.

Cumulative gas production under standard conditions	Pressure difference, (Pa)		
	1,264	2,167	3,954
Free gas, ($\times 10^{-19}$ scm)	1.849	3.172	5.792
Free and adsorbed gas, Langmuir, ($\times 10^{-19}$ scm)	2.773	4.756	8.683
Free and adsorbed gas, BET, ($\times 10^{-19}$ scm)	5.04	8.642	15.775
Free and adsorbed gas, Klotz, ($\times 10^{-19}$ scm)	2.815	4.827	8.813

Table 14. Non-dimensional cumulative gas production for the core sample under standard conditions.

Pressure difference, (MPa)	Non-dimensional cumulative gas production (free gas)	Non-dimensional cumulative gas production (free and adsorbed gas)
7	1,710	2,477
12	1,727	2429
21.9	1,728	2,492

Table 15. Non-dimensional cumulative gas production for the models with free and adsorbed gas featuring with different isotherm models.

Non-dimensional cumulative gas production under standard conditions	Pressure difference, (Pa)		
	1,264	2,167	3,954
Free gas, ($\times 10^{-19}$ scm)	1,728	1,748	1,748
Free and adsorbed gas, Langmuir, ($\times 10^{-19}$ scm)	2,428	2,429	2,430
Free and adsorbed gas, BET, ($\times 10^{-19}$ scm)	4,412	4,414	4,415
Free and adsorbed gas, Klotz, ($\times 10^{-19}$ scm)	2,464	2,465	2,467

Figure 44 displays the comparison of the non-dimensional cumulative gas production values from the models, with the different isotherms, and the core measurements. Since data from the model with the applied BET isotherm are inconsistent with the core findings (please refer to Table 14 and Table 15), these data were excluded from Figure 44. As it can be observed from Figure 44, both isotherm models show good coincidence with actual data. However, the model making use of the Klotz isotherm exhibits better agreement with rock measurements. Whatsmore, it should be noted that the microscale model simulation is performed in reservoir conditions, i.e., for high pressures where the core data and the calculated Langmuir isotherm are the most fitted (please refer to Figure 42).

On Figure 45 the non-dimensional cumulative gas production data for the model and the core sample are presented for the free gas case and for the free and adsorbed gas scenario whereas the adsorbed gas cumulative production was obtained by employing the Klotz isotherm. Figure 45 demonstrates excellent agreement between non-dimensional actual data and simulation results for the models with free and adsorbed gas.
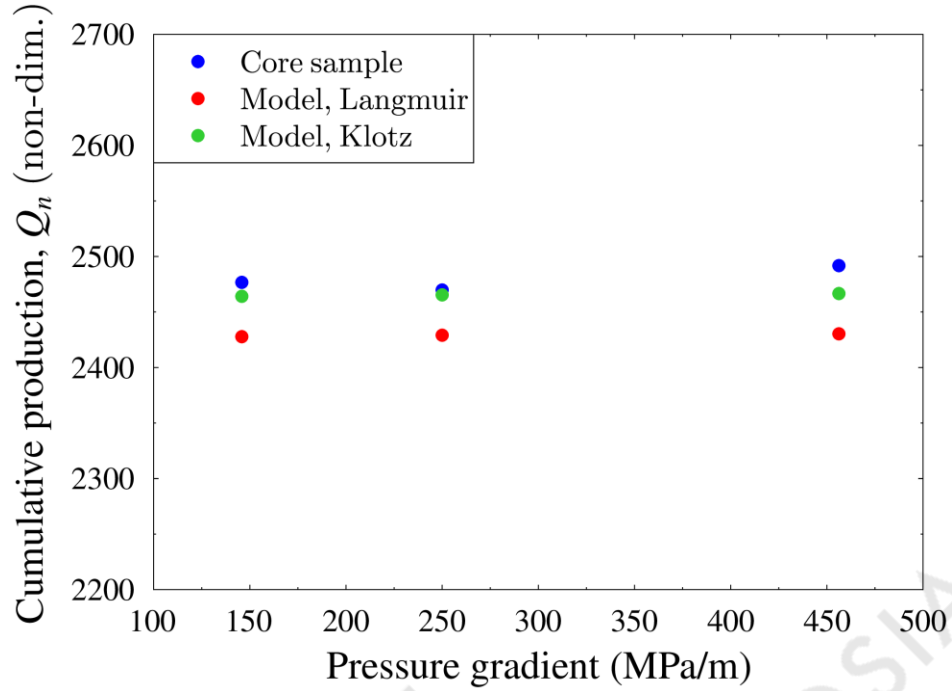
Figure 44. Comparison of core and model non-dimensional cumulative gas production findings for different isotherm models. The model with the Klotz isotherm exhibits better agreement with rock measurements.
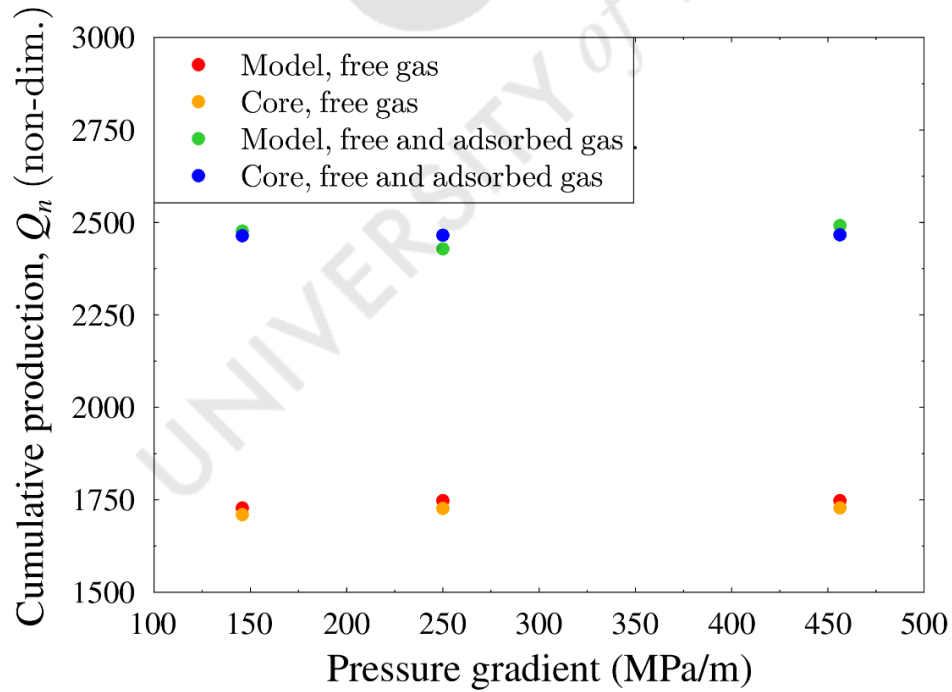
Figure 45. Comparison of core and model non-dimensional cumulative gas production findings for free and adsorbed gas deduced from using the Klotz isotherm.

4.5. Sensitivity analysis

During reservoir exploration, it is natural to encounter uncertainties in rock parameters, therefore, it is important to pin down the reservoir properties which influence the production rate the most. Once a computational model has been constructed, a sensitivity analysis of the reservoir parameters can be performed. Worth emphasising that fluid and reservoir properties are interrelated. For example, not only does reservoir pressure influence the gas mass density, it also affects gas compressibility and viscosity. Hence, the gas flow dependency on the pressure gradient which, in turn, varies with reservoir pressure. Therefore, accurately simulating reservoir conditions, by considering all of the pertinent relationships, helps investigate the influence gas and reservoir parameters exert on flowrate, otherwise often difficult to obtain from analytical solutions or laboratory measurements.

The sensitivity analysis of the gas flowrate was conducted in the context of permeability, temperature, reservoir pressure, and gas composition. Gas density, compressibility and viscosity have been incorporated in the model as functions of the parameters. To assess the influence a distinct parameter exerts on the gas flowrate, that parameter was varied while the rest of the properties were kept fixed. Computed gas flow velocity results were compared with those from the baseline model.

To consider the influence of variations in gas composition, we have incorporated into the model natural gases with different molecular weights. The gas flow properties, including mass density, viscosity, and compressibility, have been calculated as functions of the molecular weight, pressure, and temperature. With regards to the gas composition, the gas molecular weight ranged from pure methane ($MW = 16.04$) to typical upper limits for natural gas ($MW = 23$). The results of the sensitivity analysis are presented in Figure 46. Model parameters and obtained flow velocity results were normalised to the base case values.
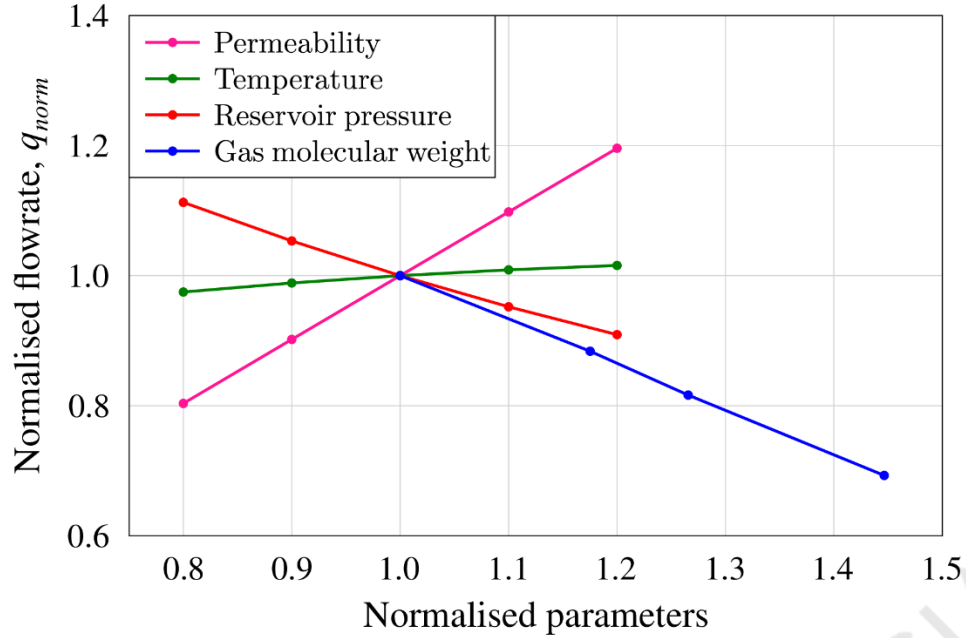
Figure 46. Sensitivity plot of gas flowrate for permeability, temperature, reservoir pressure and molecular weight. Modified parameter values are normalised on the baseline parameter values. Obtained flowrates are normalised on the base case flowrate. All four parameters overlap at point (1.0, 1.0) simply because it denotes their base values. Baseline values are described in §3.5 "Model description", page 46.

As it can be observed from Figure 46, the most important parameter which influences gas flowrate in shales is rock permeability. Therefore, precise permeability values are crucial for gas production forecasts and economic planning. However, shale permeability is still the most challenging and expensive parameter to obtain. Evidently, the development of methods to improve accuracy, reduce time and expense for shale permeability measurements is a promising research line of investigation. Besides the average formation permeability values, the permeability distribution plays a significant role. The model developed here consists of quartz which is non-permeable and makes-up 65% of the model volume. Shale cement, which represents 29% of the model volume, possesses a permeability of 1.82μD. Illite accounts for the remaining 6% of the volume and exhibits a permeability of 5.64μD. Even though, illite makes-up for a tiny fraction of the model, a large volume of the gas flows through it. If illite's permeability was smaller

than that of the shale cement's permeability, it would have created bottlenecks and flowrate would have decreased precipitously.

To analyse the responsiveness of the gas flowrate to illite permeability, a range of different illite permeability values were investigated. Figure 47 displays the results of the simulations. Gas flow velocity findings were again normalised to the baseline case value. Interestingly, Figure 47 reveals that while the magnitude of illite's permeability is more or less comparable to the shale cement's permeability, variations in illite permeability do not induce significant changes in the gas flowrate. However, if illite's permeability is much smaller than that of the shale cement, the flowrate drops dramatically.
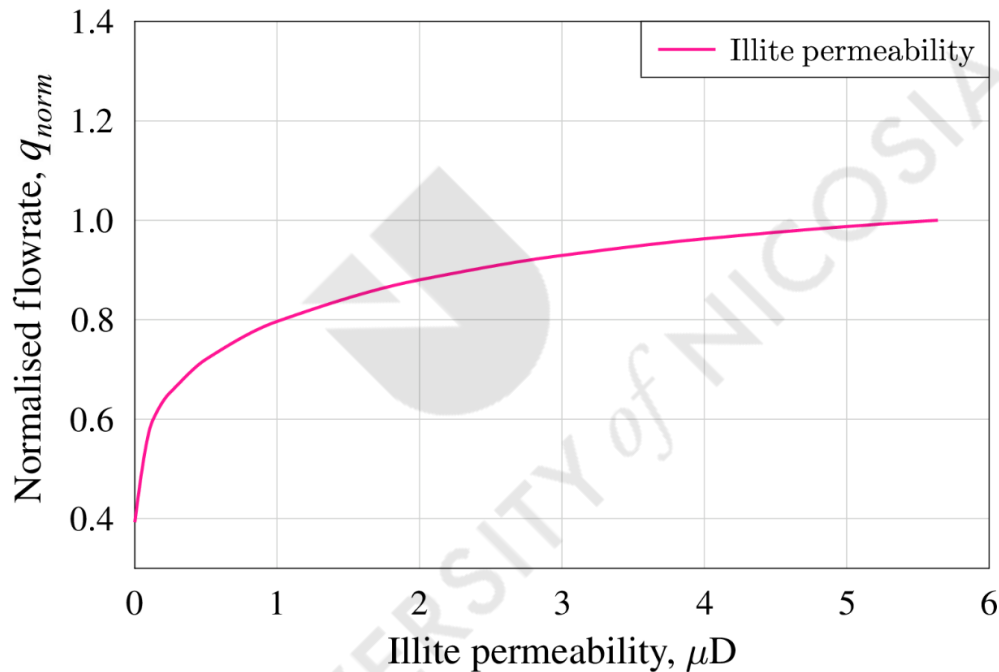
Figure 47. Sensitivity of the gas flowrate as dictated by variations in the illite permeability.

Again supported from Figure 47, if illite's permeability coincides with the shale cement's permeability, normalised flowrate is 87% of the base case permeability. In the event that illite is impermeable, normalised flowrate amounts to 39% of the baseline model value. Hence, formation areas which are characterised by higher permeability will command a smaller influence on flowrate in relation to the presence of any bottlenecks in the rock structure.

For better understanding of the pore-scale flow processes in the non-porous illite scenario we have recorded pressure and velocity variations inside the model in the same way it was done for the simulations related to the baseline model (see §4.1 "Micro-scale transient pressure and velocity results", page 49). Referring to Figure 48, four crosses are marked in blue colour. These comprise: Point 1 – just near the outlet; Point 2 – in the middle part of model; Point 3 – in the distant part from outlet side of the model; and Point 4 – in the pore throat. Points 1, 2 and 3 have been chosen to be the same as for the base case model, whereas Point 4 resides at the narrowest point in the pore channel which acts as a restriction to flow.
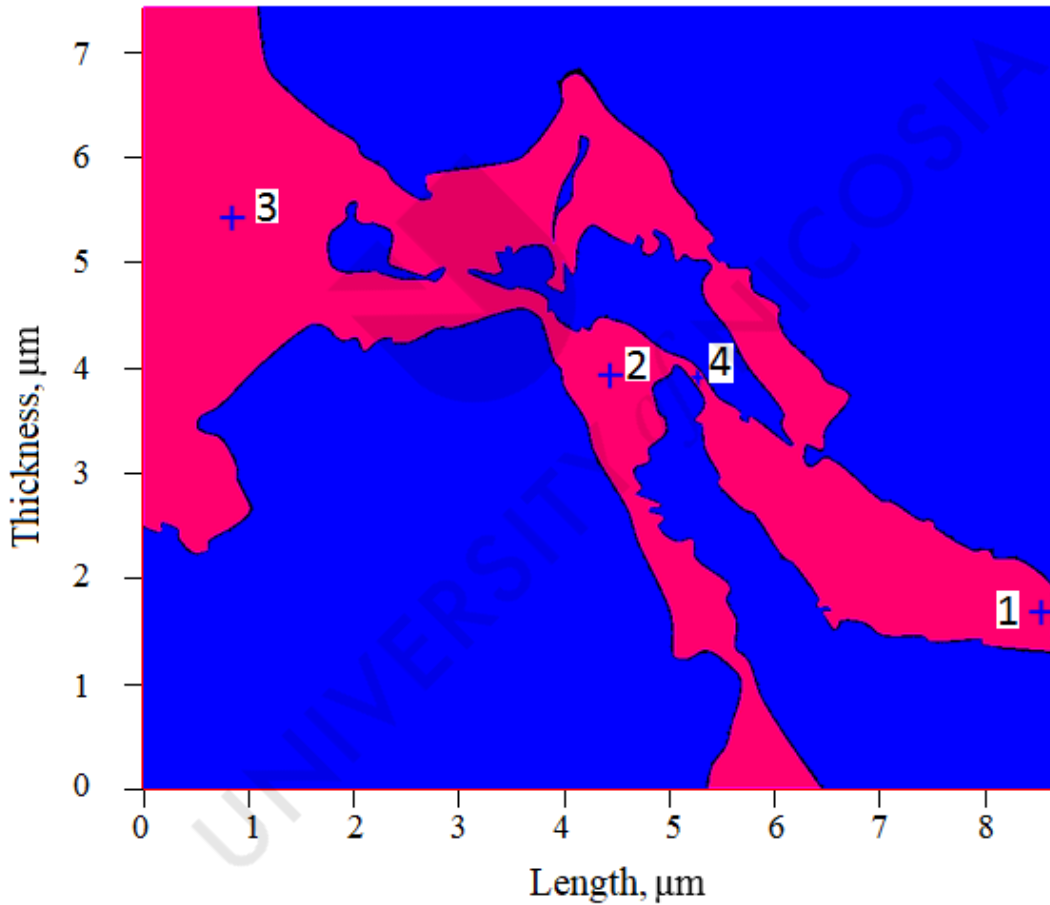
Figure 48. Point locations in the model with non-porous illite. Red colour indicates pore channel filled by shale cement where gas flow occurs. Blue colour is used for impermeable quartz and illite minerals.

Figure 49 to Figure *52* display the pressure profiles for the selected points. As it can be observed from these plots, the pressure and velocity profiles are similar to the corresponding values for the model with porous illite. However, observed features are more prominent for the non-porous illite model because of the presence of restrictions to flow. Readily discerned from the plots, the pressure profile in the near outlet point (Point1) is characterised by a steep decline. The pressure profile at the medium point (Point 2) undergoes a smoother pressure drop whereas the pressure at the far field (Point 3) exhibits a slow pressure reduction at the beginning. This behaviour can be explained in relation to the time it takes during the depletion situation for pressure decrease to propagate to the distant part of the rock sample at the micro-level or of the field at the macro-scale. Next, at Point 4, the slow pressure decrease is accompanied by a moderate pressure reduction with further slowdown in pressure decline. Variations in pressure at the pore throat are displayed in Figure 52. Initially, an abrupt pressure drop, comparable with the pressure reduction at the near outlet point (Point 1) manifests. Subsequently, a slow decline in pressure results in a drop of the pressure differential between Point 3 and the pore throat at Point 4.
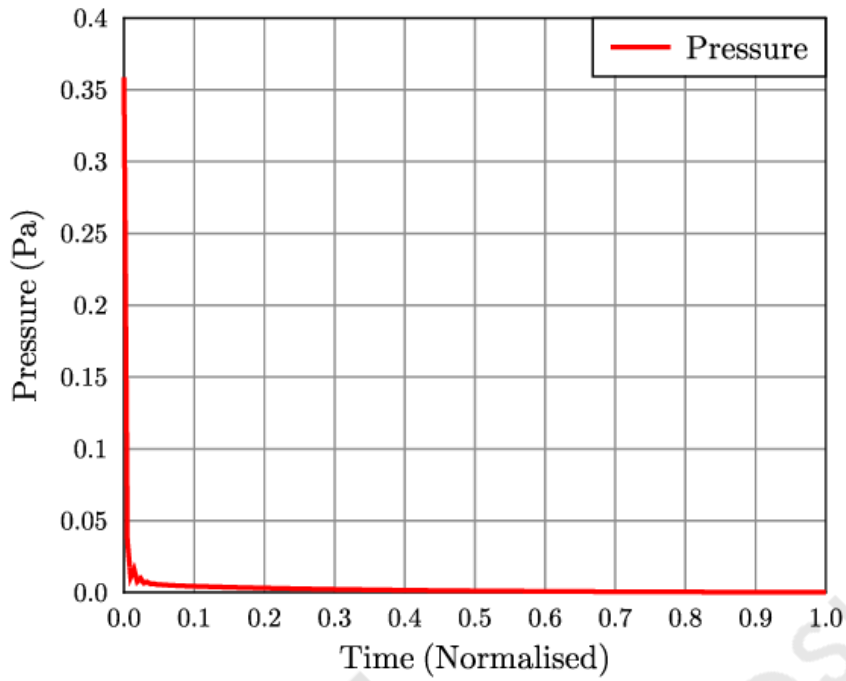
Figure 49. Pressure profile at the near outlet point (Point 1, Figure 48) of the model with non-porous illite.
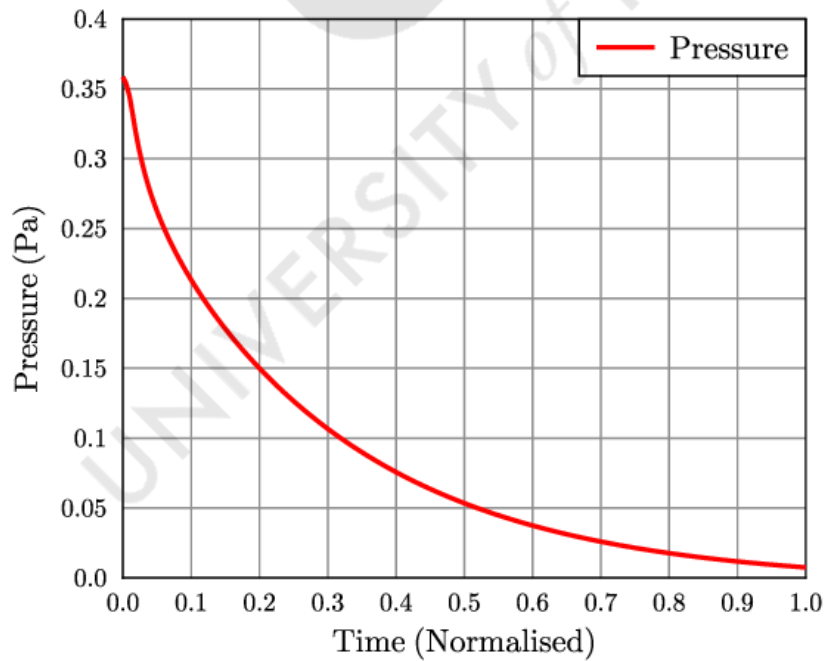
Figure 50. Pressure profile at the medium point (Point 2, Figure 48) of the model with non-porous illite.
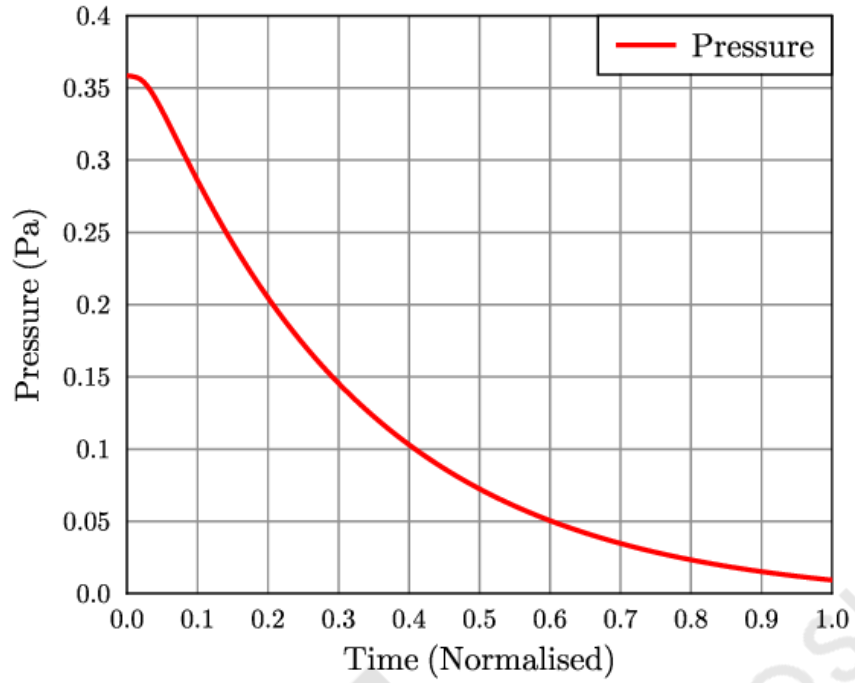
Figure 51. Pressure profile at the far point (Point 3, Figure 48) of the model with non-porous illite.
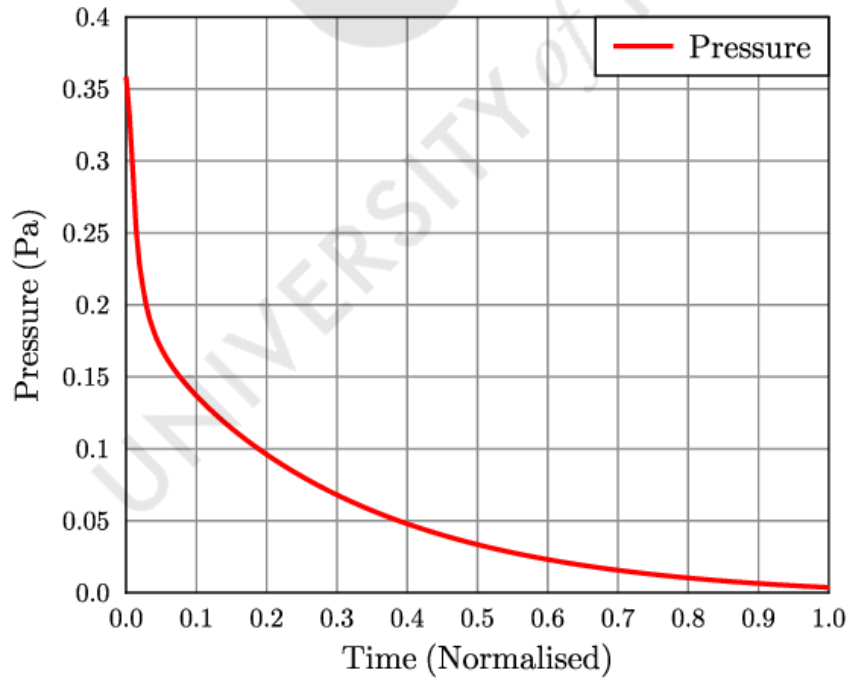
Figure 52. Pressure profile at the throat (Point 4, Figure 48) of the model with non-porous illite.

Figure 53 to Figure *56* display the captured velocity magnitude profiles for selected points. A sharp increase in velocity is shown on the profile tracing Point 1. Here, the maximum velocity magnitude is bigger than the peak velocity value at the pore throat. Followed then, a precipitous drop in velocity appears which becomes smoother at the end of the time interval. The velocity magnitude profiles at the medium (Point 2) and the far (Point 3) points are gentler. However, all features occur as in the velocity magnitude profile at the near point: fast growth up to the peak and gradual decline which becomes smoother while time is progressing. Moreover, as it can be observed from Figure 55, the wiggle can be easily discerned at the beginning of the velocity profile at the far point (Point 3) which was almost invisible at the velocity profile from the baseline model with porous illite (please refer to Figure 26). It occurs because in the middle part of the model, pressure changes faster than in the far part (see Figure 50 and Figure 51 for pressure profiles comparison) which leads to an increase in the pressure gradient at the pore throat. Impermeable illite acts as a flow restriction and results in a dramatic pore channel narrowing which, in turn, make all features of flowrate and pressure profiles more pronounced in comparison to the base case model (with porous illite). The velocity magnitude profile at the pore throat (Point 4) is similar to the velocity evolution at the medium point but differs in the absolute velocity values.
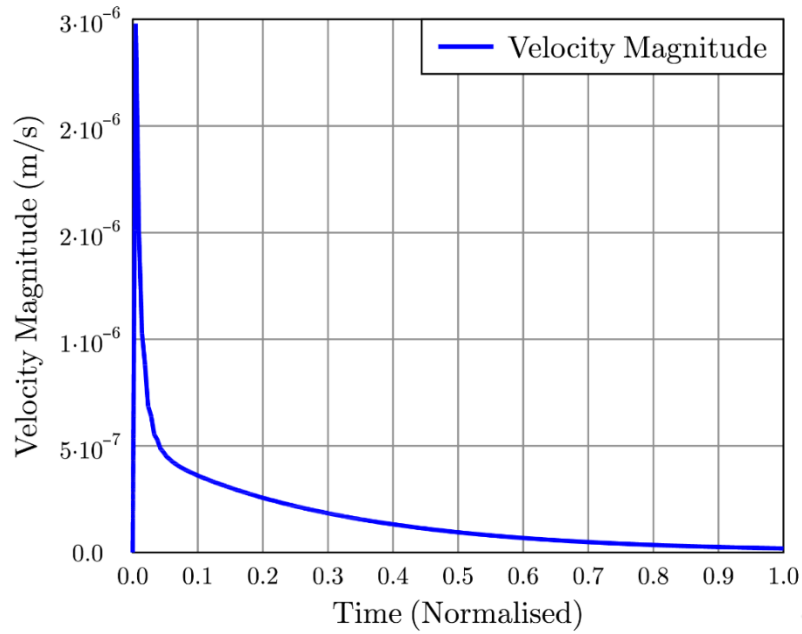
Figure 53. Velocity magnitude profile at the near outlet point (Point 1, Figure 48) of the model with non-porous illite. Velocity magnitude is a scalar velocity value, in simpler terms, the speed.
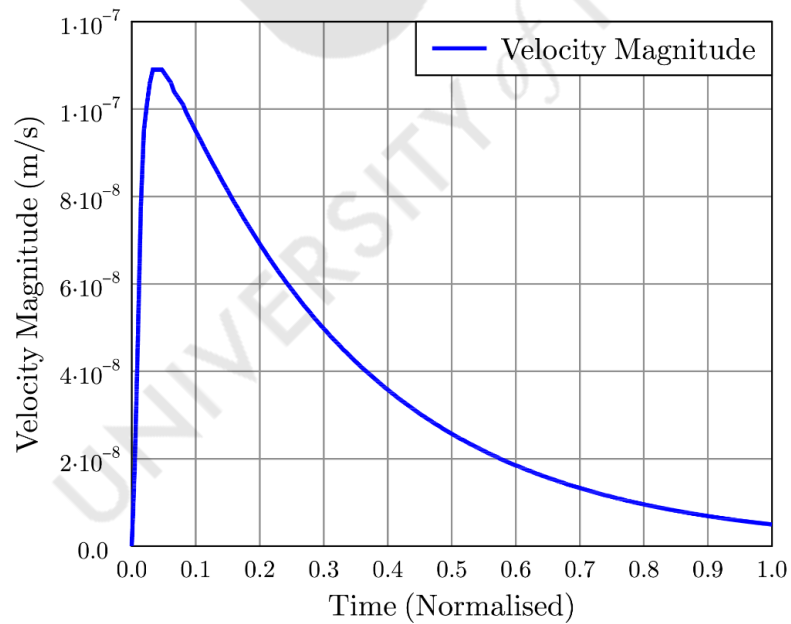
Figure 54. Velocity magnitude profile at the medium point (Point 2, Figure 48) of the model with non-porous illite. Velocity magnitude is a scalar velocity value, in simpler terms, the speed.
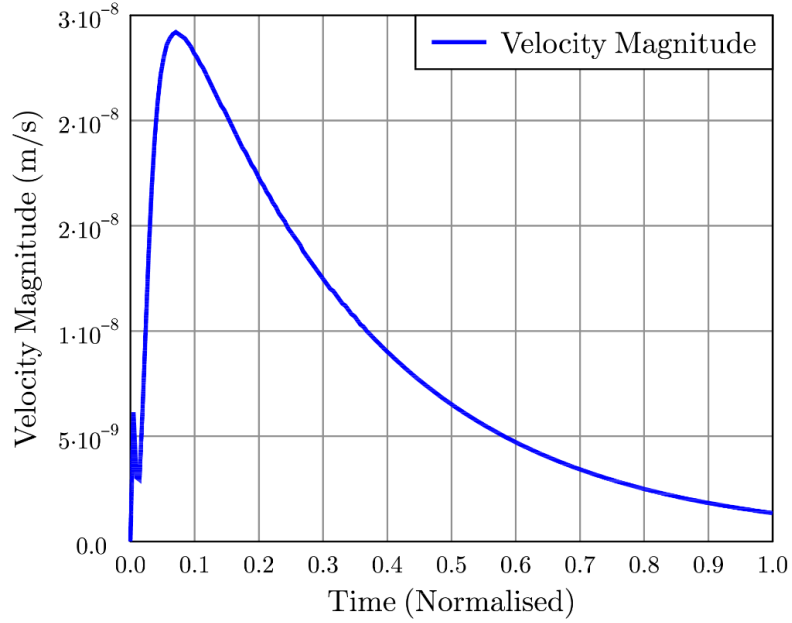
Figure 55. Velocity magnitude profile at the far point (Point 3, Figure 48) of the model with non-porous illite. Velocity magnitude is a scalar velocity value, in simpler terms, the speed.
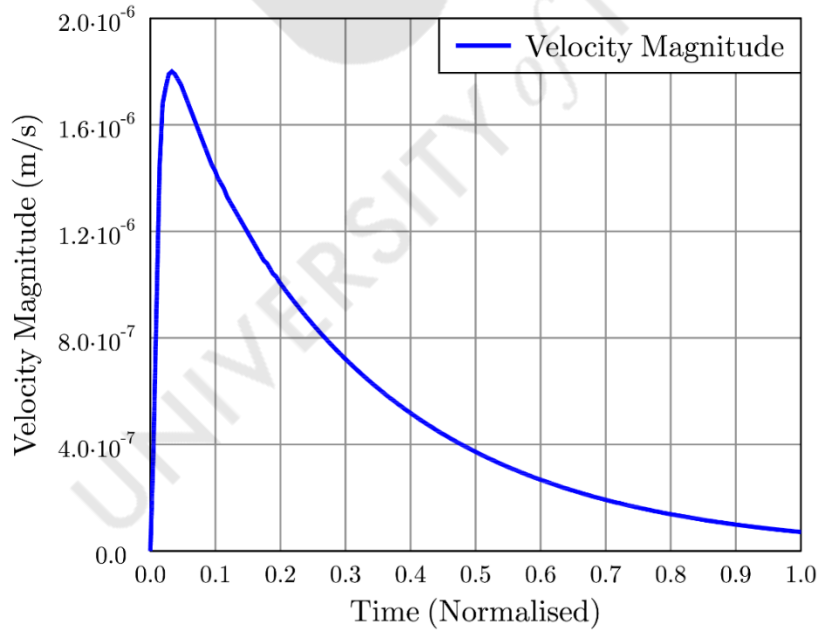
Figure 56. Velocity magnitude profile at the throat (Point 4, Figure 48) of the model with non-porous illite. Velocity magnitude is a scalar velocity value, in simpler terms, the speed.

Eventhough the shale matrix's permeability is the most important parameter with respect to gas flowrate, it is a formation property over which reservoir engineering has little control. The parameter which needs to be emphasised is reservoir pressure. Flowrate is less sensitive to formation pressure compared to permeability. However, reservoir pressure varies considerably during hydrocarbon production together with changes in fluid saturation. Whatsmore, pressure changes can be managed by an appropriate field production strategy. Thus, it is crucial to understand and monitor how pressure affects flowrate during the various stages of gas production. Likewise, gas composition exerts a considerable impact on the gas flowrate because gas density, viscosity and compressibility rest on it. Nevertheless, laboratory experiments and numerical simulations are performed mostly for pure methane, not for real reservoir fluids which influence the precision of the investigations. It is important to note that gas flowrate remains almost invariant with changes in temperature.

5. Concluding remarks

Flow in low-permeability unconventional reservoirs is an intricate process governed, to a large degree, by non-linear physical processes in contrast to conventional reservoirs. Flow characteristics in shale gas reservoirs are intimately connected with the micro- and the nano-scale pore sizes and structure. To capture the heterogeneity of shale porous media and the diversity of flow processes, we have constructed a geometrically accurate micro-scale model based on actual SEM imaging data. We have simulated the gas flow processes inside the shale matrix including viscous flow, slip flow, real gas compressibility, Knudsen diffusion, Klinkenberg permeability and adsorption and desorption at the microscopic level. In this work, we devised a non-dimensionalisation method applicable to gas shale reservoirs. This technique permits the comparison and integration of core measurements and computer simulation results transcending multiple temporal and spatial scales. The main contributions of this research are:

- We have developed a non-dimensionalisation approach considering Klinkenberg permeability and real gas behaviour which helps compare core measurements and simulation results for gas shale reservoirs.

- Our findings have demonstrated that gases with different chemical composition have a marked effect on the gas production rate and should be factored-in calculations appropriately.

- Adsorption modelling requires the accurate selection of an isotherm type and pertinent parameters. The gas production test measurements utilised to validate numerical results were shown to be the most consistent with the Klotz model.

- The performed sensitivity analysis revealed that the gas flowrate in shales is most sensitive to permeability, especially, its distribution and reservoir pressure. Highly permeable areas influence gas flowrate less than bottlenecks present in the pore network.

Non-dimensional simulation results and core findings for free and adsorbed gas display excellent agreement despite the spatial and temporal scales differing by several

orders of magnitude. Employing non-dimensionalisation can help perform more thorough characterisation of shale reservoirs and expedite laborious and time-demanding laboratory investigations by complementing and interchanging methods at different levels. With certain refinements, non-dimensionalising methodologies based on numerical simulations from the micro- to the macro-level can help bridge the gap between core or micro-CT flow results with well production data. Also, the approach proposed herein can be adapted and generalised in other cases involving complex formations, e.g., of carbonate origin.

The accurate modelling of adsorption and desorption processes is necessary to correctly estimate gas reserves. To ensure that the adsorption process is rigorously captured, the calculated isotherm profile should replicate experimental measurements within the whole pressure range. The Klotz isotherm model conforms with the isotherm profile from the core measurements illuminating the adsorption mechanism in the shale porous media. Non-dimensional cumulative gas production from the constructed model, with the incorporated Klotz isotherm, and rock findings show sound agreement.

Once the numerical model has been constructed, a sensitivity analysis has been performed to identify the parameters which influence flowrate the most and merit a more meticulous investigation. Our sensitivity study demonstrated that the main parameter governing flowrate is permeability and, particularly, permeability spatial distribution. Formation areas which are characterised by higher permeability will command a smaller influence on flowrate in relation to the presence of any bottlenecks in the rock structure. Although reservoir engineering has little control over the shale matrix permeability, the investigation of the pore network geometrical structure in shale formations permits the prediction of the future production more accurately and helps guide future decision-making. The other parameter which needs to be emphasised is reservoir pressure. Despite the fact that the flowrate is less sensitive to formation pressure compared to permeability, reservoir pressure varies considerably during different stages of hydrocarbon production. Moreover, pressure changes can be managed by an appropriate field production strategy. Eventually, our research advances the understanding pertaining to the physical processes in shale porous media and strengthens the capability to utilise shale resources more efficiently.

6. Future research directions

Although there are numerous directions to expand the research, two possible topics seem to be the most promising: 1) gas and water concurrent flow, and 2) multiscale modelling. Multiphase flow can result in more realistic production predictions since initial water or hydraulic fracture fluid always is present in gas shales. Multiscale modelling and upscaling methods could help fill this gap in knowledge and enhance macro-modelling methods what was one of the focal points of our research and also developed the non-dimensionalisation approach.

As in conventional reservoirs, the presence of water influences all of the flow mechanisms. Transport processes in water-wet shales are intrinsically complicated and multiphase flow investigations are incredibly challenging. Most investigations to-date have concentrated on single-phase flow, however, in shale gas reservoirs, a two-phase flow manifests because of the presence of innate water and fracturing fluid (Heller and Zoback 2014; Sui, Yao and Zhang 2015). Due to the fundamental differences between the flow patterns of single-phase and two-phase gas flow, the two-phase flow regime cannot be described by the Knudsen number alone. Few studies have focused on the relative permeability of the gas and the water phase in shale gas reservoirs with nanoscale pores (Jin and Firoozabadi 2014; Li, Song, *et al.* 2016; Sui, Yao and Zhang 2015).

The second future research line is related to multiscale modelling. Investigation of the physical processes manifesting in the shale matrix can be performed at multiple spatial and temporal scales. For instance, pore-level processes and mineral structure are investigated using diverse imaging techniques. Core experimental data enable investigations at the centimetre-scale and reservoir production data permit field scale analysis. It is vital to have the ability to compare and integrate all of these investigations' results transcending multiple temporal and spatial scales. Investigations of the upscaling methods of received results from the micro-level to macro-level can result in the possibility of constructing macro-models grounded in a sound understanding of the physical processes. These models can be useful not only for field production modelling and prediction, but also could a complement or even a substitute of core investigations.

References

Administration, US Energy Information. 2013. Technically Recoverable Shale Oil and Shale Gas Resources: An Assessment of 137 Shale Formations in 41 Countries Outside the United States, US Energy Information Administration - Independent Statistics and Analysis, Washington, DC (2013).

Al-Hussainy, Rafi, Ramey Jr, HJ, Crawford, PB. 1966. The flow of real gases through porous media. *journal of Petroleum Technology* **18** (05): 624-636. https://doi.org/10.2118/1243-A-PA.

Alfi, Masoud *et al.* 2015. Microscale porosity models as powerful tools to analyze hydrocarbon production mechanisms in liquid shale. *Journal of Natural Gas Science and Engineering* **26**: 1495-1505. https://doi.org/10.1016/j.jngse.2015.08.002.

Ali, Waqas. 2012. Modeling Gas Production from Shales and Coal-beds. Master of Science, Stanford University, Stanford (October 2012).

Amao, Abiodun Matthew. 2007. Mathematical model for Darcy Forchheimer flow with applications to well performance analysis. Master of Science, Texas Tech University (August, 2007).

Bahadori, Alireza. 2016. *Fluid Phase Behavior for Conventional and Unconventional Oil and Gas Reservoirs*, Gulf Professional Publishing. https://doi.org/10.1016/C2014-0-01653-X.

Bahoush, Kazerouni R, Kazemzadeh, Hanani S. 2009. Simulation of turbulent flow through porous media employing a v2f model. *Mechanical Engineering*: 159-167.

Bettotti, Paolo. 2017. *Submicron Porous Materials*, Springer. https://doi.org/10.1007/978-3-319-53035-2.

Bloshanskaya, Lidia *et al.* 2017. Productivity Index for Darcy and pre-/post-Darcy Flow (Analytical Approach). *Journal of Porous Media* **20** (9). https://doi.org/10.1615/JPorMedia.v20.i9.10.

Blunt, Martin J *et al.* 2013. Pore-scale imaging and modelling. *Advances in Water Resources* **51**: 197-216. https://doi.org/10.1016/j.advwatres.2012.03.003.

Bringedal, Carina. 2015. Modeling of heat transfer in porous media in the context of geothermal energy extraction. Doctor of Philosophy, University of Bergen, Bergen (02.10.2015).

Buttersack, Christoph. 2019. Modeling of type IV and V sigmoidal adsorption isotherms. *Physical Chemistry Chemical Physics* **21** (10): 5614-5626. https://doi.org/10.1039/C8CP07751G.

Chen, Lei *et al.* 2017. Application of Langmuir and Dubinin–Radushkevich models to estimate methane sorption capacity on two shale samples from the Upper Triassic Chang 7 Member in the southeastern Ordos Basin, China. *Energy Exploration & Exploitation* **35** (1): 122-144. https://doi.org/10.1177/0144598716684309.

Chen, Lei *et al.* 2019. Mechanisms of shale gas adsorption: Evidence from thermodynamics and kinetics study of methane adsorption on shale. *Chemical Engineering Journal* **361**: 559-570. https://doi.org/10.1016/j.cej.2018.11.185.

Chen, Li *et al.* 2015. Nanoscale simulation of shale transport properties using the lattice Boltzmann method: permeability and diffusivity. *Scientific Reports* **5**: 80-89. https://doi.org/10.1038/srep08089.

Chen, Zhangxin. 2000. Formulations and numerical methods of the black oil model in porous media. *SIAM Journal on Numerical Analysis* **38** (2): 489-514. https://doi.org/10.1137/S0036142999304263.

Clarkson, CR *et al.* 2016. Nanopores to megafractures: Current challenges and methods for shale gas reservoir and hydraulic fracture characterization. *Journal of Natural Gas Science and Engineering* **31**: 612-657. https://doi.org/10.1016/j.jngse.2016.01.041.

Coats, Keith H. 1980. An equation of state compositional model. *Society of Petroleum Engineers Journal* **20** (05): 363-376. https://doi.org/10.2118/8284-PA.

Coelho, Rodrigo CV, Neumann, Rodrigo F. 2016. Fluid dynamics in porous media with Sailfish. *European Journal of Physics* **37** (5): 055102. https://doi.org/10.1088/0143-0807/37/5/055102.

COMSOL, Multiphysics. 2017. *COMSOL Multiphysics User's Guide*, COMSOL AB Burlington, Mass.

Constant, Frank Woodbridge. 1963. *Fundamental Laws of Physics*, Addison-Wesley.

Curtis, Mark E *et al.* 2011. Investigating the microstructure of gas shales by FIB-SEM tomography & stem imaging. *Presentation given at the Oklahoma Geological Survey workshop, Norman, Oklahoma*, Vol. 21.

Darabi, Hamed *et al.* 2012. Gas flow in ultra-tight shale strata. *Journal of Fluid Mechanics* **710**: 641-658. https://doi.org/10.1017/jfm.2012.424.

Das, Malay K, Mukherjee, Partha P, Muralidhar, K. 2017. *Modeling Transport Phenomena in Porous Media with Applications*, Springer. https://doi.org/10.1007/978-3-319-69866-3.

Dejam, Morteza, Hassanzadeh, Hassan, Chen, Zhangxin. 2017. Pre-Darcy Flow in Porous Media. *Water Resources Research* **53** (10): 8187-8210. https://doi.org/10.1002/2017WR021257.

Duru, Obinna O, Horne, Roland N. 2010. Modeling reservoir temperature transients and reservoir-parameter estimation constrained to the model. *SPE Reservoir Evaluation & Engineering* **13** (06): 873-883. https://doi.org/10.2118/115791-PA.

Egbobawaye, Edwin Ikhuoria. 2013. Tight Gas Reservoir Characterization in Montney Formation, Northeastern British Columbia, Western Canada, University of Alberta (Canada).

Elsharkawy, Adel M. 2002. EOS's calculations of volumetric and transport properties of sour gases and gas condensates. *The 6th saudi engineering conference*: KFUPM Dhahran.

Elsharkawy, Adel M. 2004. Efficient methods for calculations of compressibility, density and viscosity of natural gases. *Fluid Phase Equilibria* **218** (1): 1-13. https://doi.org/10.1016/j.fluid.2003.02.003.

Erdogmus, M, Adewumi, Michael A, Ibraheem, SO. 1997. Viscosity prediction of natural gases. *SPE Eastern Regional Meeting*: Society of Petroleum Engineers. https://doi.org/10.2118/39219-MS.

ESI-CFD. 2014. CFD-ACE+ modules manual V2014.

Esteves, Isabel AAC *et al.* 2008. Adsorption of natural gas and biogas components on activated carbon. *Separation and Purification Technology* **62** (2): 281-296.

Etminan, S. Reza *et al.* 2014. Measurement of gas storage processes in shale and of the molecular diffusion coefficient in kerogen. *International Journal of Coal Geology* **123**: 10-19. http://dx.doi.org/10.1016/j.coal.2013.10.007.

Fan, Zhuoying *et al.* 2018. Investigating influential factors of the gas absorption capacity in shale reservoirs using integrated petrophysical, mineralogical and geochemical experiments: A case study. *Energies* **11** (11): 3078. https://doi.org/10.3390/en11113078.

Fathi, Ebrahim, Tinni, Ali, Akkutlu, I Yucel. 2012. Correction to Klinkenberg slip theory for gas flow in nano-capillaries. *International Journal of Coal Geology* **103**: 51-59. https://doi.org/10.1016/j.coal.2012.06.008.

Fianu, John Senam, Gholinezhad, Jebraeel, Sayed, Mohamed Hassan. 2019. Comparison of single, binary and temperature dependent adsorption models based on error function analysis. *Journal of Oil, Gas and Petrochemical Sciences* **2** (2): 77-91. https://doi.org/10.30881/jogps.00027.

Firouzi, Mahnaz *et al.* 2014. Klinkenberg effect on predicting and measuring helium permeability in gas shales. *International Journal of Coal Geology* **123**: 62-68. http://dx.doi.org/10.1016/j.coal.2013.09.006.

Firouzi, Mahnaz *et al.* 2014. Molecular simulation and experimental characterization of the nanoporous structures of coal and gas shale. *International Journal of Coal Geology* **121**: 123-128. http://dx.doi.org/10.1016/j.coal.2013.11.003.

Foo, K. Y., Hameed, B. H. 2010. Insights into the modeling of adsorption isotherm systems. *Chemical Engineering Journal* **156** (1): 2-10. http://dx.doi.org/10.1016/j.coal.2013.09.006.

Freeman, C. M., Moridis, G. J., Blasingame, T. A. 2011. A Numerical Study of Microscale Flow Behavior in Tight Gas and Shale Gas Reservoir Systems. *Transport in Porous Media* **90** (1): 253. 10.1007/s11242-011-9761-6.

Ghanizadeh, Amin *et al.* 2018. Laboratory-based characterization of pore network and matrix permeability in the Montney Formation: Insights from methodology comparisons. *Bulletin of Canadian Petroleum Geology* **66** (2): 472-498.

Gouth, Francois *et al.* 2013. Molecular simulation to determine key shale gas parameters, and their use in a commercial simulator for production forecasting. *EAGE annual conference & exhibition incorporating SPE Europec*: Society of Petroleum Engineers. https://doi.org/10.2118/164790-MS.

Guo, Chaohua, Wei, Mingzhen, Liu, Hong. 2015. Modeling of gas production from shale reservoirs considering multiple transport mechanisms. *PloS ONE* **10** (12): e0143649. https://doi.org/10.1371/journal.pone.0143649.

Guo, X. Q. *et al.* 2001. Equation of state analog correlations for the viscosity and thermal conductivity of hydrocarbons and reservoir fluids. *Journal of Petroleum Science and Engineering* **30** (1): 15-27. https://doi.org/10.1016/S0920-4105(01)00098-5.

Guo, X. Q. *et al.* 1997. Viscosity model based on equations of state for hydrocarbon liquids and gases. *Fluid Phase Equilibria* **139** (1-2): 405-421. https://doi.org/10.1016/S0378-3812(97)00156-8.

Haider, Batool Arhamna, Aziz, K. 2017. Impact of capillary pressure and critical property shift due to confinement on hydrocarbon production in shale reservoirs. *SPE Reservoir Simulation Conference*: Society of Petroleum Engineers. https://doi.org/10.2118/182603-MS.

Hall, Carl W. 1999. *Laws and models: science, engineering, and technology*. Boca Raton, CRC Press. https://doi.org/10.1201/9781315219585

Hattori, Gabriel *et al.* 2017. Numerical simulation of fracking in shale rocks: current state and future approaches. *Archives of Computational Methods in Engineering* **24** (2): 281-317.

He, Zhong. 2011. Flow of Gas and Water in Hydraulically Fractured Shale Gas Reservoirs. *for the Hydraulic Fracturing Study: Fate and Transport*: 67.

Heller, Robert, Zoback, Mark. 2014. Adsorption of methane and carbon dioxide on gas shale and pure mineral samples. *Journal of Unconventional Oil and Gas Resources* **8**: 14-24. https://doi.org/10.1016/j.juogr.2014.06.001.

Huang, Ting *et al.* 2019. A novel numerical model of gas transport in multiscale shale gas reservoirs with considering surface diffusion and Langmuir slip conditions. *Energy Science & Engineering* **7** (4): 1315-1332. https://doi.org/10.1002/ese3.351.

Inglezakis, Vassilis J, Poulopoulos, Stavros G, Kazemian, Hossein. 2018. Insights into the S-shaped sorption isotherms and their dimensionless forms. *Microporous and Mesoporous Materials* **272**: 166-176. https://doi.org/10.1016/j.micromeso.2018.06.026.

Islam, Mir Raisul *et al.* 2017. Rate transient analysis of Well-07 and Well-10 of Habiganj gas field, Bangladesh. *Journal of Petroleum Exploration and Production Technology* **7** (2): 569-588. http://dx.doi.org/10.1007/s13202-016-0278-y.

Javadpour, Farzam, Fisher, D, Unsworth, M. 2007. Nanoscale gas flow in shale gas sediments. *Journal of Canadian Petroleum Technology* **46** (10). https://doi.org/10.2118/07-10-06.

Jenkins, CD *et al.* 2010. Innovative Modeling Techniques to Quantify Fracture Characteristics, Reservoir Properties, & Well Performance in Shales. *Second EAGE Workshop on Shales*. https://doi.org/10.3997/2214-4609.20145390.

Jin, Zhehui, Firoozabadi, Abbas. 2014. Effect of water on methane and carbon dioxide sorption in clay minerals by Monte Carlo simulations. *Fluid Phase Equilibria* **382**: 10-20. https://doi.org/10.1016/j.fluid.2014.07.035.

Kalantari-Dahaghi, Mirmasoud, Mohaghegh, Shahab D. 2011. A new practical approach in modelling and simulation of shale gas reservoirs: application to New Albany Shale. *Oil, Gas and Coal Technology* **4** (2): 104–133. https://dx.doi.org/10.1504/IJOGCT.2011.038925.

Karniadakis, George, Beskok, Ali, Aluru, Narayan. 2005. Governing equations and slip models. *Microflows and Nanoflows: Fundamentals and Simulation*: 51-77. https://doi.org/10.1007/0-387-28676-4.

Kazmouz, Samuel J, Giusti, Andrea, Mastorakos, Epaminondas. 2016. Numerical simulation of shale gas flow in three-dimensional fractured porous media. *Journal of Unconventional Oil and Gas Resources* **16**: 90-112. https://doi.org/10.1016/j.juogr.2016.10.002.

107

Ketter, Aaron A *et al.* 2008. A field study in optimizing completion strategies for fracture initiation in Barnett Shale horizontal wells. *SPE Production & Operations* **23** (03): 373-378.

King, M. R. 2007. Oscillatory gas flow in a circular nanotube. *Open Nanoscience Journal* **1**: 1-4. https://doi.org/10.2174/1874140100701010001.

Klinkenberg, L. J. 1941. The permeability of porous media to liquids and gases. *Drilling and production practice*: American Petroleum Institute. https://doi.org/10.5510/OGP20120200114.

Kovalchuk, Natalia, Hadjistassou, Constantinos. 2018. New insights from shale gas production at the microscopic scale. *The European Physical Journal E* **41** (11). 134. https://doi.org/10.1140/epje/i2018-11741-5.

Kovalchuk, Natalia, Hadjistassou, Constantinos. 2019. Laws and principles governing fluid flow in porous media. *The European Physical Journal E* **42** (5). 56. https://doi.org/10.1140/epje/i2019-11819-6.

Kovalchuk, Natalia, Hadjistassou, Constantinos. 2020. Fathoming the Mechanics of Shale Gas Production at the Microscale. *Journal of Natural Gas Science and Engineering* **78**: 103283. https://doi.org/10.1016/j.jngse.2020.103283.

Lan, Yuzheng, Moghanloo, Rouzbeh Ghanbarnezhad, Davudov, Davud. 2017. Pore compressibility of shale formations. *SPE Journal* **22** (06): 1,778-1,789. https://doi.org/10.2118/185059-PA.

Lawal, A. S. 1986. Prediction of vapor and liquid viscosities from the Lawal-Lake-Silberberg equation of state. *SPE enhanced oil recovery symposium*: Society of Petroleum Engineers. https://doi.org/10.2118/14926-MS.

Lee, Dae Sung *et al.* 2011. A critical evaluation of unconventional gas recovery from the marcellus shale, northeastern United States. *KSCE Journal of Civil Engineering* **15** (4): 679. 10.1007/s12205-011-0008-4.

Lee, Kun Sang, Kim, Tae Hong. 2016. *Integrative Understanding of Shale Gas Reservoirs*, Springer International Publishing. https://doi.org/10.1007/978-3-319-29296-0.

Li, Qingyu *et al.* 2018. A Novel Analytical Method to Calculate the Amounts of Free and Adsorbed Gas in Shale Gas Production. *Mathematical Problems in Engineering* **2018**. https://doi.org/10.1155/2018/2091695.

Li, Tianxin *et al.* 2016. An analytical method for modeling and analysis gas-water relative permeability in nanoscale pores with interfacial effects. *International Journal of Coal Geology* **159**: 71-81. https://doi.org/10.1016/j.coal.2016.03.018.

Li, Zhong-Zhen *et al.* 2016. Investigation of methane adsorption and its effect on gas transport in shale matrix through microscale and mesoscale simulations. *International Journal of Heat and Mass Transfer* **98**: 675-686. https://doi.org/10.1016/j.ijheatmasstransfer.2016.03.039.

Limousin, G *et al.* 2007. Sorption isotherms: a review on physical bases, modeling and measurement. *Applied geochemistry* **22** (2): 249-275. https://doi.org/10.1016/j.apgeochem.2006.09.010.

Liu, Lingling *et al.* 2019. Application of Nanotechnology in the Removal of Heavy Metal From Water. In *Nanomaterials for the Removal of Pollutants and Resource Reutilization*, 83-147. Elsevier. https://doi.org/10.1016/B978-0-12-814837-2.00004-4.

Lockerby, Duncan A, Reese, JM, Gallis, Michael A. 2005. A wall-function approach to incorporating Knudsen-layer effects in gas micro flow simulations. *AIP Conference Proceedings*, Vol. 762, 731-736: AIP. https://doi.org/10.1063/1.1941622.

McNenly, Matthew J, Gallis, Michael A, Boyd, Iain D. 2005. Empirical slip and viscosity model performance for microscale gas flow. *International journal for numerical methods in fluids* **49** (11): 1169-1191. https://doi.org/10.1002/fld.1012.

Mehmani, Ayaz, Prodanović, Maša, Javadpour, Farzam. 2013. Multiscale, Multiphysics Network Modeling of Shale Matrix Gas Flows. *Transport in Porous Media* **99** (2): 377-390. https://doi.org/10.1007/s11242-013-0191-5.

Michalis, Vasilis K *et al.* 2010. Rarefaction effects on gas viscosity in the Knudsen transition regime. *Microfluidics and nanofluidics* **9** (4-5): 847-853. https://doi.org/10.1007/s10404-010-0606-3.

Morales-German, Gabriela, Navarro, Rafael, Dubost, Francois Xavier. 2012. Approach Models Shale Gas Production. *The American Oil & Gas Reporter*.

Morales-German, Gabriela *et al.* 2012. Approach models shale gas production. *American Oil and Gas Reporter*.

Nakagaki, Masayuki, Handa, Tetsurou, Shimabayashi, Saburo. 1973. S—shaped adsorption isotherms of surface active electrolytes from aqueous solutions. *Journal of Colloid and Interface Science* **43** (2): 521-529. https://doi.org/10.1016/0021-9797(73)90398-6.

Nezhad, Mohaddeseh Mousavi *et al.* 2018. Experimental study and numerical modeling of fracture propagation in shale rocks during Brazilian disk test. *Rock Mechanics and Rock Engineering* **51** (6): 1755-1775.

Ning, Yang *et al.* 2019. Numerical modeling of gas transport in shales to estimate rock and fluid properties based on multiscale digital rocks. *Energy Procedia* **158**: 6093-6098. https://doi.org/10.1016/j.egypro.2019.01.505.

Okoro, Emeka Emmanuel *et al.* 2017. Measurement of the Best Z-Factor Correlation Using Gas Well Inflow Performance Data in Niger-Delta. *International Journal of Applied Engineering Research* **12** (12): 3507-3522.

Pepper, Darrell W, Heinrich, Juan C. 2017. *The finite element method: basic concepts and applications with MATLAB, MAPLE, and COMSOL*, CRC press. https://doi.org/10.1201/9781315395104

Rao, Vikram, Knight, Rob. 2016. *Sustainable Shale Oil and Gas: Analytical Chemistry, Geochemistry, and Biochemistry Methods*. United States, Elsevier. https://doi.org/10.1016/C2015-0-06384-5.

Raoof, Amir, Hassanizadeh, S. Majid. 2010. A New Method for Generating Pore-Network Models of Porous Media. *Transport in Porous Media* **81** (3): 391-407. https://doi.org/10.1007/s11242-009-9412-3.

Ren, Junjie *et al.* 2015. A lattice Boltzmann model for simulating gas flow in kerogen pores. *Transport in Porous Media* **106** (2): 285-301. https://doi.org/10.1007/s11242-014-0401-9.

Rezaee, Reza. 2015. *Fundamentals of Gas Shale Reservoirs*. Hoboken, New Jersey, John Wiley & Sons. http://dx.doi.org/10.1002/9781119039228.

Ross, Daniel J. K., Bustin, R. Marc. 2007. Shale gas potential of the lower Jurassic Gordondale member, northeastern British Columbia, Canada. *Bulletin of Canadian Petroleum Geology* **55** (1): 51-75. https://doi.org/10.2113/gscpgbull.55.1.51.

Roy, Subrata *et al.* 2003. Modeling gas flow through microchannels and nanopores. *Journal of Applied Physics* **93** (8): 4870-4879. http://dx.doi.org/10.1063/1.1559936.

Sang, Qian *et al.* 2016. Experimental investigation of gas production processes in shale. *International Journal of Coal Geology* **159**: 30-47. https://doi.org/10.1016/j.coal.2016.03.017.

Sheng, Guanglong, Javadpour, Farzam, Su, Yuliang. 2018. Effect of microscale compressibility on apparent porosity and permeability in shale gas reservoirs. *International Journal of Heat and Mass Transfer* **120**: 56-65. https://doi.org/10.1016/j.ijheatmasstransfer.2017.12.014.

Sheng, Qiang, Thompson, Karsten. 2013. Dynamic coupling of pore-scale and reservoir-scale models for multiphase flow. *Water Resources Research* **49** (9): 5973-5988. https://doi.org/10.1002/wrcr.20430.

Solar, Cecilia *et al.* 2010. Adsorption of methane in porous materials as the basis for the storage of natural gas. In *Natural Gas*, 205-244. https://www.doi.org/10.5772/9846.

Song, Hongqing *et al.* 2015. Numerical investigation of gas flow rate in shale gas reservoirs with nanoporous media. *International Journal of Heat and Mass Transfer* **80**: 626-635. https://doi.org/10.1016/j.ijheatmasstransfer.2014.09.039.

Sui, Hongguang, Yao, Jun, Zhang, Lei. 2015. Molecular simulation of shale gas adsorption and diffusion in clay nanopores. *Computation* **3** (4): 687-700. https://doi.org/10.3390/computation3040687.

Tahmasebi, Pejman, Javadpour, Farzam, Sahimi, Muhammad. 2015. Multiscale and multiresolution modeling of shales and their flow and morphological properties. *Scientific Reports* **5**: 16373. https://doi.org/10.1038/srep16373.

Tiab, Djebbar, Donaldson, Erle C. 2016. *Petrophysics: Theory and Practice of Measuring Reservoir Rock and Fluid Transport Properties*, 4th edition, Gulf Professional Publishing. https://doi.org/10.1016/C2014-0-03707-0.

Voigt, Eva Maria, Tomlinson, RH. 1955. The determination of pore size distribution and surface area from adsorption isotherms. *Canadian Journal of Chemistry* **33** (2): 215-231. https://doi.org/10.1139/v55-025.

Yamaguchi, H, Matsuda, Y, Niimi, T. 2012. Tangential momentum accommodation coefficient measurements for various materials and gas species. *Journal of Physics: Conference Series*, Vol. 362, 012035: IOP Publishing. https://doi.org/10.1088/1742-6596/362/1/012035.

Yang, Shenglai, Wei, JZ. 2017. *Fundamentals of Petrophysics*. Berlin, Springer. https://doi.org/10.1007/978-3-662-55029-8.

Yang, Zehao *et al.* 2016. A model of dynamic adsorption–diffusion for modeling gas transport and storage in shale. *Fuel* **173**: 115-128. https://doi.org/10.1016/j.fuel.2016.01.037.

Yu, Hao *et al.* 2017. Multiscale transport mechanism of shale gas in micro/nano-pores. *International Journal of Heat and Mass Transfer* **111**: 1172-1180. https://doi.org/10.1016/j.ijheatmasstransfer.2017.04.050.

Yu, Wei, Sepehrnoori, Kamy, Patzek, Tadeusz Wiktor. 2014. Evaluation of gas adsorption in Marcellus Shale. *SPE Annual Technical Conference and Exhibition*: Society of Petroleum Engineers. https://doi.org/10.2118/170801-MS.

Yuan, Weina *et al.* 2014. Experimental study and modelling of methane adsorption and diffusion in shale. *Fuel* **117**: 509-519. https://doi.org/10.1016/j.fuel.2013.09.046.

Zhang, Pengwei *et al.* 2015. Micro/Nano-pore Network Analysis of Gas Flow in Shale Matrix. *Scientific Reports* **5**: 13501. 10.1038/srep13501.

Zhang, Xiaoling *et al.* 2014. Lattice Boltzmann Simulation of Shale Gas Transport in Organic Nano-Pores. *Scientific Reports* **4**: 4843. 10.1038/srep04843.

Zhang, Xiaoyang *et al.* 2017. Rate decline analysis of vertically fractured wells in shale gas reservoirs. *Energies* **10** (10): 1602. https://dx.doi.org/10.3390/en10101602.

Zou, Jie, Rezaee, Reza. 2019. A Prediction Model for Methane Adsorption Capacity in Shale Gas Reservoirs. *Energies* **12** (2): 280. https://doi.org/10.3390/en12020280.